

Temperature quenching in
LAB based liquid scintillator and
muon-induced backgrounds
in the SNO+ experiment

Dissertation

zur Erlangung des akademischen Grades

Doctor rerum naturalium

(Dr. rer. nat.)

vorgelegt von

Arnd Sörensen

geboren am 07.11.1986 in Arnstadt

Fakultät Mathematik und Naturwissenschaften
der Technischen Universität Dresden
2016

To my parents, for giving me life, the greatest gift of all.

Eingereicht am 21.03.2016
Verteidigt am 14.10.2016

1. Gutachter: Prof. Dr. Kai Zuber (TU Dresden)
2. Gutachter: Prof. Dr. Soo-Bong Kim (Seoul National University)

Abstract

The starting SNO+ experiment, successor to the Sudbury Neutrino Observatory, is a neutrino detector using LAB based liquid scintillator as active medium. Situated in the SNOLab deep underground laboratory in Sudbury, Canada, the rock overburden amounts to about 6 km.w.e., providing an effective shielding against cosmic rays. The residual muon rate is $63 \mu/\text{day}$ going through the detector volume. About 780 t of an LAB mixture inside an acrylic sphere with a 6 m radius will be observed by ≈ 9300 photomultipliers, surrounded by a ≈ 7000 t water shielding. SNO+ will be searching for low energy solar-, geo-, reactor- and supernova neutrinos, but the main goal is the observation of the neutrinoless double beta decay in ^{130}Te . Under operating conditions, the scintillator will be cooled to about 12°C . This work investigated the effect of temperature changes on the light output of LAB based liquid scintillator in a range from -5°C to 30°C with α -particles and electrons in a small scale setup. Assuming a linear behaviour, a combined negative temperature coefficient of $(-0.29 \pm 0.01) \%/^\circ\text{C}$ is found. Considering hints for a particle type dependency, electrons show $(-0.17 \pm 0.02) \%/^\circ\text{C}$ whereas the temperature dependency seems stronger for α -particles $(-0.35 \pm 0.03) \%/^\circ\text{C}$. A pulse shape analysis shows increased strength of a slow decay component at lower temperatures, pointing to reduced non-radiative triplet state de-excitations at lower temperatures. Furthermore, this work found upper bounds for the in-situ muon-induced isotope production via scaling calculations and simulations with Geant4 based software. For the most concerning isotope ^{11}C , an upper limit of about 1.3×10^3 decays/kt/yr is found and a reduction technique, developed by the Borexino collaboration, can be effectively applied for SNO+. Also a muon reconstruction algorithm is implemented, performing reasonably well, but not good enough to improve the background reduction scheme.

Kurzfassung

Das zukünftige SNO+ experiment, Nachfolger des Sudbury Neutrino Observatory, ist ein Neutrino-Detektor mit LAB basierten Flüssigszintillator als aktivem Medium. Im SNOLab Untertagelabor (Sudbury, Kanada) gelegen, ist es durch die Felsüberdeckung von 6 km.w.e. hervorragend gegen kosmische Strahlung abgeschirmt. Die Rate der übrigen Myonen die das Detektorvolumen durchdringen beträgt ca. $63 \mu/\text{Tag}$. In einer Acrylkugel, mit einem Radius von 6 m, wird eine LAB Mischung von ≈ 9300 Photomultipliern beobachtet und von einer Wasserabschirmung von ≈ 7 kt umgeben. SNO+ wird nach niederenergetischen solaren-, Geo-, Reaktor- und Supernova Neutrinos suchen, aber das Hauptziel ist die Beobachtung von neutrinolosen doppelten Betazerfällen in ^{130}Te . Unter den Betriebsbedingungen wird er Flüssigszintillator eine Temperatur von ca. 12°C annehmen. Diese Arbeit hat den Einfluss von Temperaturveränderungen in einem Bereich von -5°C to 30°C auf die erzeugte Lichtmenge untersucht. Dazu wurden α -Teilchen und Elektronen in einem kleineren Versuchsaufbau beobachtet. Unter der Annahme eines linearen Verhaltens, wurde ein globaler negativer Temperaturkoeffizient von $(-0.29 \pm 0.01) \%/^\circ\text{C}$ gefunden. Unter Berücksichtigung von Hinweisen auf eine Teilchenartabhängigkeit, findet sich für Elektronen ein Koeffizient von $(-0.17 \pm 0.02) \%/^\circ\text{C}$, wohingegen α -Teilchen eine stärkere Abhängigkeit von $(-0.35 \pm 0.03) \%/^\circ\text{C}$ aufweisen. Eine Pulsform-Analyse zeigt eine bei tieferen Temperaturen stärker ausgeprägte langsame Zerfallskomponente, was darauf hinweist dass die nicht-radiativen Abregungen der Triplet-Zustände bei niedrigeren Temperaturen reduziert sind. Weiterhin wurden in dieser Arbeit obere Ausschlußgrenzen für in-situ Myon-induzierte Isotopenproduktion gefunden, wozu Skalierungsrechnungen und Simulation mit auf Geant4 basierender Software benutzt wurden. Für das wichtigste Isotop ^{11}C wurde eine obere Grenze von 1.3×10^3 Ereignisse/kt/Jahr gefunden und eine Technik zur Reduzierung des Untergrundes, entwickelt von der Borexino Kollaboration, kann effektiv für SNO+ angewendet werden. Darüber hinaus wurde eine Myon Spurrekonstruktion implementiert, die sinnvolle Ergebnisse liefert, aber nicht gut genug ist um die Untergrund Reduzierung zu unterstützen.

Contents

1	Introduction	1
2	Neutrino physics	5
2.1	Neutrinoless double beta decay	7
2.2	Solar neutrinos	15
2.3	Geo- and reactor neutrinos	18
2.4	Supernova neutrinos	19
3	The SNO+ experiment	21
3.1	Detector setup	22
3.2	Search for $0\nu\beta\beta$ -decay in ^{130}Te	25
3.3	CNO, pep and pp solar neutrinos	26
3.4	Reactor-, geo- and supernova neutrinos	28
4	Organic liquid scintillator	31
4.1	Physics of scintillation in organic liquids	32
4.2	Quenching	38
4.3	Linear alkyl benzene and SNO+	42
4.4	Temperature effects	45
5	Temperature quenching measurements	49
5.1	Experimental setup	50
5.1.1	The detector	50
5.1.2	Commissioning and data acquisition	53
5.1.3	Detector developments	55
5.2	PMT sensitivity control	57
5.2.1	Hardware	58
5.2.2	Proof of concept	59
5.3	LAB absorption and emission spectroscopy	62
5.4	Energy calibration	65
5.5	Energy calibration at different temperatures	72
5.6	Pure LAB background spectrum	73
5.7	Samarium loaded LAB measurements	75
5.7.1	Spectral analysis	75
5.7.2	Pulse shape analysis	78

5.8	Radon loaded LAB measurements	79
5.8.1	Spectral analysis I - no energy or time cuts	82
5.8.2	Spectral analysis II - application of energy and time cuts	84
5.8.3	Pulse shape analysis	88
5.9	Discussion and Conclusions	90
6	Muons in SNO+	95
6.1	Cosmic ray muons underground	97
6.2	Muon-induced backgrounds	98
6.2.1	Scaling calculations	102
6.2.2	Simulations with RAT	104
6.2.3	¹¹ C background reduction technique	108
6.3	Track reconstruction	110
6.3.1	Track reconstruction for muons only in water	113
6.3.2	Track reconstruction for muons in liquid scintillator	114
6.3.3	Results	117
7	Conclusions	121
A	List of power law exponents α	125
	Acronyms	127
	Bibliography	129
	Acknowledgement	139

CHAPTER **1**

Introduction

FUNDAMENTAL research is the basis for progress, innovations and in general the improvement of the conditions of human life. Although it is so strictly logical, it is not at all obvious in every day life. Nevertheless has new knowledge about the elements of our world and their interaction almost always led to great inventions. Instructive examples are modern day medical imaging and radiation based cancer treatment which are widely based on our knowledge of elementary particle- and nuclear physics. Hardly could have had C. D. Anderson imagined that his discovery of the positron would one day lead to positron emission tomography (PET), which is now a standard instrument to find cancer cells in the human body. The positron also nicely illustrates the other, most often underestimated, aspect of basic research, an ever-changing view of the world we are living in. This discovery of the anti-particle to the electron also marks the discovery of anti-matter in general, and its pure existence changed the view of our universe forever. Not long before the experimental evidence, W. Pauli postulated that there must exist another, much more elusive particle, which was later named neutrino.

Already from the beginning of neutrino physics, the nature of the weak interaction made it necessary to build large experiments, with only few exceptions, in order to gain insight into neutrino properties. A long list of experiments can be called to account for the progress in this field of elementary particle physics, like the Wu-, Goldhaber-, Homestake- and Heidelberg-Moscow-Experiment as well as Kamiokande, Super-Kamiokande, KamLAND, Borexino and many more.

One of the most important ones was the Sudbury Neutrino Observatory (SNO), which was situated in an active nickel mine near the city of Sudbury, Canada. SNO solved the so-called *solar neutrino problem*: the fact that the predictions for the solar neutrino fluxes were two to three times higher than all measurements showed until then. Initially established by H. Chen and G. Ewan, the international collaboration built a larger water Cherenkov detector underground, which was operated in three different phases, in order to measure the electron- and flavour-independent neutrino flux from the sun. This very successful approach could resolve the discrepancy and in connection with the results from another large scale experiment, Super-Kamiokande, neutrino oscillations were finally found as the solution. Moreover, this result has also proven that neutrinos must have a mass, which was before assumed to be vanishing, changing the fundamentals of our understanding of the particle world. This great success was in 2015 rewarded with the Nobel Prize in physics to the spokespersons of the experiments, A. B. McDonald and T. Kajita, representing their collaborations.

After the end of SNO in 2006, the whole infrastructure of the experiment was still available in its place and was calling for another use. Parts of the initial SNO collaboration proposed to change the detector setup towards a use with liquid scintillator. A new collaboration, building the so-called SNO + liquid scintillator (SNO+) experiment, was formed. Instead of heavy water, SNO+ will be filled with an organic liquid scintillator based on linear alkyl benzene (LAB). This allows to detect neutrinos with lower energies and therefore from a broader variety of sources, such as low energy solar neutrinos, those from the radioactivity in the earths crust and mantle, as well as neutrinos from nuclear power plants or supernovae. However the main goal of the experiment is to dissolve large amounts of tellurium into the liquid scintillator

and thus to search for the so-called neutrinoless double β -decay. Currently SNO+ is being started with the filling of light water into the detector, and is expected to take the first data by the end of 2016.

The active medium of SNO+ will be immersed in a water shielding that mainly serves as a protection against natural radioactivity but also cools the photomultipliers that are used to detect the scintillation light. This water will have a temperature of about 12° C and thus significantly cools down also the LAB mixture inside the detector. So far, very few work has been done on the influence of temperature on the light yield of liquid scintillator, and available studies are mostly qualitatively and show very few reliable data. Especially the light yield is an extremely important ingredient for the success of these kinds of experiments, as it is directly linked to the energy reconstruction. Therefore this work investigates the effects of cooling on to the light generation in LAB based liquid scintillator mixtures. Beside the immediate benefit for SNO+, this helps to find general insights into the properties of this material and might help also other large scale experiments like e.g. JUNO.

The other topic of this thesis is linked to the fact that SNO+ is situated in a very deep underground laboratory to escape cosmic radiation as good as possible, but still has to deal with some residual cosmic ray muons. Even though the flux is much lower than for comparable experiments, these highly energetic muons induce radioactive isotopes that can interfere with the sought-after signals. Especially the production of ^{11}C via muon spallation of the largely abundant ^{12}C can be problematic. Therefore the benefits of a background reduction technique in combination with a muon track reconstruction, which were both developed by the collaboration of the similar Borexino experiment, are studied for SNO+.

The following chapter will briefly introduce the relevant aspects of neutrinos physics, after which these are discussed in the context of SNO+ in chapter 3, that is also introducing the SNO+ experiment itself. Chapter 4 presents the fundamentals of organic liquid scintillator physics, that are needed in chapter 5. Here the mentioned investigations on the temperature quenching are explained and it is followed by chapter 6, concerning muon induced backgrounds in SNO+.

CHAPTER 2

Neutrino physics

As it was mentioned in the introduction, the SNO+ experiment delivers the broader scope for this thesis and therefore, of course, the motivation for the individual investigations. In order to understand why these studies are performed, the physics behind the direct goals of SNO+ have to be introduced, which will be done here in a brief manner. More comprehensive literature will be mentioned and referenced in the following sections on the main physics topics of SNO+.

Right from the beginning, neutrinos took a special place in particle physics. For the first 25 years after their postulation by Pauli in 1930, they remained experimentally undiscovered until Reines and Cowan successfully detected them in 1956 [Rei56]. Even until today, many questions are unanswered concerning the nature of neutrinos, which are to our best knowledge today, the most abundant matter particle in the universe*. Are they stable? Do they exhibit a magnetic moment? Are there only three kinds? The probably most central open question is the nature and size of the neutrino mass. The evidence that at least one neutrino type must have a non-vanishing mass, was only found in the late 20th century and was awarded with the Nobel Prize in physics to Takaaki Kajita and Arthur B. McDonald. Nevertheless, it is still unknown if this mass is generated via a Dirac- or Majorana mechanism and the neutrino could be the only fundamental fermion which is also its own anti-particle.

The investigations of so-called double beta decays (abbr. $\beta\beta$ -decays) holds great potential for answering these questions and especially the search for the 'neutrinoless double beta decay' (abbr. $0\nu\beta\beta$ -decay) might decide which of the mass generating mechanisms is realised in nature. If the neutrino is of Majorana type, the observation of the $0\nu\beta\beta$ -decay would be the only way of an experimental determination of the effective Majorana-mass of the electron neutrino, and thus opening a door to physics beyond the standard model of elementary particles. Modern chemical techniques allow interesting isotopes to be stably dissolved into liquid scintillator, and as SNO+ will be filled with even this medium, it possesses great potential in the search for $0\nu\beta\beta$ -decay. Due to the importance of this measurement, the SNO+ collaboration prioritises this goal over the other following potential physics discoveries.

Compared with water, much smaller energy depositions are able to excite the organic molecules in liquid scintillator, and it is for that reason that experiments as KamLAND, Borexino and SNO+ have a much lower detection threshold for low energy signals. These might stem from solar neutrinos, neutrinos produced in nuclear power plants or the radioactive contaminants in the earth crust and mantle or might even be emitted from supernovae. All of these are potential signals in the SNO+ experiment, and a more detailed discussion is presented in the following sections of this chapter. Before that, a short general introduction shall be given.

*This is intentionally ignoring all indications of dark matter and dark energy which, if ever discovered, likely disprove this statement.

In the original and most simple version of the standard model of particle physics, neutrinos are fermions, have no mass and are ordered into doublets with their leptonic partners

$$\begin{pmatrix} \nu_e \\ e^- \end{pmatrix} \quad \begin{pmatrix} \nu_\mu \\ \mu^- \end{pmatrix} \quad \begin{pmatrix} \nu_\tau \\ \tau^- \end{pmatrix}$$

and equivalently for antiparticles

$$\begin{pmatrix} e^+ \\ \nu_e^c \end{pmatrix} \quad \begin{pmatrix} \mu^+ \\ \nu_\mu^c \end{pmatrix} \quad \begin{pmatrix} \tau^+ \\ \nu_\tau^c \end{pmatrix}$$

Here, the superscript c refers to the conjugation of all possible charges. Every 'family' carries a so-called Lepton-number $L_{e,\mu,\tau} = 1$ and $L_{e^c,\mu^c,\tau^c} = -1$ for the anti-particles. In this theory particles are not changing in between families and particles and anti-particles are distinguishable from each other.

Though already in 1957, Pontecorvo proposed a possible oscillation between neutrinos and anti-neutrinos, which later proved to be wrong [Pon57]. Not much later, in 1962, Maki, Nakagawa and Sakata started to theoretically investigate oscillations in between neutrino families [Mak62]. This is only possible if at least one non-vanishing mass eigenstate $|v_i\rangle$ ($i = 1, 2, 3$) exists, that is connected to the interaction eigenstates via

$$|v_\alpha\rangle = \sum_i U_{\alpha i} |v_i\rangle \quad (2.1)$$

with $U_{\alpha i}$ as the mixing matrix that is commonly known as PMNS-matrix, honouring the former mentioned physicists [Boe92]. The experimental evidence for the existence of these oscillations was found by the Super-Kamiokande- [Fuk98] and SNO experiment [Ahm02] and these were therefore, as already mentioned, rewarded the Nobel Prize in 2015.

The existence of such non-vanishing neutrino masses is a necessary prerequisite for the neutrinoless double beta decay ($0\nu\beta\beta$), which would, in case it is ever discovered, directly decide between Dirac- and Majorana mass (see next section) and also deliver a direct measurement of the effective Majorana electron neutrino mass. But also the much more common and already observed double beta decays with two neutrinos ($2\nu\beta\beta$) are of interest, as they help understanding the internal structure of the nuclei and their configurations. The next section shall briefly introduce the theoretical and phenomenological concepts of the $0\nu\beta\beta$ decays.

2.1 Neutrinoless double beta decay

In quantum field theory, fermions are described by four component spinors $\psi(x)$ that have to satisfy the Dirac equation, which can be derived from the respective Lagrangian density, that is of the following shape in case of a free fermion without further interactions

$$-\mathcal{L} = \bar{\psi}(\gamma_\mu \partial^\mu + m_D)\psi \quad (2.2)$$

here and hereafter $\hbar = c = 1$ is assumed, m_D is the so-called Dirac mass and $\bar{\psi} = \psi^\dagger \gamma_0$ is the adjoint spinor to ψ . Furthermore is

$$\partial^\mu = \frac{\partial}{\partial x_\mu} \quad , \quad \gamma_k = \begin{pmatrix} 0 & -i\sigma_k \\ i\sigma_k & 0 \end{pmatrix} \quad \text{for } k = 1, 2, 3 \quad (2.3)$$

$$\text{and } \gamma_0 = \begin{pmatrix} \mathbb{I} & 0 \\ 0 & -\mathbb{I} \end{pmatrix} \quad , \quad \gamma_5 = \gamma_0 \gamma_1 \gamma_2 \gamma_3 = \begin{pmatrix} 0 & -\mathbb{I} \\ -\mathbb{I} & 0 \end{pmatrix} \quad (2.4)$$

where σ_k symbolises the Pauli spin matrices and \mathbb{I} the unity matrix [Sch97].

When taking a closer look at the mass terms, it becomes clear that they need to satisfy only two conditions. They need to be Lorentz invariant and Hermitian. Besides the obvious $\bar{\psi}\psi$ and $\bar{\psi}^c\psi^c$, also mass terms including $\bar{\psi}^c\psi$ and $\bar{\psi}\psi^c$ satisfy this condition. In the first two cases m_D has to be real to deliver the two conditions and these are called Dirac mass terms:

$$- \mathcal{L}_D = \frac{1}{2} m_D (\bar{\psi}\psi + \bar{\psi}^c\psi^c) \quad (2.5)$$

and on the other hand

$$- \mathcal{L}_M = \frac{1}{2} (m_M \bar{\psi}\psi^c + m_M^* \bar{\psi}^c\psi) \quad (2.6)$$

are called Majorana mass term. The most general form of a mass term for neutrinos is then

$$- 2\mathcal{L}_{mass} = \frac{1}{2} (\bar{\psi} m_D \psi + \bar{\psi}^c m_D \psi^c + \bar{\psi} m_M \psi^c + \bar{\psi}^c m_M^* \psi) \quad (2.7)$$

containing three real parameters (m_D, m_1, m_2) if ($m_M = m_1 + i m_2$). It is insightful to write the last equation in matrix form:

$$- 2\mathcal{L}_{mass} = \frac{1}{2} (\bar{\psi}, \bar{\psi}^c) \begin{pmatrix} m_D & m_M \\ m_M^* & m_D \end{pmatrix} \begin{pmatrix} \psi \\ \psi^c \end{pmatrix} \quad (2.8)$$

if this matrix is diagonalised, one finds the eigenvalues $m_D \pm |m_M|$ and the respective eigenvectors are then

$$\begin{pmatrix} \chi_+ \\ \chi_- \end{pmatrix} = \frac{1}{\sqrt{2}} \begin{pmatrix} e^{-i\theta} \psi + e^{i\theta} \psi^c \\ -e^{-i\theta} \psi + e^{i\theta} \psi^c \end{pmatrix} \quad (2.9)$$

with $\tan 2\theta = m_2/m_1$. These are the so-called Majorana fields and are eigenstates of the charge conjugation with opposite eigenvalues and are therefore describing Majorana particles. Moreover it is helpful to know the chiral projections on the eigenvectors of the helicity operator

$$\psi_L = \frac{1}{2} (1 - \gamma_5) \psi \quad , \quad \psi_R = \frac{1}{2} (1 + \gamma_5) \psi \quad (2.10)$$

and

$$(\psi_L)^c = \frac{1}{2} (1 + \gamma_5) \psi^c = (\psi^c)_R \quad , \quad (\psi_R)^c = \frac{1}{2} (1 - \gamma_5) \psi^c = (\psi^c)_L \quad (2.11)$$

With these in mind, the Dirac- and Majorana mass terms can be rewritten as

$$- \mathcal{L}_D = \frac{1}{2} m_D (\bar{\psi}_L \psi_R + \bar{\psi}_R \psi_L) \quad (2.12)$$

and

$$-\mathcal{L}_M^L = \frac{1}{2}m_L(\bar{\psi}_L\psi_R^c + \bar{\psi}_R^c\psi_L) \quad , \quad -\mathcal{L}_M^R = \frac{1}{2}m_R(\bar{\psi}_L^c\psi_R + \bar{\psi}_R\psi_L^c) \quad (2.13)$$

now with m_L and m_R real. Similar to equation 2.8, this can be formulated as a general mass term in matrix form as

$$-2\mathcal{L}_{mass} = \frac{1}{2}(\bar{\psi}_L, \bar{\psi}_L^c) \begin{pmatrix} m_L & m_D \\ m_D & m_R \end{pmatrix} \begin{pmatrix} \psi_R^c \\ \psi_R \end{pmatrix} + h.c. \quad (2.14)$$

where $(1 + \gamma_5)(1 - \gamma_5) = 0$ was used and thus arbitrary fields are $\bar{\psi}_L\phi_L = \bar{\psi}_R\phi_R = 0$, [Boe92]. Finally, if a global gauge transformation is applied on to the Lorentz scalars in equation 2.5 and equation 2.6, for example like

$$\psi \rightarrow e^{i\alpha}\psi \quad , \quad \bar{\psi} \rightarrow e^{-i\alpha}\bar{\psi}, \quad (2.15)$$

it turns out that $\bar{\psi}\psi \rightarrow \bar{\psi}\psi$ is invariant, but

$$\psi^c \rightarrow (e^{i\alpha}\psi)^c = e^{-i\alpha}\psi^c \quad \text{and also} \quad \bar{\psi}^c \rightarrow e^{i\alpha}\bar{\psi}^c \quad (2.16)$$

are obviously not. Therefore Dirac mass terms are connected to a conserved quantum number (Lepton number), but Majorana mass terms violate the Lepton number by $\Delta L = \pm 2$ two units. Dirac terms are responsible for transitions of leptons l as $l \rightarrow l$ and $\bar{l} \rightarrow \bar{l}$, but Majorana terms transform $\bar{l} \rightarrow l$ and $l \rightarrow \bar{l}$. The latter transitions are forbidden for charged leptons, but not necessarily for neutrinos (as they are neutral in all additive quantum numbers) [Sch97].

These much simplified considerations shall show how Majorana mass terms can be embedded into the well verified Dirac theory and therefore deliver a theoretical basement for the $0\nu\beta\beta$ -decays. The $2\nu\beta\beta$ -decays on the other hand can be described already in the classic Dirac theory. Much more comprehensive information can be found in [Moh04] and [Kim93], as well as in the already mentioned books and publications.

With these theoretical foundations in mind, the view shall now be directed towards nuclear beta decays which, as will be seen later, are of course directly related to the neutrino mass terms. It is instructive to start with the 'classic' single β^- -decay. Here a down-quark inside a neutron is changing into an up-quark, transforming the neutron into a proton while simultaneously emitting an electron and an electron anti-neutrino. This is illustrated in a Feynman-diagram in Fig. 2.1.1 and can be written at the nucleus level as

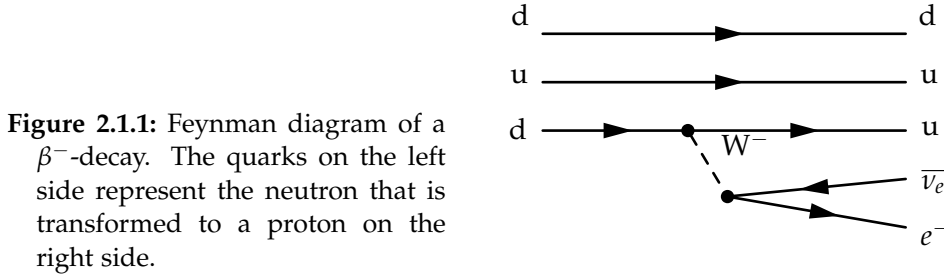
$$(A, Z) \rightarrow (A, Z + 1) + e^- + \bar{\nu}_e + Q \quad (2.17)$$

with A as the number of nucleons, Z the number of protons and Q is the amount of energy that is released in this reaction, the so-called Q -value:

$$Q = [m(Z, A) - Z \cdot m_e] c^2 - [m(Z + 1, A) - (Z + 1) \cdot m_e + m_e] c^2 \quad (2.18)$$

These equations and the Feynman diagram can be formulated in similar ways for the β^+ -decay or the electron capture (EC), in which a proton is turning into a neutron,

emitting an electron neutrino, and in case of the β^+ transformation also a positron. The 'classic' β -decay can also be seen as the birth place of the neutrino, as it was the electron energy spectrum that lead Pauli in 1930 [Pau30] to the proposal of an invisible and unknown particle, which should later turn out to be the neutrino.



Already in 1935, Goepfert-Meyer proposed that two β -decays could happen at the same time in one nucleus [Goe35]. In the notation of before, in the case of two β^- -decays, this can be written as

$$(A, Z) \rightarrow (A, Z + 2) + 2e^- + 2\bar{\nu}_e + Q \quad (2.19)$$

which is, due to the two neutrinos in the final state, called neutrino accompanied double beta decay ($2\nu\beta\beta$). In some cases this is possible if the single β -decay is energetically forbidden, but the double disintegration would not be. For a better understanding the simplified Weizsäcker mass formula for isobaric nuclei ($A = \text{const.}$) shall be considered:

$$m(Z, A = \text{const.}) \approx \text{const.} + \alpha Z + \beta Z^2 + \delta_p \quad (2.20)$$

where β and $\alpha \approx 12 \text{ MeV}$ are constants and δ_p is the pairing energy for kindred nucleons as

$$\delta_p = \begin{cases} -\alpha A^{1/2}, & N, Z = \text{even} \\ 0 & N, Z = \text{odd \& even or even \& odd} \\ +\alpha A^{1/2} & N, Z = \text{odd} \end{cases} \quad (2.21)$$

with $N = (A - Z)$ denoting the number of neutrons and the labels even and odd referring to nuclei with an even number of neutrons and an even number of protons, and so forth. These labels are also used in a graphical representation of these mass parabolas, shown in Fig. 2.1.2. When viewed like this, it can be seen that nuclei with an odd number of nucleons A , have a stable isobar occupying the energetically lowest possible point in the parabola. Neighbouring isobars might move towards this global minimum via β^\pm -decay or EC. For nuclei with even numbered nucleons the situation is somewhat different, as the pair energy term in (2.21) leads to the manifestation of two parabolas, one with generally higher energies (odd,odd) and one at lower energies (even,even). In very rare cases, the configuration of an even-even nucleus is such that a single β^\pm -decay or EC to the neighbouring odd-odd nucleus is energetically forbidden as its energy level is higher. Then only a second

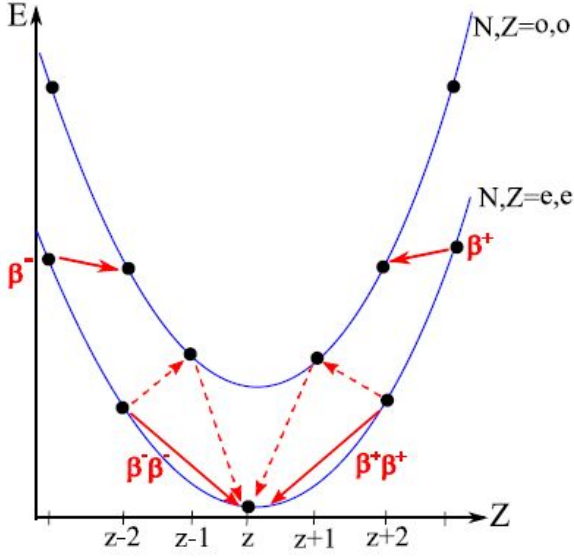


Figure 2.1.2: Mass parabola for nuclei with even numbered nucleons ($A=\text{const.}$). The isobars with odd numbers for protons (Z) and neutrons (N) are placed on an energetically higher parabola than even numbered ones. The solid red lines show allowed transitions via single β^\pm -decay or $\beta^\pm\beta^\pm$ -decays. Red dashed lines show energetically forbidden decays. Taken from [COB].

order weak interaction process is possible, changing the charge number by two, so-called double beta decays (double β^- -decay, double β^+ -decay or double EC).

The mentioned ‘very rare cases’ refer to 35 known isotopes for $\beta^-\beta^-$ disintegration and only 6 $\beta^+\beta^+$ -decay isotopes (these are always accompanied by β^+ -EC and double EC processes). The first direct evidence for neutrino accompanied double β -decay was found in 1987 by Elliott et al. [Eli87] in ^{82}Se . The measured extreme long half-life of $T_{1/2}^{2\nu} \sim \mathcal{O}(10^{20})$ y is characteristic for these kind of second order processes and results in extremely low event rates, which are presenting the main challenge for any experiments attempting a direct detection.

Only the, so far purely theoretical, neutrinoless double β -decays would show even longer half-lives of $\mathcal{O}(10^{24})$ y and were first proposed by Furry, already in 1939 [Fur39]. In this case no neutrinos leave the nucleus, which is possible if they are their own anti-particle and thus of Majorana type ($\nu_L \equiv \bar{\nu}_L, \nu_R \equiv \bar{\nu}_R$). Some kind of mechanism has to adapt the helicity of a, by a neutron emitted, right-handed $\bar{\nu}_R$ to the, by the other neutron absorbed, left chiral ν_L . Figure 2.1.3 shows a Feynman diagram illustrating this situation. In case of massive neutrinos, the probability of an admixture of the opposite helicity is already given by

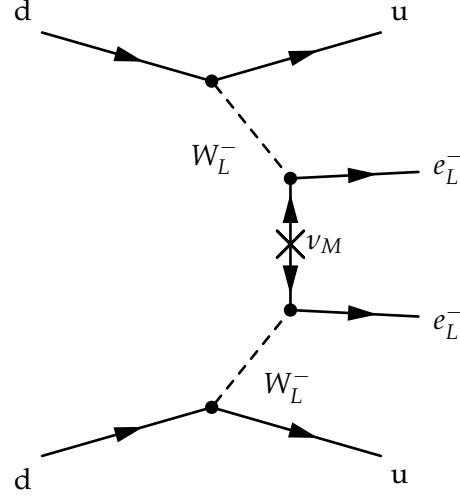
$$P = \frac{1}{2} \left(1 - \frac{v}{c}\right) \approx \left(\frac{m_\nu}{2E_\nu}\right)^2 \quad (2.22)$$

This possibility is commonly referred to as mass mechanism and here presented in a very much simplified way. Other theoretical possibilities to trigger $0\nu\beta\beta$ -decays exist, such as so far unobserved right-handed charged currents in Left-Right chiral symmetry models [Doi83], some Super Symmetry theories [Bab95] and even in models involving extra dimensions [Bha03].

From the experimental point of view it is important to mention that, due to the missing neutrinos, the two electrons in the final state of a $0\nu\beta\beta$ -decay carry all the released energy. Nearly all of the current experiments are of a calorimetric type that is

only able to measure the sum energy of the two electrons, which are then appearing as a line at the Q -value of the transition. For the far future, if $0\nu\beta\beta$ is ever discovered, the angular correlation between the electrons and their energy distribution might shed light into the underlying mechanism. Until then, the Q -value of these decays are a crucial experimental value in order to discriminate the signal from background events produced by other natural radioactivity with always much shorter half-lives and thus higher event rate if even slightly occurring in the detector.

Figure 2.1.3: Feynman diagram of a neutrinoless double β^- -decay ($0\nu\beta\beta$). The cross at the centre marks the unknown mechanism of the helicity adaptation of the two neutrinos and is therefore labeled with the sign for a Majorana neutrino ν_M . The sum energy of the two electrons in the final state is defined by the Q -value of this transition and results in a monoenergetic line, in case only the sum is measured.



Finally, a very brief view at the calculation of the half-lives shall be taken. For the $2\nu\beta\beta$ transitions it can be derived to

$$(T_{1/2}^{2\nu})^{-1} = G^{2\nu}(Q, Z) \cdot |M_{GT}^{2\nu}|^2 \quad (2.23)$$

where $M_{GT}^{2\nu}$ is the Gamov-Teller matrix element and $G^{2\nu}(Q, Z) \propto Q^{11}$ is the phase-space factor, illustrating how much the half-life depends on the Q -value in case of the $2\nu\beta\beta$ -decay. Even though related, the situation is quite different for the $0\nu\beta\beta$ case:

$$(T_{1/2}^{0\nu})^{-1} = G^{0\nu}(Q, Z) \cdot |M_{GT}^{0\nu} - M_F^{0\nu}|^2 \cdot \left(\frac{|m_{\beta\beta}|}{m_e}\right)^2 \quad (2.24)$$

with $M_F^{2\nu}$ symbolising the Fermi matrix element and the much less sensitive (still strongly dependent) $G^{0\nu}(Q, Z) \propto Q^5$. Additionally the factor electron mass m_e and the so-called effective Majorana neutrino mass $|m_{\beta\beta}|$ contribute. The latter one is composed of the neutrino mass eigenstates weighted with the aforementioned PMNS matrix-elements as

$$|m_{\beta\beta}| = \left| \sum_i U_{ei}^2 \cdot m_i \right| \quad (2.25)$$

Therefore a measurement of the half-life leads to the determination of the effective Majorana mass, in case the matrix elements and phase space factors are well known.

The PMNS matrix is commonly defined with 3×3 elements consisting of combinations of three mixing angles θ_{12} , θ_{13} and θ_{23} , as well as a Dirac Charge-Parity

(CP) violating phase δ and possibly two Majorana CP-violating phases λ_2 and λ_3 . This matrix can only be diagonalised if massive neutrinos are of Majorana type. As explained before, this matrix is central for neutrino oscillation and the probability for a flavour transition of neutrinos in vacuum can be written as

$$P(\nu_l \rightarrow \nu_{l'}) = \left| \delta_{ll'} + \sum_{i \neq k} U_{li} \left(\exp \left(-i \frac{\Delta m_{ki}^2 L}{2E} - 1 \right) \right) U_{li}^* \right|^2 \quad (2.26)$$

where L is the distance between neutrino generation and detection and $\Delta m_{ki}^2 = (m_i^2 - m_k^2)$. Thus the probability for an oscillation depends on the three mixing angles, the CP-violating phases, the neutrino energy, the distance at their detection from the source and the two independent squared mass differences Δm_{12}^2 and Δm_{23}^2 . Historically these mass-squared differences are associated with the source of neutrinos from which they were first measured and therefore often referred to as solar $\Delta m_{\text{solar}}^2 \equiv \Delta m_{12}^2$ (commonly the smaller splitting) with $m_1 < m_2$ and the atmospheric $\Delta m_{\text{atmos}}^2 \approx \Delta m_{23}^2 \approx \Delta m_{13}^2$ splitting. The latter ambiguity is due to the fact that to this day, oscillation experiments are not able to measure the sign of the splittings, and therefore three possible mass orderings for neutrino masses remain [Bil12]:

Quasi degenerate in case the lightest neutrino mass is $m_{\text{lightest}} \gtrsim 0.1$ eV and thus the splittings are much smaller than the neutrino masses: $m_1 \approx m_2 \approx m_3$

Normal spectrum if $m_{\text{lightest}} = m_1 < m_2 \ll m_3$; $\Delta m_{12}^2 \ll \Delta m_{23}^2$

Inverted spectrum if $m_{\text{lightest}} = m_3 \ll m_1 < m_2$; $\Delta m_{12}^2 \ll |\Delta m_{13}^2|$

Figure 2.1.4 shows a parameter space for the effective Majorana neutrino mass as a function of the lightest neutrino mass $m_{\text{min}} = m_{\text{lightest}}$, incorporating the most recent values for the oscillation parameters. Also the most stringent bound for $|m_{\beta\beta}|$ from $0\nu\beta\beta$ searches is indicated, provided by the GERDA experiment [Mac14].

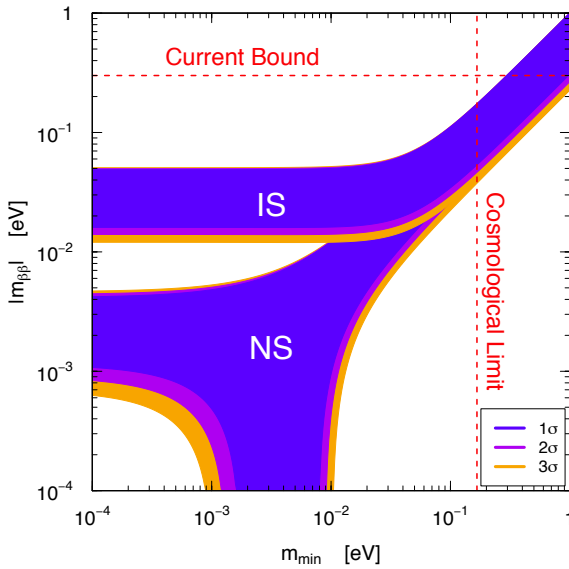


Figure 2.1.4: Effective Majorana mass as function of the lightest neutrino mass $m_{\text{min}} = m_{\text{lightest}}$ for the normal- (NS) and inverted spectrum (IS). For the NS $m_{\text{min}} = m_1$ and for the IS $m_{\text{min}} = m_3$ is assumed. The quasi degenerate region is not labelled but can be found in the upper right region of the plot where IS and NS overlap. The current bound on $|m_{\beta\beta}|$ is taken from [Arn11] and the Cosmological Limit from [Han10]. Taken from [Bil12].

At the end of this section, a very brief look at the current experiments and the involved isotopes for the search of $0\nu\beta\beta$ shall be taken. Table 2.1.1 summarises some of the most important values for the isotopes that are currently considered, or already in practical use in experiments.

Table 2.1.1: List of isotopes that are currently in use for $0\nu\beta\beta$ searches, their $0\nu\beta\beta$ Q-value and isotopic abundance. Data taken from [Del16].

isotope	Q-value [MeV]	nat. abundance [%]	current experiments
^{76}Ge	2.039061(7)	7.8	GERDA-II, MAJORANA-D.
^{130}Te	2.52697(23)	34.5	CUORE, SNO+
^{136}Xe	2.45783(37)	8.9	EXO-200, nEXO, KamLAND-Zen, NEXT, PandaX-III
^{100}Mo	3.03440(17)	9.6	AMoRE
^{82}Se	2.99512(201)	9.2	SuperNEMO
^{48}Ca	4.27226(404)	0.187	CANDLES-III

Finally the most important challenges for experiments attempting the measurement of the so far unobserved neutrinoless double β -decay shall be discussed. As has been mentioned earlier, due to the nature of this process, the expected half-lives (supported by current limits) are extremely long and result in extremely low count rates in experiments, even if the observed mass is significant. This has severe implications for experimental efforts and the following formula estimates the half-life sensitivity if background events are distributed evenly in the Region Of Interest (ROI):

$$T_{1/2}^{(\text{det})} \propto \varepsilon \alpha \sqrt{\frac{M \cdot t}{\Delta E \cdot B}} \quad (2.27)$$

where α is the isotopic abundance, ε is the detection efficiency, M is the observed mass, t is the measurement time, ΔE is the energy resolution in the ROI and B the background in the same region. While α and ε affecting the reachable half-life linearly, the other variables contribute only with a square root dependence. Simplifying the situation coarsely, one can state that a high isotopic abundance, high efficiency, high observable mass, good energy resolution and ideally no background are the key ingredients for a successful experiment. In reality many constraints on one or the other variable are given, by various factors ranging from detector technology to cost for isotopic enrichment to background reduction. These factors will be discussed again in section 3.2 in the context of the SNO+ experiment.

2.2 Solar neutrinos

It is difficult to only briefly describe the importance of the sun to humankind and all life on earth. Although it is omnipresent, we are rarely aware of the spectacular processes taking place inside the sun every second. Our ancestors- and our modern lives depend crucially on the consistency of the energy production and dissipation inside the sun. For obvious reasons the tools for investigations are limited and beside much progress in the last century, a lot of questions remain. Is the CNO cycle realised in our sun and how much does it contribute to the energy production? What are the exact values of the solar metallicity? And many more.

Theoretical models such as the Standard Solar Model (SSM) developed e.g. by Bahcall et al. [Bah05] provide the theoretical foundations of our understanding of the sun and are benchmarked by observations. The chemical composition of the surface is known through spectroscopy of visible and UV light from the sun and the internal hydrodynamical processes can be investigated to some extent by helio-seismology. Low energy collider experiments such LUNA [For03] provide substantial input through precise measurement of the relevant cross-sections of the thermo-nuclear reactions which are fundamental for the understanding of the energy production inside the sun. As these nuclear reactions almost always involve neutrinos, the observation of solar neutrinos is another completely independent input and the only direct way of 'looking into the sun'.

The main energy production process in the sun is given by hydrogen fusion:



which is starting the so-called **pp**-chain and the electron-neutrinos in the final state are commonly named after the reaction they are produced in. This reaction is feeding the next fusion process in more than 99% of the cases and the remaining fraction is produced by the so-called **pep**-reaction, leading to almost the same products:



The, through the previous two reactions produced, deuterons are fusing with protons to helium



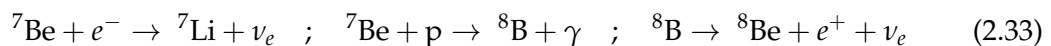
which is in turn in most cases consumed by



and commonly referred to as pp-I branch. The next most common reaction after (2.30) is



which is starting a chain that produces the important ${}^7\text{Be}$ and ${}^8\text{B}$ neutrinos via



And a last path for the helium that is produced in (2.30) is the so-called **hep**-reaction



An overview of the energy spectrum of the neutrinos generated in these reactions is shown in Figure 2.2.1, which is also including those produced in the CNO-cycle. This reaction cycle is possible if heavier elements such as nitrogen, carbon and oxygen are abundant in the star, and takes place in the inner layers or the core of the sun. It is a catalytic reaction that, in a simplified description, fuses four protons to helium, two positrons and two neutrinos, using carbon, nitrogen and oxygen as catalysts. Several variations of this scheme exist and in some of them also fluorine is produced, which generates the ${}^{17}\text{F}$ neutrino flux shown in Fig. 2.2.1. A comprehensive explanation of the complex fusion burning network is given e.g. in [Mau05].

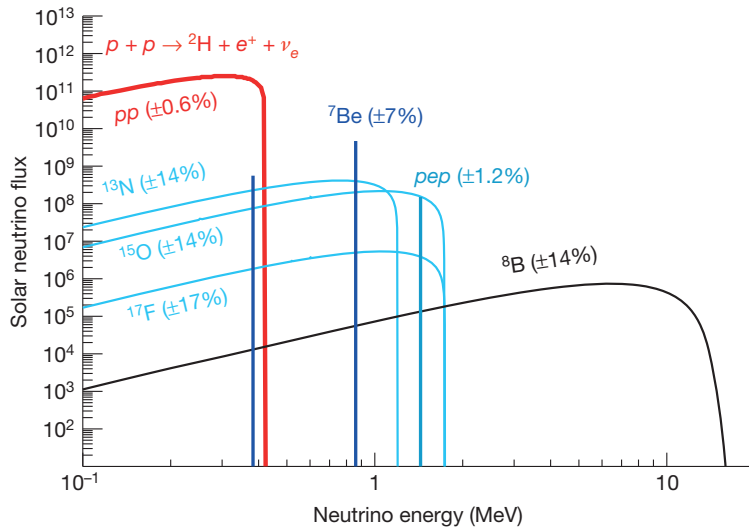


Figure 2.2.1: Solar neutrino fluxes as function of energy. The flux unit for mono-energetic lines is $[\text{cm}^{-2} \text{s}^{-1}]$ and for continues fluxes $[\text{cm}^{-2} \text{s}^{-1} \text{MeV}^{-1}]$. The given uncertainties stem from the underlying SSM [Ser11]. Taken from [Bel14].

The, through the described fusion processes (and β -decays), generated neutrinos are purely of electron-neutrino type, and in the middle of the last century it was believed that a measurement of those should account for the full flux expectation. The first solar neutrino detectors, such as the famous radiochemical experiment of R. Davis Jr. [Dav68], as well as the GALLEX [Ham99] and SAGE [Aba91] experiments, were only sensitive to ν_e . Their results showed a 30%-50% deficit compared to the expected rate from the SSM predictions, leading to the so-called solar neutrino problem. This was finally resolved by the SNO experiment around the millennium [Ahm02], as it was sensitive to all three kinds of neutrinos and could show that the total rate of ν_x ($x = e, \mu, \tau$) from ${}^8\text{B}$ solar neutrinos is in good agreement with SSM prediction, and that therefore neutrinos must have had oscillated on the way from their production to earth. In 1986 Mikheev and Smirnov [Mik86] used a theory initially developed

by Wolfenstein [Wol78], and proposed that the ν_e already oscillate into ν_μ and ν_τ inside the suns extremely dense matter due to an resonance enhanced oscillation effect. Neutrinos with energies above 5 MeV interact with the very dense electrons in the solar matter, and can change their flavour completely, reducing the ν_e flux to about one third. In this energy region the survival probability for ν_e approximates $P(\nu_e \rightarrow \nu_e) = \sin^2 \theta_{12}$. Low energy solar neutrinos with $E_{\nu_e} < 1$ MeV are little or not affected by this resonance effect and their flux reduces to about a half on their path from the sun to the earth as they oscillate in vacuum. Due to this long path, their oscillation is averaged and the survival probability is $P(\nu_e \rightarrow \nu_e) = 1 - 1/2 \sin^2 \theta_{12}$. The transition region in between those two regimes is expected to be smooth. The ratio of matter to vacuum effects is given by the equation

$$R = \frac{2\sqrt{2} G_F n_e E_\nu}{\Delta m_{12}^2} \quad (2.35)$$

in which G_F represents the Fermi coupling constant, n_e is the electron density, E_ν the neutrino energy and Δm_{12}^2 is the previously introduced mass splitting between ν_1 and ν_2 neutrino mass eigenstates. The two involved oscillation parameters are thus θ_{12} and Δm_{12}^2 . The best known value for the latter one is provided by the KamLAND experiment with $\Delta m_{12}^2 = (7.59_{-0.21}^{+0.21}) \times 10^{-5} \text{ eV}^2$ [Abe08]. After the initially larger parameter space for θ_{12} narrowed down, a so-called large mixing angle (LMA) solution was finally found to be realised and in a combined fit of all available solar neutrino data and in combination with the KamLAND results, the best fit value is now $\sin^2 \theta_{12} = 0.304_{-0.012}^{+0.012}$ [Gon14]. An overview of this situation is given in Fig. 2.2.2, showing the predicted survival probability in a current MSW-LMA model as a function of neutrino energy (pink band) and Borexino data points.

The large uncertainties of the data points in Fig. 2.2.2 do not allow to precisely pin down the survival probability at all energies and thus the shape of the function. Especially the transition region in between 1 MeV and 5 MeV is difficult to access but is actually the region with the highest sensitivity to modified models and new physics. Such models are presented e.g. by Friedland et al. [Fri04], proposing allowed flavour changing interactions which would lead to a significantly reduced pep-neutrino flux, shown in Figure 2.2.3. Furthermore, a theory involving sterile neutrinos by de Holanda and Smirnov [Hol11], modifies the survival probability in the same transition region. Thus a more precise detection of pep neutrinos could rule out and decide between different theories.

Moreover, the neutrinos from the CNO-cycle carry a lot of information about the interior of the sun, as they are produced in the core region of the star. Their production is very sensitive to the core metallicity and temperature. Interest in them has grown more and more as they are able to provide an independent measurement of the abundance of heavier elements, which has been a subject of debate as newer SSM predict much lower metallicities and contradict helio-seismic data. More information on the solar abundance problem can be found e.g. in [Ser09]. Finally, solar CNO-neutrinos have never been observed and their measurement would qualify as a discovery.

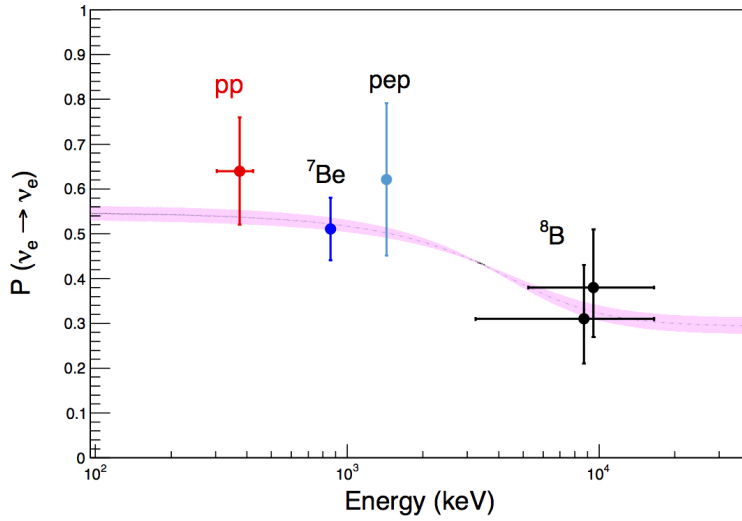


Figure 2.2.2: Survival probability for solar ν_e as function of E_{ν_e} . The pink band shows the $\pm 1\sigma$ prediction from the MSW-LMA solution for ${}^8\text{B}$ solar neutrinos, considering their production region in the sun [Ber12]. All data points are from Borexino and the horizontal error bars show the energy range that was used for the measurement. Taken from [Bel14].

2.3 Geo- and reactor neutrinos

Beside those produced with particle accelerators, geo- and reactor neutrinos represent the strongest terrestrial neutrino sources. In both cases they stem from β -decays of radioactive isotopes, either from naturally occurring potassium, uranium and thorium in the earth's crust and mantle, or from fission products in nuclear power plants. These electron anti-neutrinos are generally detected via the so-called inverse beta decay (IBD):



which has a very distinct final state signature, as the positron soon annihilates with an electron and the neutron is in most cases captured by a hydrogen nucleus, releasing a characteristic 2.2 MeV γ -ray. The threshold energy for this reaction is $E_{\bar{\nu}_e} = 1.8$ MeV.

Geo-neutrinos stem from the β -decays of ${}^{40}\text{K}$, ${}^{238}\text{U}$ and ${}^{232}\text{Th}$ and daughter isotopes in their decay chains and were first detected by the KamLAND experiment [Ara05a; Abe08], which was later followed by the Borexino collaboration [Bel10; Bel13b]. These radioactive decay chains are considered to significantly contribute to the heat production inside the earth and the emitted neutrinos are a new and independent probe for the abundance and distribution of these isotopes. Due to low statistics and large systematic uncertainties, it is until now not possible to discriminate between different geological models. Analysis combining the two results has better prediction power and more measurements, from different sites, would provide a lot of new insights [Gan11b; Fio12].

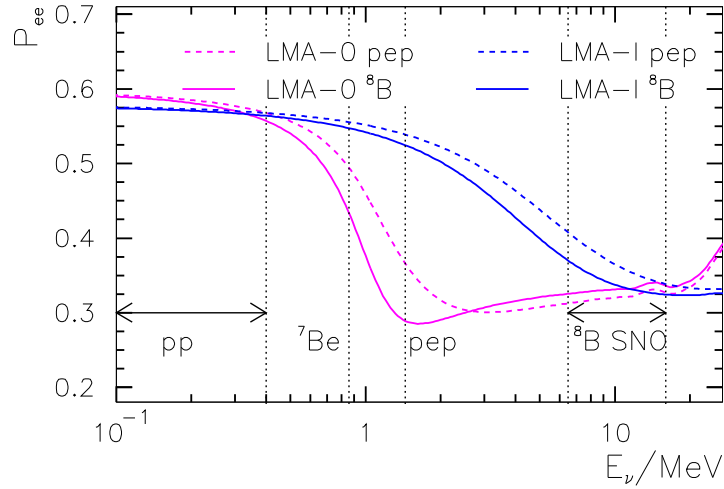


Figure 2.2.3: Survival probability for ^8B and pep solar neutrinos as function of energy and calculated with two models. LMA-I corresponds to the classic MSW-LMA theory as in Fig. 2.2.2. LMA-0 is the alternative model involving flavour changing interactions, proposed by de Holanda and Smirnov. It is clearly visible that a measurement of pep neutrinos provides the most powerful probe, given a small uncertainty. More details can be found in [Hol11], which is also where this graph is taken from.

Reactor neutrinos are an irreducible background for the geo-neutrino detection (and vice versa), but also present a powerful signal themselves. In recent years, the medium baseline reactor experiments Double Chooz [Abe12], RENO [Ahn12] and Daya Bay [An12] have measured the $\bar{\nu}_e$ disappearance of reactor neutrinos and were able to determine the surprisingly large mixing angle θ_{13} with unprecedented precision. These experiments were dedicated to measure the neutrino oscillation parameters and consist of one or several near detectors close to a nuclear power plant ($L = \mathcal{O}(100)$ m) providing the flux normalisation, and one or several far detectors ($L = \mathcal{O}(1.5)$ km) to measure the, due to the oscillation, reduced $\bar{\nu}_e$ -flux. The most precise measurements at the near detectors indicate a 6% lower flux compared to the best predictions for the neutrino flux emitted by the power plants, commonly referred to as reactor anti-neutrino anomaly [Men11].

Finally it shall be mentioned that also other liquid scintillator experiments such as KamLAND can provide values for θ_{13} , but mainly help to constrain Δm_{12}^2 and θ_{12} with their measurement of reactor neutrinos [Gan11a].

2.4 Supernova neutrinos

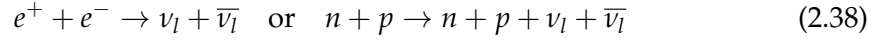
The end of a life of a massive star is marked by gigantic explosion, known as supernova. Within our current knowledge, supernovae are believed to be the highest energy processes in the universe, releasing 99% of its gravitational binding energy in

the form of neutrinos [Moh04]. Therefore supernova neutrinos carry a tremendous amount of information about the processes taking place during the explosion.

During their lifetime, massive stars produce their energy by fusion of hydrogen to helium, and as they evolve, burning heavier and heavier elements until they eventually reach iron (if $m_{\text{star}} > 5 - 10 \times m_{\odot}$, the mass of our sun). As iron is the most stable nucleus, it can not be fused further to a heavier element. Before that, every time a heavier element is produced, it settles in the core of the star due to gravity, increasing its mass and density until it reaches the Chandrasekhar mass of $\approx 1.4 m_{\odot}$. From that point on, the internal pressure in the core is smaller than the gravitational pull and the pressure is increased further through various processes, one of which is the absorption of electrons by protons



producing neutrons and ν_e , known as deleptonisation neutrinos [Moh04]. The core collapse is finally ended by the hard-core nuclear repulsion and a so-called bounce back process is started but yet not fully understood, leading to the explosion. Neutrinos of other flavour are also produced, in processes that are possible in the very special conditions of matter inside a collapsing and exploding star, such as



These processes also thermalise the back and forth bouncing neutrinos, inside a so-called neutrino sphere with a radius much larger than that of the collapsed core.

Much of these processes is quite theoretical as only one supernova was observed during the age of neutrino detectors and all of those were insensitive to the neutrino flavour (most of them were water Cherenkov detectors). While the supernovae 1987A was unambiguously observed by the Kamiokande-II [Tot87] and IMB [Bio87] experiments in coincidence, the detection by the Baksan [Ale88] and Mont-Blanc [Agl87] experiments are controversial [Kri04]. Even with only 19 detected events via the reaction



a broad variety of information can be derived from their energy (all are less than 60 MeV) and the time window they were detected in (10-12 s). From this minimal information, many constraints can be derived, such as: upper bounds on neutrino mass, magnetic moment and charge, neutrino decay modes and lower bounds on neutrino lifetime [Moh04].

With so many unknowns about the internal mechanisms of supernovae and so much information that can be gained with advanced modern day detectors, the arrival of a next supernova within a distance of 10 – 20 kpc is highly awaited. In order to gain as much information as possible from such a rare event, neutrino detectors are organised in a supernova early warning system (SNEWS) network [Ant04], ensuring the best coverage from the neutrino physics community and to inform other astronomers about the detection. This way, ideally, another supernova will be studied through neutrinos and classic astronomical instruments, collecting as much information as possible.

CHAPTER 3

The SNO+ experiment

THIS chapter shall introduce the SNO+ experiment and its physics goals, which are the main motivation for this work and the measurements and simulations that are described in the later chapters 5 and 6. The location and hardware setup of the SNO+ project offer unique opportunities to contribute to the future of neutrino physics. It was initially perceived as the successor of SNO and therefore mainly as a solar neutrino experiment, but in this section the rich and diverse possibilities for SNO+ will be laid out in a brief manner. Much of the following information can also be found in a recent review publication by the SNO+ collaboration [And16].

3.1 Detector setup

The SNO+ collaboration inherited most of the detector infrastructure from the original SNO experiment, which was built in the 1990s and operated till 2006. In order to be able to use the same detector with liquid scintillator instead of heavy water, some changes to the hardware had to be made, as well as sensible updates to the read-out electronics and a full replacement of the computing hardware. The most important modifications will be explained after the following overview of the setup.

The detector is situated at SNOLab, a deep underground physics laboratory inside the active Creighton nickel mine, in Sudbury, Ontario, Canada. The hard rock overburden of 2.092 km (≈ 6 km.w.e.) provides an excellent shielding from cosmic rays and reduces the muon flux to about $63 \mu/d$ going through the volume of the detector, as it has been measured by SNO [Arh09]. Inside a large excavation, the main components are the following, see Fig. 3.1.1:

- (1) **The detector deck** is containing all read-out electronics and high voltage supplies, the cover-gas system, multiple calibration systems and provides access to the neck of the acrylic vessel (4).
- (2) **A urylon liner** on the cavity wall is sealing the setup from radon and other gases diffusing into the volume and is holding back the shielding water.
- (3) **PSUP with PMTs** - the geodesic photomultiplier support structure (PSUP) with a diameter of about 18 m is holding ≈ 9300 PMTs which are facing inwards to observe light generated in the acrylic vessel (4). A small number of 70 PMTs is mounted on the outside of the PSUP and is looking outwards, mainly to detect the Cherenkov-light of incoming muons.
- (4) **The acrylic vessel (AV)** is a 12 m diameter acrylic sphere, with a wall thickness of 5.5 cm, that will be first filled with ultra-pure water and in a later phase with liquid scintillator.
- (5) **The cavity** will be filled with ≈ 7000 t of ultra pure water, which is also going in between the PSUP and the AV. This provides shielding from ambient radioactivity and is cooling the PMTs on the PSUP to a temperature of about 13° C.
- (5) **The hold-up ropes** are suspending the AV inside the cavity. Not shown are the **hold-down ropes** which are going to hold the AV down when it will be filled with liquid scintillator, as it is lighter than water.

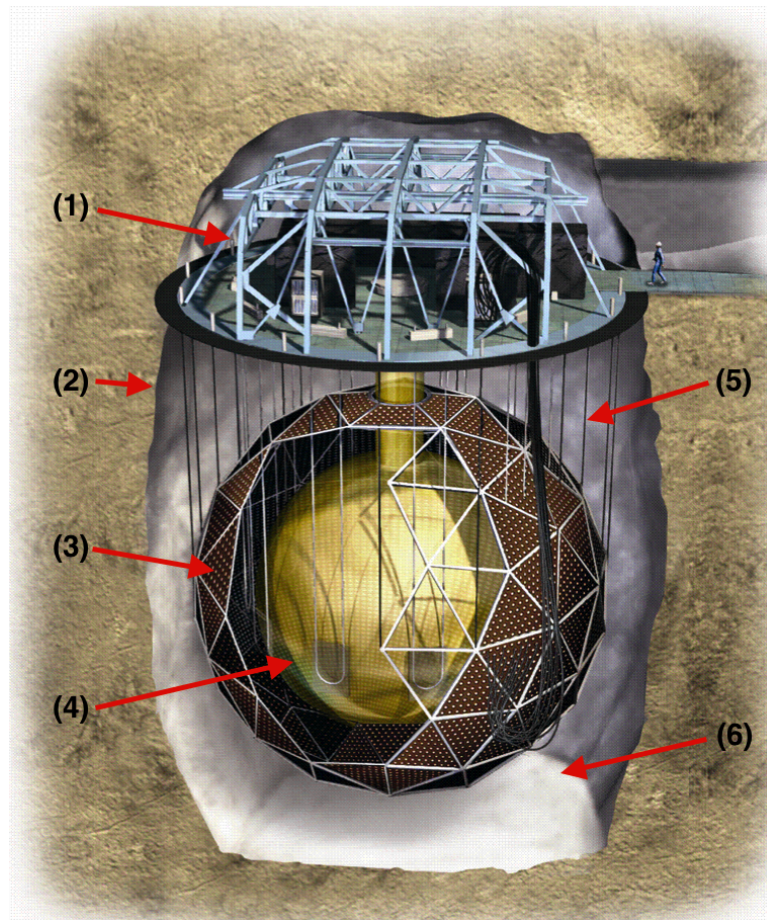


Figure 3.1.1: An artistic view of the SNO detector, taken from [G O]: (1) - detector deck (2) - urylon liner on cavity wall (3) - PMT support structure with PMTs (4) - acrylic vessel (5) - hold-up ropes. The only major structural change for SNO+ is not shown, these are ropes holding down the buoyant acrylic vessel in case it is filled with LAB.

The largest modification to the hardware was the installation of a rope net, that holds down the acrylic vessel (AV) when it will be filled with liquid scintillator. LAB is less dense than water ($\rho_{LAB} \simeq 0.86 \text{ g/cm}^3$ at 12°C) and thus the AV will be very buoyant inside the water shielding. The 40 mm strings are made of high purity Tensylon and are anchored in the floor of the cavity.

Other adaptations include a completely new calibration system, which is manipulating a variety of β, γ, α - and neutron calibrations sources such as ^{60}Co , ^{57}Co , ^{24}Na , ^{48}Sc and others, covering an energy range of 0.1 MeV to 6 MeV. This is completed by an optical calibration which is injecting LED and laser pulses into the detector via optical fibres. And finally it shall be mentioned that PMTs that broke during the operation of SNO are being repaired or replaced.

The main detection medium in SNO+ will be a liquid scintillator mixture based on LAB with 2 g/l 2,5-diphenyloxazole (PPO) and optionally a secondary solute as a wavelength shifter. This basic solution offers many advantages as it is compatible with acrylic, has a high light yield of about 10 k optical photons per MeV deposited energy, is available in high purity and exhibits favourable optical properties. As the detailed properties of different mixtures are not only crucial for SNO+ but also for this thesis, the whole chapter 4 is dedicated to liquid scintillator in general and LAB mixtures in particular.

In order to reach the same radio-purity levels as the comparable experiments Borexino and KamLAND, an industrial petrochemical plant has been installed underground, at the SNOLab site. It is capable of multi-stage and vacuum distillation to remove heavy elements, residual water and gases are removed via N₂/steam gas stripping process and finally a micro-filtration is used to eliminate suspended fine particles [For15]. The collaboration expects to reach purity levels of 10⁻¹⁷ g/g_{LAB} for the ²³⁸U and ²³²Th decay chains, as well as 10⁻¹⁸ g/g_{LAB} for ⁴⁰K, 10⁻²⁴ g/g_{LAB} for ³⁹Ar and 10⁻²⁵ g/g_{LAB} for ⁸⁵Kr.

Before the scintillator takes its place as active medium inside the AV, the whole detector will be filled with ultra pure water for a commissioning phase in which backgrounds are analysed and the opportunity to detect supernova neutrinos and some exotic physics exists. As of the moment of this thesis, the water fill is expected to be finished by July 2016, and the water phase will be continued till the end of this year. After that a short pure scintillator phase during 2017 will be used to again assess backgrounds and taking data of the possible physics signals. Later in 2017, the pure scintillator will be loaded with natural tellurium to about 0.3 % (by weight) to search for $0\nu\beta\beta$ -decays in ¹³⁰Te. As this loading changes the possible physics program, Table 3.1.1 gives a short overview of the phases and the available physics therein.

Table 3.1.1: Overview of the SNO+ physics program according to the planned phases. As it is obvious that some signals can only be seen with liquid scintillator in the AV, in the Te-loaded phase the $2\nu\beta\beta$ signal and significantly increased low energy backgrounds are the main causes why a measurement of low energy solar neutrinos will no be possible during that period.

search for...	water phase	pure scintillator	Te-loaded scintillator
$0\nu\beta\beta$ -decay	-	-	✓
⁸ B solar- ν	-	✓	✓
low energy solar- ν	-	✓	-
geo- & reactor- ν	-	✓	✓
supernova- ν	✓	✓	✓
exotic physics	✓	✓	✓

3.2 Search for $0\nu\beta\beta$ -decay in ^{130}Te

Initially the excellent prerequisites of SNO+ for the detection of low energy solar neutrinos favoured this measurement as primary physics goal. However the collaboration decided to prioritise the search for $0\nu\beta\beta$ -decays. A first investigated isotope option was ^{150}Nd due to its relatively large phase space factor and Q -value. A technique to load neodymium into LAB based liquid scintillator was available but limited in terms of achievable mass ($\sim 0.3\%$) and the low natural abundance of 5.64% posed another limitation as isotopic enrichment is extremely costly for this element.

With the invention of a new technique to stably bind metals to organic liquid scintillator (see sec. 4.3), the choice of isotopes widened and ^{130}Te was picked up by the collaboration as it has some significant advantages. Firstly, the Q -value of 2527.518 ± 0.013 keV [Red09] is in a reasonable range and ^{130}Te has the highest natural abundance of 34.08% among the 35 known $2\nu\beta^-\beta^-$ isotopes, allowing for a very large mass to be observed. In a first phase, 0.3% of natural tellurium will be loaded into SNO+ LAB, corresponding to about 800 kg of ^{130}Te . Secondly, the $2\nu\beta\beta$ half-life of $(7.09 \pm 0.9(\text{stat}) \pm 1.1(\text{sys})) \times 10^{20}$ yr [Arn11] is among the longest for the known $0\nu\beta\beta$ isotopes, which leads to a smaller irreducible $2\nu\beta\beta$ background. And finally, the innovative loading technique allows much higher loadings of up to 5% in the further future, while maintaining reasonable optical properties of the tellurium-LAB mixture.

Due to the specific features of the background in the region of interest (ROI), SNO+ will be using an asymmetric definition for the ROI of $-0.5\sigma - 1.5\sigma$ around the expected gaussian signal peak. This helps to preserve most of the $0\nu\beta\beta$ signal, while significantly excluding the irreducible $2\nu\beta\beta$ background as well as ^{238}U - and ^{232}Th chain decays. A 3.5 m fiducial volume cut will reduce the major external backgrounds, leaving about 20% of the signal events. In an energy window of 2.47 MeV to 2.7 MeV, the main backgrounds are, ordered by their contribution from high to low: ^8B solar neutrinos, $2\nu\beta\beta$ decays, external backgrounds such as ^{208}Tl and ^{214}Bi from contaminations in ropes, the AV, PMT glass and water shielding and cosmogenic induced isotopes in tellurium e.g. ^{60}Co or ^{110m}Ag and others. As only one example of background rejection, the dominant uranium- and thorium chain backgrounds can be very efficiently tagged (almost 100% without pile-up) with the delayed ^{212}Bi -Po and ^{214}Bi -Po coincidences, more information on this can be found in section 5.8 as this is also important for this thesis. A comprehensive list with more detailed information, especially about the reduction of the individual backgrounds can be found in [And16]. Figure 3.2.1 shows a simulated signal and background spectrum in the ROI and the mentioned fiducial volume, assuming 5 years running time, 0.3% loading, 99.99% and $> 98\%$ rejection of ^{214}Bi -Po and ^{212}Bi -Po events, respectively. Also a light yield of 200 $N_{\text{hits}}/\text{MeV}$ and for the signal simulation an effective Majorana mass of $m_{\beta\beta} = 200$ meV and the IBM-2 nuclear matrix element are used [Bar13].

With these assumptions, SNO+ can set a lower half-life limit for ^{130}Te $0\nu\beta\beta$ -decay of $T_{1/2}^{0\nu\beta\beta} > 9 \times 10^{25}$ yr (90% C.L.), which corresponds to a limit on the effective Majorana neutrino mass of $m_{\beta\beta} = 55 - 133$ meV, depending on the nuclear matrix element (with a phase space factor $G = 3.69 \times 10^{-14} \text{ yr}^{-1}$ and $g_A = 1.29$) [And16].

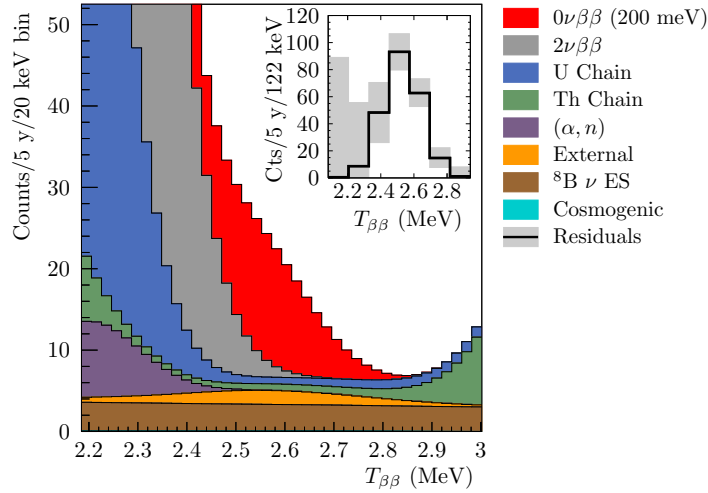


Figure 3.2.1: Simulated signal and background spectrum for a 5 year measurement of tellurium loaded LAB in SNO+. $T_{\beta\beta}$ denotes the effective kinetic energy and a loading of 0.3 % natural tellurium, $m_{\beta\beta} = 200$ meV, fiducial volume of 3.5 m and $200 N_{\text{hits}}/\text{MeV}$ are assumed. Taken from [And16].

3.3 CNO, pep and pp solar neutrinos

Due to the SNOLab site with its excellent shielding against cosmic rays, the SNO+ experiment will be able to measure low energy solar neutrinos with an unprecedented precision, given some conditions. The approximately 6 km.w.e. overburden reduce the cosmic ray muon flux to levels at least two orders of magnitudes lower than at sites for comparable liquid scintillator detectors, such as Borexino and KamLAND. For these pioneering experiments, one major limiting factor is the in-situ ^{11}C production through muon spallation of ^{12}C in the organic liquid. This will not be a major problem for SNO+ and this work evaluates simulations and calculations to support this claim. A detailed analysis and discussion of the relevant muon induced backgrounds will be given in chapter 6. Furthermore SNO+ needs to achieve similar radio-purity levels as the Borexino collaboration in phase-I of their experiment [Arp08; Ali09] to be able to measure pep, CNO, ^8B and pp-solar neutrinos with an excellent sensitivity.

In the last chapter it has been pointed out how precision measurements of the solar neutrino fluxes can effect (standard) solar- and physics models and therefore help to better understand our sun and neutrino oscillations. Especially the shape of the ν_e survival probability in the transition region between matter- and vacuum dominated regime can be investigated by a precise determination of the pep-neutrino flux. For this a precision of at least 10% in the pep neutrino flux is required. For pp neutrinos, Borexino has presented a measurement with about 10% uncertainty [Bel14]. A percent level precision would allow to investigate the solar luminosity constraint, testing extra energy loss or generation mechanisms in the sun [And16].

Concerning backgrounds, the major concern for SNO+ is the level of ^{210}Bi that will be present. During construction and in between the SNO and SNO+ experiments, the AV was exposed to air and radon and radon daughters implanted themselves into the acrylic. The exact levels of bismuth and its leaching into the water and LAB will be studied during the initial water phase and the beginning of the pure scintillator phase. Mitigation strategies such as further purification or the deployment of a balloon are prepared if the levels are too high. For pep and CNO neutrinos the amounts of ^{214}Bi and ^{212}Bi from the ^{238}U and ^{232}Th chain are critical, but can be very effectively suppressed by the already mentioned β - α -coincidence technique (see sec. 5.8). For the measurement of ^8B neutrinos, ^{10}C can pose a background, but due to the short half-life ($T_{1/2} = 19.3\text{ s}$) and supposedly little in-situ production its influence is marginal, see again chapter 6 for more details. Figure 3.3.1 illustrates the complex situation of expected backgrounds and signals.

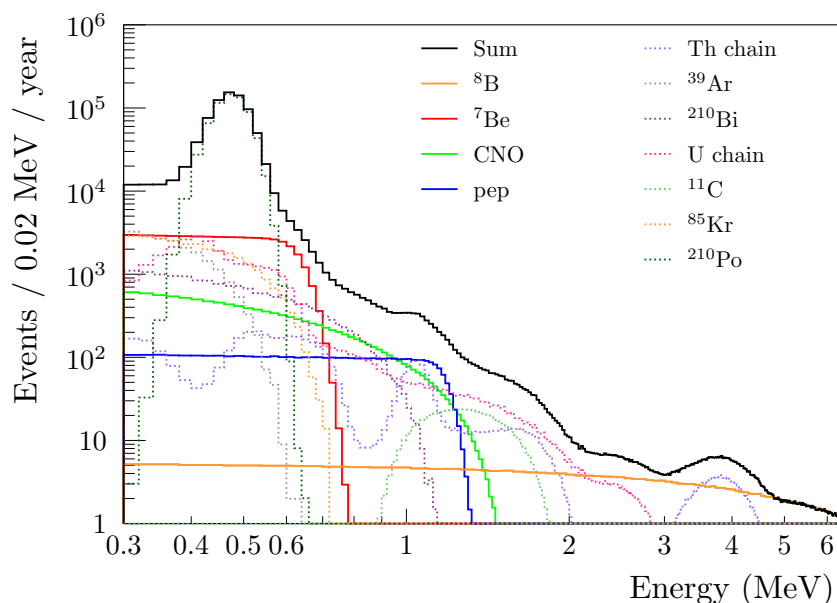


Figure 3.3.1: Expected signals and backgrounds for a SNO+ solar phase in pure LAB-PPO scintillator. Most background levels are those achieved by Borexino phase-I [Arp08; Ali09]. Further assumptions are a light yield of $400 N_{\text{hits}}/\text{MeV}$ and a fiducial volume of 5.5 m. The assumed reduction of ^{214}Bi , ^{214}Po and ^{210}Po isotopes is 95 %, and the input amount of ^{11}C is calculated by a scaling of results from KamLAND and Borexino, see section 6.2. Taken from [And16].

Sensitivities were gained by assuming one year of pure scintillator data, making use of an extended likelihood fit in energy, with a conservative 50 % fiducial volume. This fit included beside the four neutrino signals (^8B , ^7Be , CNO, pep) also thirty background event types and is comprehensively described in [And16]. From these simulations, SNO+ expects to measure the pep flux with less than 10 % uncertainty, the CNO flux with very conservative assumptions to about 15 %, ^7Be neutrinos to 4 % and ^8B with an uncertainty better than 8 %.

The pp neutrino sensitivity depends crucially on the amount of ^{14}C and ^{85}Kr present in the LAB mixture. Therefore SNO+ tries to obtain the liquid scintillator from a source providing LAB especially low in ^{14}C . Should the experiment reach radio-purity levels of 10-50 times that reached by Borexino, within just 6 months of data SNO+ could provide a few percent level uncertainty measurement of the pp flux.

3.4 Reactor-, geo- and supernova neutrinos

In the last chapter it was pointed out how anti-neutrinos emitted from fission products in nuclear power plants or natural radioactivity in the earth's crust and mantle can be detected via the inverse β -decay process $\bar{\nu}_e + p \rightarrow n + e^+$, if the energy of the $\bar{\nu}_e$ is greater than 1.8 MeV. In liquid scintillator the anti-neutrino energy can be measured through the amount of scintillation light that the positron produces as it is slowing down to finally annihilate:

$$E_{\bar{\nu}_e} \simeq E_{\text{prompt}} + (m_n - m_p) - m_e \simeq E_{\text{prompt}} + 0.8 \text{ MeV} \quad (3.1)$$

with m_n , m_p and m_e the mass of a neutron, proton and electron, respectively. Once the neutron in the final state thermalised, it is in 99% of the cases captured by a hydrogen nucleus and subsequently emits the characteristic 2.2 MeV γ -ray. The SNO+ collaboration will thoroughly calibrate the detectors response to neutrons, using the AmBe source that has a well studied n-emission spectrum and was already used by SNO. These results will be used to benchmark the neutron simulation in the SNO+ RAT software.

The main backgrounds for these signals arise from (α, n) reactions, mainly caused by the α -decay of ^{210}Po , which is a well known radon daughter, likely to be present in the AV. Since most of the neutron sources are expected to be external, fiducial volume cuts and reconstruction in the outer regions helps to reduce these backgrounds effectively.

SNO+ expects about 90 reactor- $\bar{\nu}_e$ events per year. The flux from one detector at a distance of 240 km and two at a distance of 350 km shows very clear oscillation patterns (see Fig. 3.4.1), leading to a good sensitivity of Δm_{12}^2 . In a preliminary analysis the following assumptions were made. As the geo- and reactor neutrino signals overlap for energies below 3.5 MeV only signals above this threshold are included. A light yield of 300 $N_{\text{hits}}/\text{MeV}$ is used, which is reduced to this number in the Te-loaded phase. After 7 years of data taking with a 5.5 m fiducial radius, a mass splitting sensitivity of $0.2 \times 10^{-5} \text{eV}^2$ in Δm_{12}^2 can be reached [And16], comparable to that of the KamLAND experiment [Gan11a].

For geo-neutrinos the sensitivity of SNO+ is limited by statistical uncertainties. A comparable rate of geo- and reactor neutrinos is expected in the energy window from 1.8 - 3.5 MeV, but with its larger volume, SNO+ can compensate the higher background due to reactor neutrinos, compared to Borexino. Thus SNO+ will reach a similar sensitivity. In a global analysis, using KamLAND [Gan11b] and Borexino

[Bel13b] data, SNO+ aims to separate uranium and thorium, as well as mantle and crust contributions. A combined illustration of the expected geo- and reactor neutrino energy spectrum in SNO+ is given Figure 3.4.1.

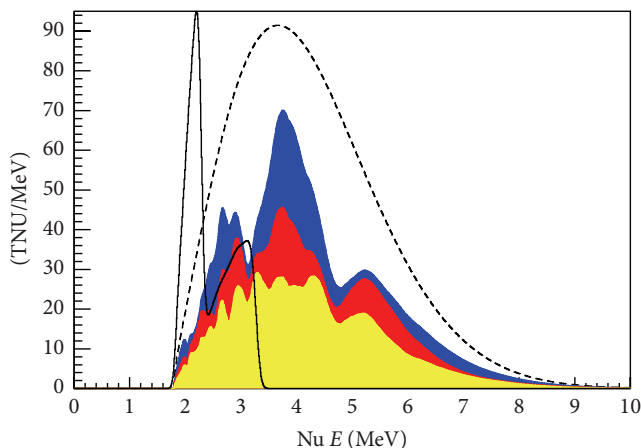


Figure 3.4.1: Expected anti-neutrino spectrum in SNO+, with 10^{32} proton-years per MeV. The dashed line shows the reactor neutrino spectrum in case no oscillation is assumed. Signals from geo-neutrinos are shown with a solid line and arbitrary normalisation. The coloured spectra correspond to the oscillated spectra from individual nuclear power plants: in blue at 240 km and in red at 350 km distance, whereas yellow refers to the sum of others. Taken from [And16].

With its large target mass, low backgrounds and many detection channels, SNO+ will be one of the best supernova neutrino detectors. In the absence of flavour changing mechanisms (others than the well known MSW effect), the shape of the energy spectrum of supernova neutrinos is expected to be thermal. The following sensitivities are gained assuming a supernova in distance of 10 kpc from the sun and that 10^{53} erg of binding energy is released in form of the three neutrino and three anti-neutrino types, which are assumed to be released in equal amounts. Derived from the observation of SN 1987 A, mean energies for ν_e and $\bar{\nu}_e$ of 12 MeV and 15 MeV are used respectively, as well as 18 MeV for the other types.

The possible detection channels and event numbers in SNO+ are summarised in Tab. 3.4.1. The elastic neutrino scattering at protons is of special interest as it is the only (significant) reaction that provides information about the $\nu_\mu, \nu_\tau, \bar{\nu}_\mu, \bar{\nu}_\tau$ spectral shape. Even though its cross-section is three time smaller than that for inverse beta decay, it is possible for all six neutrino types, and thus the final event rates are similar, see Tab. 3.4.1. In order to extract the neutrino energy correctly, the strongly non-linear quenched light yield of protons in all relevant LAB mixtures were measured by Krosigk et al. [Kro13]. In simulations, the reconstructed neutrino energy spectra from ν -p elastic scattering are in excellent agreement with the theoretical input [And16].

Finally it shall be mentioned that the SNO+ collaboration will also search for more exotic physics signals from invisible nucleon decay and axion-like particles, which are not further discussed here. For more information, refer to [And16].

Table 3.4.1: Detection channels and expected number of events for supernova neutrinos in 780 t of LAB-PPO. The assumed incoming flux is described in the text and no flavour changing mechanisms are considered. CC and NC refer to charged- and neutral current reactions, respectively. The uncertainties only stem from those of the cross-sections. Data taken from [And16].

reaction	Number of events
NC: $\nu + p \rightarrow \nu + p$	119 ± 3
CC: $\bar{\nu}_e + p \rightarrow n + e^+$	195 ± 1
CC: $\bar{\nu}_e + {}^{12}\text{C} \rightarrow {}^{12}\text{B}_{g.s.} + e^+$	7 ± 7
CC: $\nu_e + {}^{12}\text{C} \rightarrow {}^{12}\text{N}_{g.s.} + e^-$	2.7 ± 0.3
NC: $\nu + {}^{12}\text{C} \rightarrow {}^{12}\text{C}^* + \nu'$	44 ± 9
CC/NC: $\nu + {}^{12}\text{C} \rightarrow {}^{11}\text{C}/{}^{11}\text{B} + X$	2.4 ± 0.5
ES: $\nu + e^- \rightarrow \nu + e^-$	13

CHAPTER **4**

Organic liquid scintillator

THIS chapter shall introduce the phenomenon of scintillation in organic liquids in a general way, and in more detail some processes that are of special interest for this work. Besides the processes of quenching, namely non-radiative de-excitation, also the current knowledge of temperature effects is discussed. As linear alkyl benzene is the choice of SNO+ as basic solvent, its properties will be discussed and thus why it was chosen.

The word scintillation stems from the Latin *scintillare*, which means sparkling or jitter. It refers to all phenomena where light is emitted by a substance that was excited by some kind of radiation. It occurs in a wide range of liquid, solid state, gaseous, organic and inorganic materials and is of interest for many practical purposes. As the emitted light is usually in the visible or UV range, a detection of this light and the subsequent transformation into a well quantifiable electric signal is extremely useful. Not only do nuclear and particle physics experiments make frequent use of this, but also every day applications profit from this behaviour. For example, only the very fast light generation and detection make medical imaging techniques such as positron emission tomography (PET) possible. Other examples are the scintillation of fluorine in toothpaste or washing agents as well as the afterglow of the hands in a classic wrist watch or emergency signs.

As the scintillation mechanism is fundamentally different in inorganic materials, such as NaI, CsI, CdWO₄, Ar or Xe, the following description concentrates on organic substances, since they are the main interest of this work.

4.1 Physics of scintillation in organic liquids

Carbon's important role in organic chemistry makes its electron structure and states a very important part in understanding the scintillation process. The configuration of electrons in a state that is able to form bonds is $1s^2 2s 2p^3$, where one $2s$ electron is already excited into a $2p$ state, from the original carbon ground state of $1s^2 2s^2 2p^2$. In the very common combination with hydrogen, carbon forms double and triple-bonds with the H atom. Those four valence electron orbitals can form molecular bonds by hybridisation into so called sp^3 , sp^2 and sp hybrid orbitals. This can theoretically be described by solving Schrödinger's equation for a slightly excited carbon atom which can be done by linear combination of atomic orbitals (LCAO).

The sp^3 configuration is of tetrahedral shape, is present i.e. in diamond or methane, and not scintillating. In the sp hybridisation the spatial arrangement is linear, two p orbitals are unchanged and one is mixing with the s state to form a so-called σ -bonding. These are themselves not scintillating either, though they might occur in molecules such as acetylene, which are luminescent due to the presence of another electron binding via sp^2 orbitals.

In sp^2 hybridisation one p -orbital is unchanged, whereas the other two p and one s are mixing. These form a plane that is orthogonal to the remaining p -state. This arrangement is the basis for the formation of the hexagonal ring structure of benzene (C₆H₆). Figure 4.1.1 illustrates how the aforementioned σ -bonds build the ring of carbon atoms with hydrogen atoms attached, and how the remaining p -orbitals form

a symmetric nodal plane. While the σ -electrons are well localised and difficult to excite, the so-called π -electrons from the six p -orbitals interact with each other, are only loosely bound and therefore called de-localised.

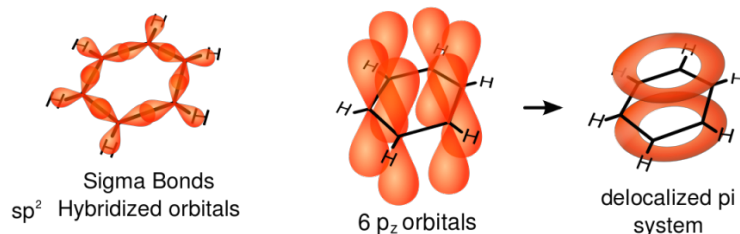


Figure 4.1.1: Three illustrations of electron orbital structures of a benzene (C_6H_6) molecule. On the left, σ -bonds of sp^2 hybrid-orbitals form the hexagonal benzene ring. The remaining p atomic orbital from the six carbon atoms form a nodal plane (middle). The resulting π -molecular orbitals are depicted as red rings on the right. Taken from [Wik16].

Those π -electrons can be easily excited and already a simplistic semi-classical model is able to describe the basic features of the excitations. This perimeter free-electron model was developed by Platt [Pla49] already in 1949. It is the basis for a more complete calculation of the electron energy states as they are illustrated in Fig. 4.1.2. Here, also the spin orientation of an excited electron relative to the unpaired electron in the ground state needs to be taken into account. For anti-parallel aligned electron spins, so-called singlet states are generated that lie above the ground state S_0 and are labelled $S_{1,2,\dots}$. The excited states with parallel electron spin orientation are called triplet states, labelled $T_{1,2,\dots}$ and are always energetically lower than the corresponding singlet state (Hunds rule [Hun27]). Furthermore is each level degenerated by vibrational sub-levels that add another subscript to the labels, e.g. $S_{10,11,12,\dots}$ for the first excited singlet sub-levels. While the vibrational excitations lie ~ 0.1 eV apart, the major energy levels distance are around 1 – 4 eV. The upper end of the scheme is marked by the π -electron ionisation energy I_π .

Once a molecule is excited into a singlet state or its vibrational sub-level, internal conversion (also degradation) is taking place on very small time scales of $\sim 10^{-12}$ s, i.e. non-radiative relaxation into vibrational sub-levels of the first excited state S_{1j} , via collision with neighbouring molecules. A subsequent vibrational relaxation into S_{10} happens just as fast and marks another non-radiative transition via heat dissipation.

As a direct population of triplet states from S_{0j} via absorption is forbidden due to the necessary spin-flip, only two indirect transitions are possible. Firstly a so-called intersystem crossing can occur were S_{10} (that always lies above) relaxes via electron spin-flip into T_{10} , again radiationless. And secondly, if an ionised molecule recombines with an electron, 75 % of them 'fall' into triplet states, due to spin multiplicity selection rules.

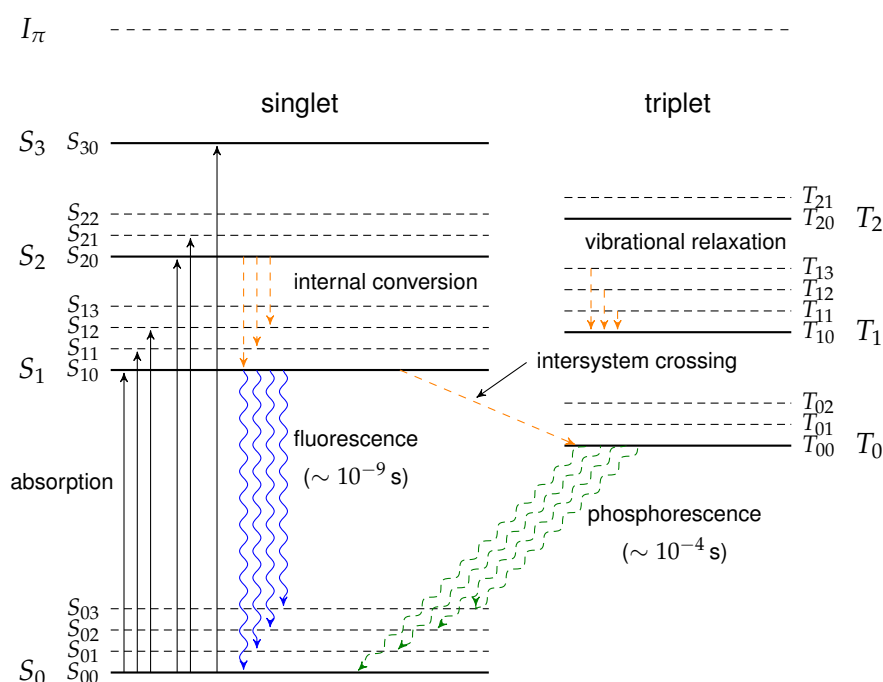


Figure 4.1.2: Energy levels of π -orbitals in organic molecules, also known as Jablonski diagram. Emitted radiation is marked as wavy blue line (fluorescence) and dashed wavy green line (phosphorescence). Non-radiative transitions are drawn with orange dashed lines.

The three possible processes of de-excitation from S_1 and T_1 into the ground state are:

fluorescence that describes the 'normal' transition from S_{10} into the ground states S_{0j} , via the emission of photons. As the population of S_{10} decays exponentially, the intensity of the emitted light can be described by:

$$I(t) = (-I_0 e^{-t/\tau_{rise}})(I_0 e^{-t/\tau_{decay}}) \quad (4.1)$$

where τ_{rise} is a measure for the steep rise-time of the light intensity, and τ_{decay} a measure for the lifetime of the state and in the order of $\tau_{fluorescence} \sim 10^{-9}$ s. The probability of reaching first a vibrational sub-levels of S_{0j} is higher, thus the emitted light is of less energy and therefore longer wavelength than what would be needed for an absorption like $S_{00} \rightarrow S_{1j}$. This is called Stokes shift and this type of scintillator is therefore mostly transparent for its own light.

phosphorescence which is the forbidden transition from T_0 to S_{0j} as it involves an electron spin-flip. Therefore this de-excitation is strongly suppressed which translates into longer decay times of up to $\tau_{phosphorescence} \sim 10^{-4}$ s or even longer, depending a lot on the actual molecular structure. In order to incorporate this into Eq. 4.1, usually simply another exponential decay term is added to the equation.

delayed fluorescence is a name for several processes that occur on time scales similar to phosphorescence, do not follow an exponential behaviour and usually contribute to the total light output only in a minor way. One component arises from transition of a T_{10} or another metastable state back to S_{10} , e.g. by collisions with other molecules or if the molecule itself has enough thermal energy to overcome the gap between T_{10} and S_{1j} . In this case the following transition from S_{10} to S_{0j} is the same as in the case of normal fluorescence. As the energy gap is large for aromatic hydrocarbons, another effect is more important here, so-called excimer formation. Excimers (excited dimers) are formed by colliding molecules where at least one is excited into a triplet state. Those might dissociate thermally into excited singlet monomers and subsequently de-excite via $S_{10} \rightarrow S_{0j}$ fluorescence [Par63; Bir64].

One practical aspect of the combination of these three processes is depicted in the scheme in Fig. 4.1.3, as it is showing how a scintillation light pulse is composed of mainly two components. The fast component arises from direct fluorescence and the slow component is a mixture of phosphorescence and delayed fluorescence. Since the recombination of ionised molecules in triplet states is strongly enhanced, the ratio of the fast and slow decay component is largely influenced by the ionisation strength of the incident radiation.

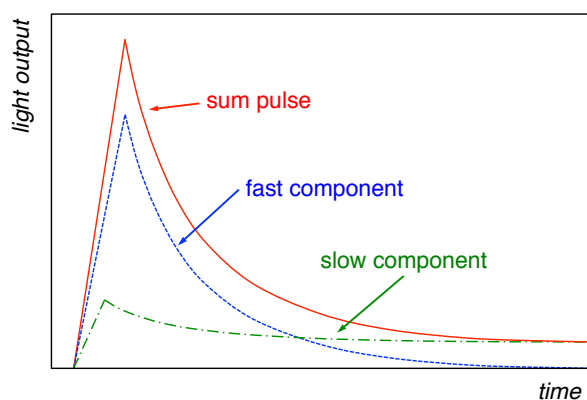


Figure 4.1.3: Scheme of scintillation light output vs. time, with fast and slow component of the total light output.

In order to develop a comprehensive view on the processes taking place in organic (liquid) scintillators, it is inevitable to consider not only pure scintillators, such as anthracene, LAB, or polystyrene. Also system with secondary fluors (binary systems) and even such with a third fluor, so called ternary systems are very important and actually widely used. These compound scintillators prove to be beneficial mainly for the following two reasons.

Firstly, even though all scintillators show a Stokes shift and are therefore to some extent transparent for their own light, an overlap of the emission and absorption spectra is common. This self-absorption effect can reduce the overall efficiency significantly. By adding another, compatible fluor to the mixture, this loss of light can be mitigated. Ideally these secondary scintillators absorb the radiation from the main solute very effectively and re-emit light at longer wavelengths. For that reason they are also called wavelength-shifters. Common liquid solvents and primary scintillat-

ors are 1,2,4-trimethylbenzene (PC), also known as pseudocumene, and LAB. These might be combined with 2,2-p-phenylene-bis-(5-phenyloxazole) (POPOP) and PPO as primary solutes.

And secondly, shifting the final emitted wavelength might have other positive effects, such as to better match photomultiplier tube (PMT) sensitivities, reflectivity or transparency of other relevant detector material. This is mostly done by secondary solutes, such as 1,4-bis(2-methylstyryl)benzol (bis-MSB).

In such a liquid scintillator system consisting of a solvent and two fluors various processes are taking place. The following section shall give an overview and will especially focus on energy transfer between the three constituents. In the standard literature e.g. by Birks [Bir64] and Bransome et al. [Bra70], a more or less common notation and depiction has been developed and will be followed here as well. Figure 4.1.4 is adapted from [Bir64] and illustrates diagrammatically radiative and non-radiative transitions and energy transfer processes in ternary liquid scintillator systems.

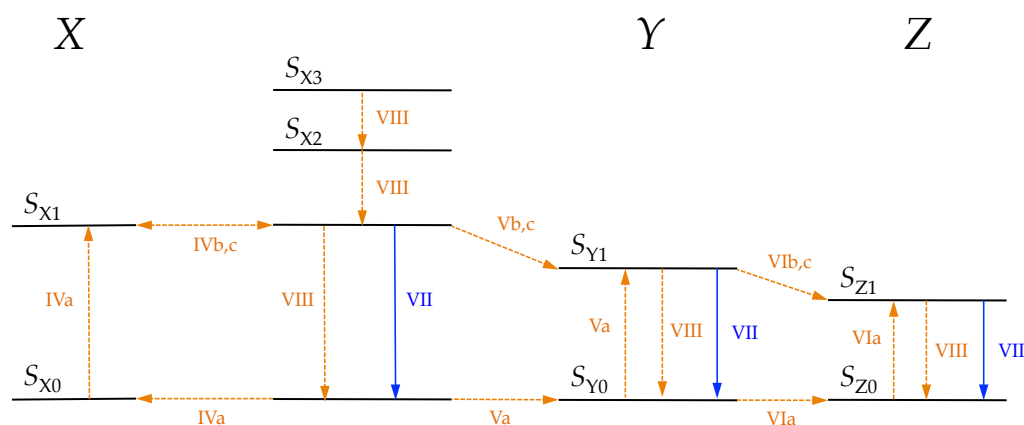


Figure 4.1.4: Scheme of energy transfer processes between π -electron singlet states (solid black lines) in ternary organic scintillator compounds. Solid blue lines indicate fluorescence and dashed orange arrows various transition and transfers as they are described in the text.

Due to the typically very low concentrations of the solutes, the primary excitation processes are almost only taking place on the solvent molecules, here X, e.g. LAB. Primary and secondary solutes are abbreviated with Y and Z, respectively. Excited states are labelled with the corresponding number of stars, ions with the common plus and minus, and spin multiplicity with a prefix-superscript. Occurring only ones are dimers (*D*) and free radicals (*F*). The following list separates primary and secondary processes and corresponds to the scheme in Fig. 4.1.4.

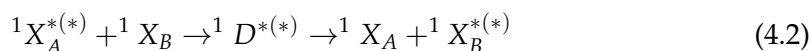
primary processes (via energy deposition by radiation)

- I) excitation of π -electrons, absorption, producing
 - a) $^1X^{*(*)}$
 - b) $^3X^{*(*)}$
- II) excitation of σ - or carbon 1s- electrons, producing
 - a) $\sigma^{*(*)}$
 - b) $1s^{*(*)}$
- III) ionisation, producing
 - a) $^2X^+ + e^-$
 - b) $F^+ + F^-$ (free radicals)

secondary processes

- IV) transfer between X's by
 - a) absorption and re-emission
 - b) collisions
 - c) dipole-dipole coupling
- V) transfer from X to Y
 - a) absorption and re-emission
 - b) collisions
 - c) dipole-dipole coupling
- VI) transfer from X to Y to Z
 - a) absorption and re-emission
 - b) collisions
 - c) dipole-dipole coupling
- VII) fluorescence
- VIII) internal conversion
- IX) intersystem crossing
- X) excimer fluorescence
- XI) $D^{*(*)}$ dissociation into $^3X^{*(*)}$ and 1X
- XII) excimer dissociation into $^1X + ^1X$
- XIII) phosphorescence

The energy transfer processes are caused mainly by three physics phenomena. As the densities in liquid scintillators are $\sim 10^3$ mol/m³, direct intermolecular reactions taking place, i.e. excited molecules $^1X^{*(*)}$ collide with unexcited ones and may form excimers $^1D^{*(*)}$ (IVb, Vb, VIb), after which they could dissociate, e.g.:



This is taking place on time scales on the order of $\mathcal{O}(10^{-11}$ s) and competes with $D^{*(*)}$ dissociation into a triplet state (XI), non-radiative via thermal dissipation (XII) or excimer fluorescence (X).

Besides the already described absorption and re-emission (IVa, Va, VIa), dipole-dipole coupling contributes significantly to the energy transfer, originally developed by Förster [För48; För51]. The transfer rate constant is given by:

$$k_{ET} = \frac{1}{\tau} \left(\frac{R_0}{R} \right)^6 \quad (4.3)$$

where R is the distance between the molecules, τ the lifetime of the excited molecular state and R_0 the critical radius at which energy transfer is 50 % likely to occur. Typical values for R_0 are on the order of $\mathcal{O}(10 \text{ nm})$, which is the reason why Förster energy transfer is also called long-range coupling.

Furthermore Dexter found that even direct electron transfer reactions might occur non-radiatively between molecules [Dex53]. Here, the wave functions of the molecules must overlap, which leads to an exponential decrease with distance, and hence the rate constant is:

$$k_{ET} \propto J e^{-2R/L} \quad (4.4)$$

with R again the distance of the molecules, J the spectral overlap integral and L the sum of the Van der Waals radii. This direct electron migration occurs only on very short distances of less than 10 \AA and therefore contributes only to a minor degree to the energy transfer processes.

Formerly it has been disputed whether excimer formation and dissociation or dipole-dipole coupling might be the dominant process in excitation migration [Bir64; Con68; Hom85b]. A study by Mathad and Umakantha [Mat85] sheds light into this subject. They investigated a liquid scintillator mixture composed of a solvent of 90 % cyclohexane and 10 % toluene, which was mixed with 3-phenylindole-1-propionitrile as single solute. With more or less simple models of the temperature dependence of the energy transfer processes, they could demonstrate, with temperature variation measurements, **that resonance interaction accounts for about 99 % of the energy migration**. These measurements are simultaneously interesting in the scope of this work and will therefore also be discussed in detail in section 4.4 of this chapter. Before that, the next section will focus on non-radiative processes of liquid scintillator de-excitation.

4.2 Quenching

After gaining an understanding of the basic principles of the luminescence of aromatic hydrocarbons in the last section, this part shall now focus on non-radiative de-excitations or transitions that do not result in a direct light generation. These effects are generally known as quenching. While a vast variety of effects can lead to reduced light output in organic liquids, the following selection concentrates on common mechanisms and those which are most important in the scope of this work.

The very common **colour or impurity quenching** refers to absorption of scintillation light by impurities and contaminations. As they will typically reduce the light intensity at a certain wavelength, this 'colour' would be missing or strongly suppressed in the resulting emission spectrum. In case the foreign molecules are

not luminescent themselves, this change in spectral intensity would remain the only effect. Otherwise the overall reduction in light output might be less pronounced, though an additional scintillation component obviously also changes the timing of the produced light.

Simultaneously all foreign molecules might also take part in non-radiative energy transfers. Especially if they are not luminescent, the energy transferred to them is then lost in terms of light generation. This effect is called dynamic impurity quenching, whereas static impurity quenching refers to another phenomenon. Here the contaminations form ground state complexes with the scintillator components. Even though they might be excited, they are usually not fluorescent and therefore inactive and also lost for light generation.

A very important example for a substance that causes strong dynamic impurity quenching is oxygen, which also demonstrates how the presence of a contamination can lead to an reduction in light yield via various effects. **Oxygen quenching** is well studied and known already for a long time [Bow39]. Dioxide (O_2) naturally dissolves in liquid scintillator if no special provisions are made to eliminate oxygen from the atmosphere in which the solution is prepared or handled. The molecule causes not only the already mentioned impurity quenching but also has a very rare triplet ground state which leads to another non-radiative transition competing with fluorescence. The first excited triplet state of O_2 has an energy of 0.98 eV and lies therefore mostly below the excited triplet state of the organic scintillator molecule, which leads to a direct transition that is actually preferred over the triplet - triplet interaction between the hydrocarbons. Using the symbolism from the last section, the reaction can be described with:



Like this, the excitation energy migrates to the dioxide, leaving the aromatic hydrocarbon molecule in the singlet ground state and the oxygen in an excited singlet state, thus eliminating any fluorescence or phosphorescence of the scintillator. Through this mechanism, liquid scintillators with dissolved oxygen show a significantly reduced slow scintillation component. It has been shown that this even leads to problems in pulse shape discrimination, e.g. in LAB based scintillators [OKe11]. Furthermore does O_2 catch electrons well, reducing free electrons from ionisation processes which in turn would normally provoke scintillation. One last argument against oxygen is that its excited singlet state molecules are chemically reactive and deteriorate the scintillator.

Since the presence of oxygen in the solutions has these severe effects, great care has to be taken to removing it thoroughly and avoiding it dissolving into the liquids. The common ways to do so are vacuum distillation, ultrasonic degassing or using noble gasses for bubbling, such as nitrogen or argon [Bow39; Pri53]. The nitrogen flushing method is widely used due to its effectiveness, simplicity and the common availability of N. Even average quality N or Ar can be considered practically oxygen free, so that, when bubbling, the O_2 diffuses into the bubbles and is removed from the liquid. A dedicated study has shown that the optimal bubble diameter is ≈ 4 mm and

that after a flushing time of about 20 min the lowest remaining oxygen concentration is reached [Xia10].

The last mechanism that shall be discussed here is the very important **ionisation quenching**. In the last section it was pointed out that electrons recombining with ionised scintillator molecules preferably occupy triplet states. That causes a reduced overall light output since the quantum yield of phosphorescence is much smaller than for fluorescence. This effect influences heavily the composition of prompt and slow scintillation light, thus the timing profile depends strongly on the ionisation energy loss of the incident particle. This is the main reason why the luminescence of α -particles is quenched strongly. The influence of ionisation quenching on the light timing profile is depicted in Fig. 4.2.1, clearly showing how the late light component is significantly more pronounced in the case of α -radiation.

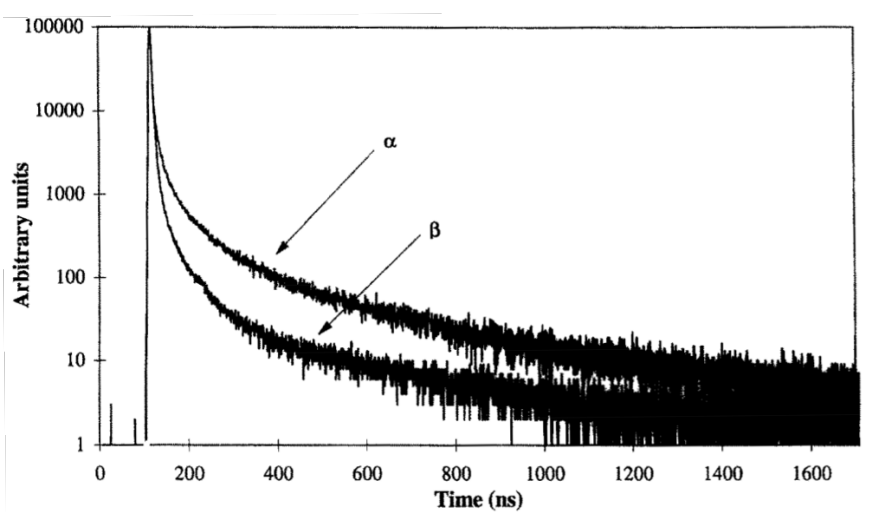


Figure 4.2.1: Scintillation light timing profile for α -particles (^{210}Po) and electrons (via ^{137}Cs) in PC + 1.5 g/l PPO. Normalised to peak height. Taken from [Eli97].

As this phenomenon is due to the primary interaction of the incident particle with the solvent, it is independent of solutes [Kro13]. A quantitative description of ionisation quenching was developed by Birks in the middle of the last century [Bir51], firstly by studying anthracene. A good starting point is the linear approximation of the light output, simply assuming an efficiency constant, e.g. S , as link between the in the scintillator deposited energy E and light yield L :

$$L = SE \quad (4.6)$$

which is true only if interactions between excited or ionised molecules are neglected. Considering a differential path length dx of a particle in the compound, Eq. 4.6 becomes:

$$\frac{dL}{dx} = S \frac{dE}{dx} \quad (4.7)$$

This linearity approximation works well for fast electrons with a relatively low ionisation density along their path, so that the respective molecules lie far enough

apart. For many scintillator types this has been confirmed for electron energies above ≈ 100 keV [Abe11; Bra62]. For slow electrons or heavy particles such as protons, helium nuclei or other ions, dE/dx is larger and thus the density of excited and ionised molecules is high enough for interactions between them. This results in a non-linear behaviour, which was semi-empirically described by Birks with:

$$\frac{dL}{dx} = S \frac{\frac{dE}{dx}}{1 + kB \frac{dE}{dx}} \quad (4.8)$$

here k is a parameter to account for ionisation quenching, B is a constant in the product $B dE/dx$ which is known as specific ionisation density. Since kB commonly occur together, this product is known as Birks's constant and Equation 4.8 as Birks's law. For particles with a large dE/dx , Eq. 4.8 becomes

$$\frac{dL}{dx} = \frac{S}{kB} = \text{const.} \quad (4.9)$$

A good comparison of the specific fluorescence (dL/dx) versus energy loss in the case of an anthracene crystal is given in Figure 4.2.2. The deviation from the linear trend for higher dE/dx is compelling and Birks's law (function (a) in Fig. 4.2.2) approximates most of the data very well.

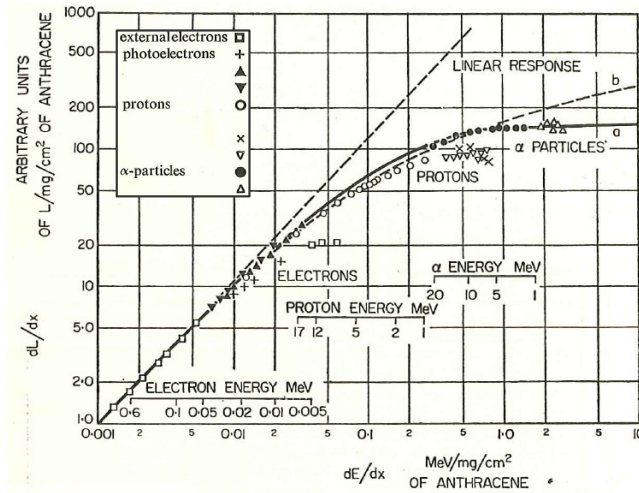


Figure 4.2.2: Specific fluorescence of an anthracene crystal, irradiated with protons and α -particles. Also the respective values for photo-electrons and internal electrons are shown. The theoretical curve (a) is calculated with Eq. 4.8 and $kB = 0.0053$ cm/MeV and $S = 1040$ MeV $^{-1}$. The curve (b) uses a bi-molecular theory not further discussed here. External electrons show a deviation towards lower light yield due to surface effects.

For practical considerations the actual light yield is mainly of interest, which is represented in the integral form of Birks's law:

$$L(E) = \int_0^E \frac{dE}{1 + kB \left(\frac{dE}{dx}\right)} \quad (4.10)$$

Even though this only assumes uni-molecular interactions and is overall a very simplistic, semi-empirical model, Eq. 4.10 succeeds extremely well in describing the light yield in solid and liquid organic scintillators. Initially the Birks parameter kB was considered universal for all particle types different from electrons. If so, it would suffice to measure kB for one particle type (e.g. α 's from internal contaminations) and

calculate the respective light yield for all other kinds. While this has been confirmed by Tretyak [Tre10], recent investigations by Krosigk et al. [Kro13; Kro16] indicate that α -particles might actually have different Birks parameters than protons.

Finally it shall be mentioned that for practical measurements, usually a relative determination of the light yield is preferred. Commonly electrons are used as reference and the light yield $L(E)$ will be given in units of electron equivalent energy. The so-called quenching function of an ion is thus given by its light yield ratio to electron light output:

$$Q_i(E) = \frac{L_i(E)}{L_e(E)} \quad (4.11)$$

which is, for a given energy, known as quenching factor.

4.3 Linear alkyl benzene and SNO+

Now the focus shall be laid on linear alkyl benzene (LAB), which will be the basis for the liquid scintillator solution of the SNO+ experiment. Therefore all measurements within this thesis have been carried out with LAB mixtures that are close to what will be used by the SNO+ collaboration. As the final composition has not been decided yet, this work used the same basic ingredients and the solutions were slightly optimised for the detector setup described in chapter 5.

The name LAB describes not a single molecule but rather a family of those and therefore mostly mixtures of slightly different compositions that differ due to the exact production process. The LAB that will be used for SNO+ and was used for all measurements during the work for this thesis is composed of the hydrocarbons shown in Table 4.3.1. The given values are approximate and the resulting average composition formula reads $C_{17.1}H_{28.3}$.

Table 4.3.1: Approximate molecular composition of the linear alkyl benzene that will be used by the SNO+ experiment. Taken from [Mas07].

molecule	mass fraction [%]
$C_{17}H_{28}$	43.2
$C_{18}H_{30}$	33.4
$C_{16}H_{26}$	20.4
$C_{19}H_{32}$	1.8
$C_{15}H_{24}$	1.2

Even though benzene and alkyl benzene was known and used as solvent for liquid mixtures already in the early decades of scintillator physics, it has caught more attention in recent years. This is due to some properties that make it superior to other solvents such as PC, toluene and cyclohexane. Starting with practical considerations, LAB is an odourless, colourless liquid with a relatively high flash point of $130^\circ C$, that is low in toxicity and environmentally safe. It is readily available and rather cheap, as it is a component of standard detergent production process in chemical

industry. Furthermore it can be bought in high purity and is chemically compatible with acrylic, which makes it suitable for the SNO+ detector.

From the physics point of view, already pure LAB exhibits good light yield with about 60% compared to anthracene [Kög11]. When combined with e.g. 2 g/l PPO, it reaches comparable levels in total light yield with about 10 000 photons/MeV deposited energy. This amount of primary solute will also very likely be used in the SNO+ scintillator and eventually combined with a second fluor, possibly bis-MSB or perylene, both with about 15 mg/l. These values have been determined experimentally to reduce an overlap between absorption and emission and therefore increased light yield. A recent and comprehensive study on this topic is presented by Ye et al. [Ye15]. The effect of the solutes on the total light yield and the emission spectra is nicely depicted in Figure 4.3.1, obtained by transmission and UV excitation measurements. When taking a closer look at the overlap between emission and absorption, the effect of primary and secondary solute is strongly visible and it is very clear that this results in enhanced light yield. Furthermore, the spectral sensitivity of the PMTs is much better matched for emission maxima at larger wavelengths, i.e. above 350 nm.

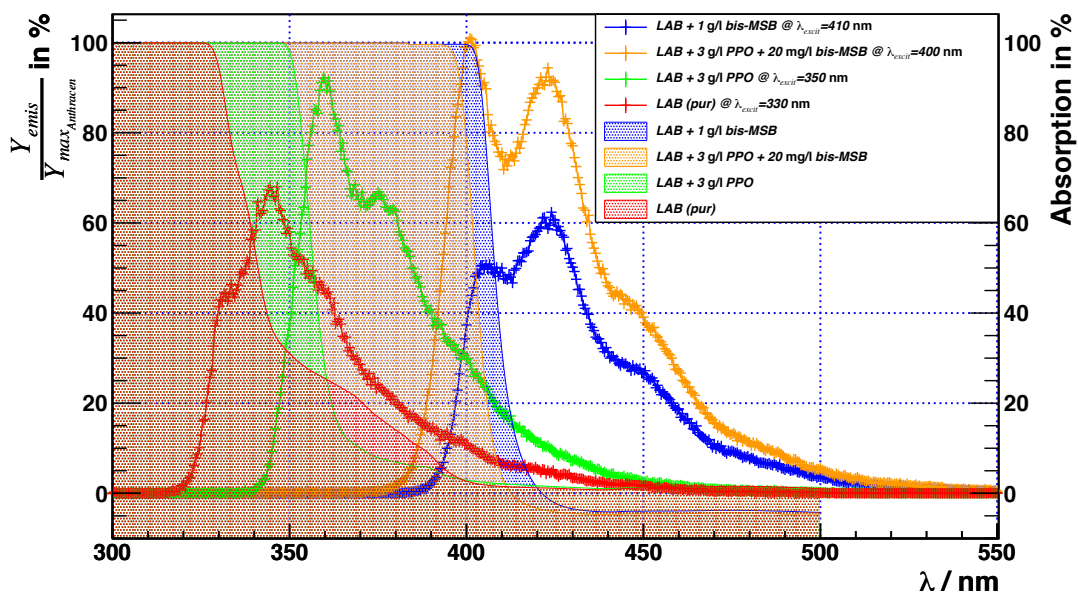


Figure 4.3.1: Emission (solid lines, shaded area) and absorption (crosses) spectra for several LAB mixtures. In terms of light yield, the yellowish solution with LAB + 3 g/l PPO and 20 mg/l bis-MSB seems to be the most promising. In SNO+ the green LAB-PPO spectra will look different, as this was taken with a small 1 cm thick cuvette, which is not large enough to show another peak at around 340 nm. Taken from [Kög11].

In addition to dissolving secondary fluors in LAB, it is sometimes desired to bind inorganic substances to the organic scintillator molecules, in order to establish a stable solution. These metal-organic compounds are sometimes very difficult to achieve and even more challenging in terms of high radio-purity and constraints on the scin-

tillation properties of the liquid. A first example can be found in the initial goal of SNO+ to investigate the double beta decay of ^{150}Nd . A way to bind neodymium to LAB is via a so-called single stage solvent-solvent extraction process. Here neodymium chloride hexahydrate ($\text{NdCl}_3\cdot 6\text{H}_2\text{O}$) and the reactant 3,5,5-trimethyl-hexanoic acid (TMHA) are combined in an aqueous solution, forming a organic Nd complex which can then be extracted into LAB. The product, metal-loaded LAB contains up to 1% neodymium and is in a stable solution for several years [Yeh07]. As the metal loading affects the optical properties of the LAB dramatically, SNO+ had planned to use only 0.1% Nd fraction. Because samarium is a lanthanide as well and thus has similar chemical properties, this technique can also be used to generate Sm loaded LAB, which was used in this thesis and will be presented in the next chapter.

A second example is the current goal of SNO+ of loading LAB with tellurium in order to search for the neutrinoless double β -decay of ^{130}Te . The situation with tellurium proved to be at least as difficult as with neodymium, but at Brookhaven National Laboratory (BNL) a novel process was developed using a water-surfactant binding technique. Here the hydrophilic tellurium in form of telluric acid ($\text{Te}(\text{OH})_6$) is dissolved in water and a link with the hydrophobic LAB is formed by using an aromatic photoreactive surfactant (PRS). This leads to a final scintillator mixture containing not only the solvent, solutes and isotope of interest, but also fractions of water and surfactant. For an initial loading of 0.3% Te in LAB, $\sim 2\%$ water and $\sim 5\%$ PRS would have to remain in a stable liquid scintillator mixture. While water of extremely high purity is readily available, the radio-purity of the surfactant remains one of the major last challenges for the SNO+ scintillator. Therefore the very final mixture of tellurium loaded LAB for SNO+ has not been decided yet. Table 4.3.2 gives an overview of the relevant components used in either this thesis or those that will be used by SNO+, as far as known to date.

Table 4.3.2: List of relevant components of LAB mixtures used for this thesis or in SNO+. As PRS describes a family of compounds and as the final composition for SNO+ has not been decided yet, it is not included here. The data is taken from [Mas07; Pet09; She15; Kro15]

description	name	molecular formula	density [g/cm^3]
solvent	LAB	$\text{C}_{17.1}\text{H}_{28.3}$	0.86
1 st solute	PPO	$\text{C}_{15}\text{H}_{11}\text{NO}$	1.06
2 nd solute	bis-MSB	$\text{C}_{24}\text{H}_{22}$	1.10
2 nd solute	perylene	$\text{C}_{20}\text{H}_{12}$	1.30
-	TMHA	$\text{C}_9\text{H}_{18}\text{O}_2$	0.9
sample isotope	neodymium	Nd	7.01
sample isotope	tellurium acid	$\text{H}_6\text{O}_6\text{Te}$	3.07
sample isotope	samarium	Sm	7.54

4.4 Temperature effects

This last section in this chapter shall introduce and discuss the available literature on the subject of temperature effects in organic liquid scintillators.

The change in density is the most obvious to start with. Since the purpose of this work is to investigate the behaviour of LAB based liquid scintillators, it will be constraint to this particular solvent. A dedicated density versus temperature measurement has been undertaken by O’Keeffe [OKe09]. This ensures that the density is known precisely at whatever temperature will be present during the experiment, with exactly the Petresa LAB that will be actually used in SNO+. O’Keeffe used a hydrometer and found the parameters for the function:

$$\rho(T) = \rho_0 - n \times T \quad (4.12)$$

to be $\rho_0 = (0.86 \pm 0.01) \text{ g/cm}^3$, $n = (5.88 \times 10^{-4} \pm 8.8 \times 10^{-5}) (\text{ }^\circ\text{C})^{-1}$ and T in $[\text{ }^\circ\text{C}]$. For the scope of the investigations in this work, the concerning temperature range is -5°C to 30°C , which then results in density changes of about 1.95 % and -0.63% compared to room-temperature (24.5°C), respectively.

When researching for temperature effects in liquid scintillators, real data and good studies are scarce, especially when focusing on changes in light yield. The very first investigations were carried out by Seliger and Ziegler [Sel56]. Unfortunately they changed the temperature of their whole measurement setup, including the PMTs. Therefore their work was discussed and commonly disqualified by Laustriat and Coche [Lau58; Lau60] and Birks [Bir64].

The former two did investigate temperature effects themselves with three different toluene solutions. They used PPO, 2-phenyl-5-biphenyl-oxadiazole (PBD) and 2-phenyl-5- α -naphthylloxazole (α -NPO) as single solute. While somehow maintaining the PMTs at constant temperature and exciting the mixture via UV light, they report negative temperature coefficients for PPO of about 20 % increase in light output and about 10 % for PBD, both at -10°C . When they used ^{137}Cs as a radiation source, the effect is much less expressed with less than 5 % for both solvents, again at -10°C . This study is difficult to interpret quantitatively since they did not describe or show their setup, they did not explain how they achieved temperature stability on the PMTs or how this was controlled and they did not report any uncertainties on their measurements. Therefore, unfortunately, this can only be seen as an indication that scintillation light output might be quenched at higher temperatures and is enhanced when the liquid is cooled down.

More than two decades later Homma, Murase and Sonehara [Hom85b; Hom85a; Hom87] revisited this topic and carried out some measurements with α - and β -radiation sources dissolved in five different liquid scintillator solvents, namely o-xylene, m-xylene, ethyl-benzene, benzene and cumene. The single fluor solute in all of them was 4 g/l PPO. The radiation sources were ^{241}Am with $E_\alpha = 5.49 \text{ MeV}$ and $E_\alpha = 5.44 \text{ MeV}$, and $^{131\text{m}}\text{Xe}$ which emits mono-energetic electrons of $E_\beta = 0.164 \text{ MeV}$. Even though they show pulse-height spectra (see Fig. 4.4.1), again they did not analyse their data quantitatively, do not give any uncertainties and describe their setup

only roughly. They also claim to have stabilised the PMT temperature for all measurements. Figure 4.4.1 shall give an impression how difficult it is to extract any quantitative information from this study, in order to compare it with this work. When using the two peaks in Fig. 4.4.1 for an 'by hand' approximation, a temperature coefficient would be about $-0.5\%/^{\circ}\text{C}$.

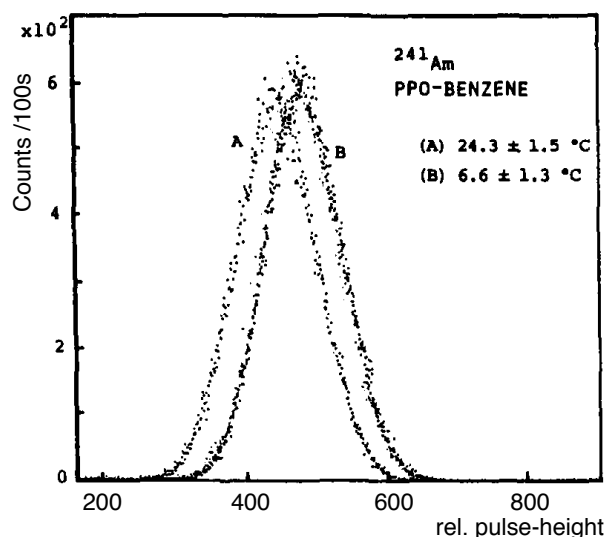


Figure 4.4.1: Pulse height distribution of ^{241}Am α -decays in a benzene + 4 g/l PPO solution. The x-axis shows the pulse height in arbitrary units. Taken from [Hom87], modified.

Nevertheless they do report consistently for all scintillator mixtures and both radiation types a significant increase in light output at lower temperatures. They argue that this phenomenon strengthens the hypothesis that enhanced excimer formation at lower temperatures can be held responsible for the effect. This is in sharp contrast to the results reported in [Mat85], which will be discussed in detail later in this section.

In 1999 Buontempo et al. [Buo99] investigated a variety of combinations of four solvents and four solutes. Irradiated with a ^{90}Sr β -source, when a neutral gas was present, a light yield increase of $\approx 10\%$ was observed at -10°C . Unfortunately again, temperature effects on the PMT were ignored and a setup scheme shows that the cooled and heated cuvette was directly mounted on to the PMT, thus having direct thermal contact.

The so far last and best work was published by Xia et al. [Xia14]. This group built a detector setup much alike the one developed for this thesis. A ^{137}Cs γ -ray source was used in a Compton scattering setup that could be heated and cooled. To account for PMT sensitivity changes, an external (not cooled) LED light source was used to generate pulsed reference light, which was led via an optical fibre onto the PMT. With this technique they exclude any hysteresis effect and measure and correct for the changes in the PMT sensitivity. Figure 4.4.2 shows their results for two scintillator types. Unfortunately they do not report the exact composition of the liquids tested, nor do they accompany all of the quantitative results with the respective uncertainties. When approximating the LAB data in Fig. 4.4.2 linearly, the resulting temperature coefficient would be $\approx -0.32\%/^{\circ}\text{C}$.

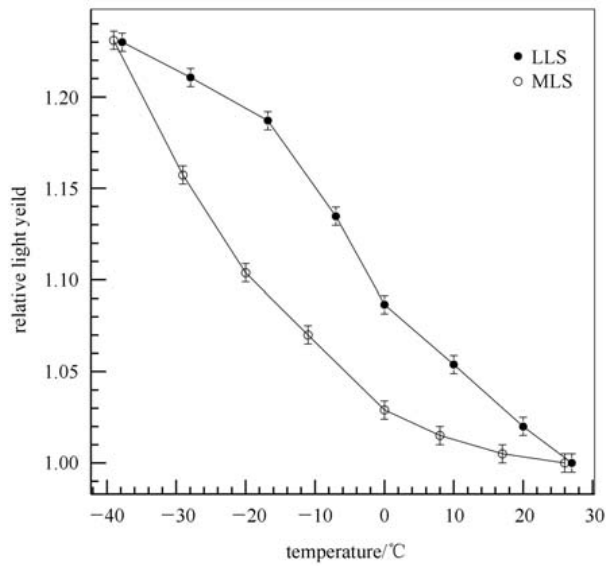


Figure 4.4.2: Relative light yield of LAB based (LLS) and mesitylene based liquid (MLS) scintillator with already applied PMT sensitivity correction. Normalised to 26° C. Taken from [Xia14].

Even though most of the previous studies presented here have significant conceptual problems or report only coarse results, all show consistently that organic liquid scintillator solutions yield more light at lower temperatures.

The physics explanation remains rather unclear. An insightful study is the work by Mathad and Umakantha [Mat85], as it was mentioned earlier. They determined the energy transfer parameter k_{YX} at six temperatures in their scintillator mixture (10% toluene with 90% cyclohexane as solvent and 3-phenylindole-1-propionitrile as single solute). Moreover they measured the viscosity (η) of this liquid at these temperatures. As k_{YX} varies linearly with the diffusion parameter T/η , they conclude that excimer formation can only contribute to a minor degree to the energy migration in this liquid scintillator solution, by using the following arguments:

- In benzene and alkyl benzene, the resonant multipole-multipole interaction energy is about 0.35 meV and the thermal energy of the molecules is about 25 meV. **Therefore the energy migration due to resonance interaction should be independent of temperature.**
- excimer binding energy is with about 250 meV large compared to the average thermal energy. As this can be characterised as an activation process, its **temperature dependence is expected to be exponential**
- diffusion is rather simply proportional to the diffusion constant T/η

Thus:

$$k_{YX} = \alpha + \beta e^{-\epsilon/kT} + \gamma(T/\eta) \quad (4.13)$$

where α is the constant describing resonance interaction, in the second term η is the activation energy of the excimer formation - dissociation process and β and γ are constants. When k_{YX} now only varies linearly with T/η , the conclusions are that excimer formation does not contribute significantly to energy migration and that instead resonance interaction and diffusion are most important.

CHAPTER 5

**Temperature quenching
measurements**

THE goal of the investigations carried out at the Helmholtz Zentrum Dresden-Rossendorf (HZDR) was to shed light into the not well known behaviour of liquid scintillator light output at temperatures different than room-temperature for α -particles and electrons. As explained in the previous chapter (Ch. 4), liquid scintillator physics and previous studies would predict temperature coefficients at the small percent scale, $\sim 0.2\%/^{\circ}\text{C}$. In order to measure such small changes precisely, a detector is needed that is very stable with temperature change and gives reliable and reproducible results. With these prerequisites in mind, a liquid scintillator detector was developed and built at HZDR and used to carry out the measurements as intended and explained in the following sections.

5.1 Experimental setup

5.1.1 The detector

In order to efficiently change, and keep the temperature of the liquid scintillator stable, the vessel for the liquid must conduct heat well and was thought to be bathed with a cooling liquid. To achieve the desired behaviour, a solid block of aluminium was machined into the shape that can be seen in the computer-aided design (CAD) drawing in Fig. 5.1.1 and in Fig. 5.1.2. A mixture of water and glycol is flushed through small pipes in the block by a cooling device, which can change the liquids temperature in between -30°C and $+40^{\circ}\text{C}$.

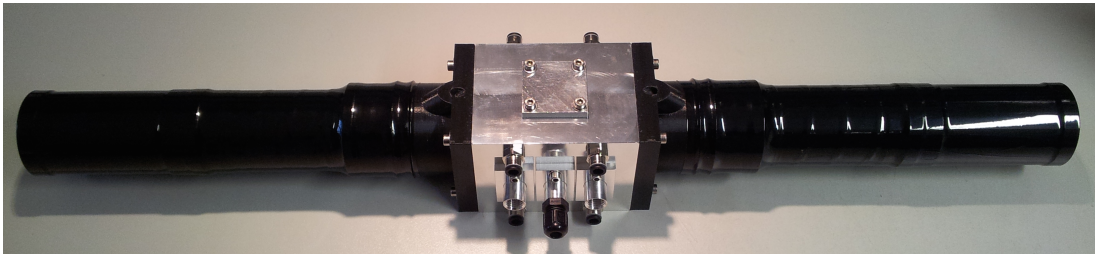


Figure 5.1.1: Picture of the assembled detector with the aluminium cuvette in the centre and the black PMT mounts attaching the two Hamamatsu R2059 PMTs.

Despite better temperature stability of other light sensing devices, PMTs are chosen to detect the scintillation light, because they still perform very well in counting small amounts of photons with superior time resolution. Furthermore are PMT characteristics well known and their application is fairly uncomplicated. Also, with a good time resolution, a coincidence measurement of two PMTs greatly suppresses signal background by electronic noise, PMT dark currents and other unphysical noise. It also improves the light collection from the liquid scintillator, which in turn results in a better energy resolution. Therefore two Hamamatsu R2059 PMTs are mounted opposing on to the aluminium block, separated from the liquid scintillator by UV transparent acrylic light guides and quartz glass windows. These light guiding components are connected with each other by a silicon grease from Bicon (BC-630), which matches the increasing refractive index of the parts. The light guides decouple

the PMTs thermally from the cooled liquid, since the PMT sensitivity is known to significantly change with temperature [Lau58; Ham07; Fly02]. As this decoupling can not be in any way perfect, PMT gain changes are still expected and addressed by a gain monitoring/correction technique.

To make sure that all PMT gain changes are noticed and can be corrected, an independent light source is used to monitor the PMT response. For this purpose, a light emitting diode (LED) pulser was developed in cooperation with the electronics lab at HZDR and will be explained in detail in section 5.2. The light from the LED is lead through two optical fibres directly pointing at the PMT cathodes, and simultaneously on to an independent photodiode. The diode is thermally decoupled from the PMTs and itself known to be very stable against temperature changes.

For different practical reasons and mainly to prevent air moisture condensation on the PMT bases, a custom built box was used to enclose the detector with a nitrogen atmosphere. This insulated plastic container also extends the achievable temperature range of the detector and thermally decouples all read-out electronics and the LED pulser from the detector. A schematic overview of the setup and read-out electronics is given in Fig. 5.1.3.

The temperature changes are monitored in three places independently. First, two sensors are 'glued' into two separate aluminium caps with heat conducting paste and those caps are in turn placed into the wall of the aluminium cuvette, see the light grey cylinder in the top drawing in Fig. 5.1.2. This ensures optimal thermal contact with the liquid scintillator, as the actual DS18B20 digital semiconductor thermometers are incompatible with LAB. A third sensor is placed inside the nitrogen box, monitoring the temperature and humidity. Those sensors provide a temperature measurement precision of 0.044°C and an accuracy of 0.5°C .

To achieve the coincidence detection and also including the signals from the LED, the electronic signals from the PMTs are split and simultaneously lead to a nuclear instrumentation module (NIM) electronics crate for coincidence- and counting logic, and to a flash analog-to-digital converter (FADC). The two 'raw' voltage signals from the PMTs are read by two constant fraction discriminators, and when passing the threshold, a NIM logic signal is send to a fast coincidence unit. This device evaluates the presence of two logic signals in an adjustable time window of $1\text{ ns} - 1\ \mu\text{s}$, and if so, sends itself a rectangular pulse to the external trigger input on the FADC. This Acquiris DC-282 fast digitiser then starts the read-out of all four input channels (1: PMT₁, 2: PMT₂, 3: Photodiode, 4: LED Trigger), starting 350 ns backwards in time, using its internal buffer. With 2 GS/s sampling rate (one sample every 0.5 ns, 10bit resolution and variable dynamic range between 1 - 5 V), it provides excellent data and pulse shape analysis capabilities.

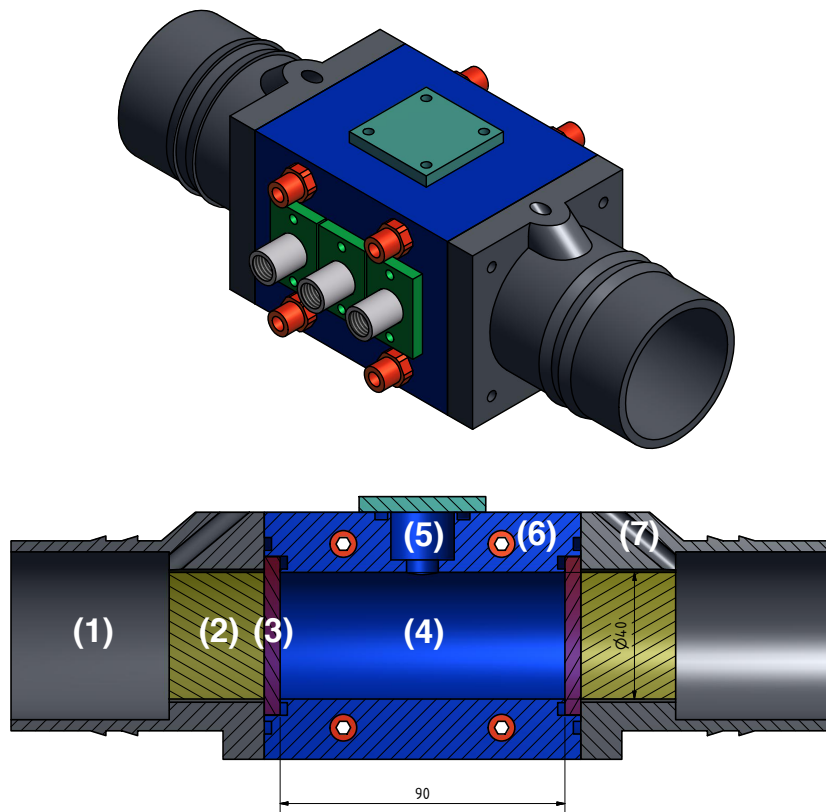


Figure 5.1.2: 3D CAD drawing (top) and 'cut' (bottom) of the aluminium cuvette (blue) with the PMT mounts (dark grey) and the light guides (yellow).

- (1) **The PMT mounts** are a 3D-printed support for the PMTs, made from acrylonitrile butadiene styrene (ABS) material with optical fibre feed through on top (7). These are screwed on to the aluminium body (4) and press the quartz glass windows (3) and fluoroelastomer (FKM) gaskets into place, closing the liquid scintillator volume.
- (2) **The acrylic light guides** are turned into cylindrical shape and (in a second development step) have been coated with a special titanium oxide colour (with very high reflectivity) on the outside, in order to increase reflection and therefore the light guiding effect (see section 5.1.3). Their UV transparency has been verified in a dedicated UV spectrometer measurement.
- (3) **The quartz glass windows** are 0.5 mm thick, known to be compatible with LAB and match the increasing refractive index in the materials that guide the scintillation light towards the PMTs.
- (4) **The aluminium cuvette** is 9 cm long, 4 cm in diameter and thus encloses a volume of ≈ 113 ml. It was, also in a second development step, coated with titanium oxide colour on the inside to increase reflectivity and therefore light collection on to the PMTs (see section 5.1.3). The main volume is connected to a small

buffer volume on top (5). The aluminium is penetrated by four pipes for a circulating cooling liquid (6).

- (5) **A small buffer volume** also serves as filling/emptying port and is closed with an aluminium lid and FKM gasket.
- (6) **Four pipes** are flushed with a circulating glycol-water mixture which is cooled or heated by a cooling device (Endocal RTE-100).
- (7) **A feed through** for an optical fibre to point directly on to the PMT cathode. This is used to send light generated by an LED simultaneously on the two PMTs (see section 5.2).

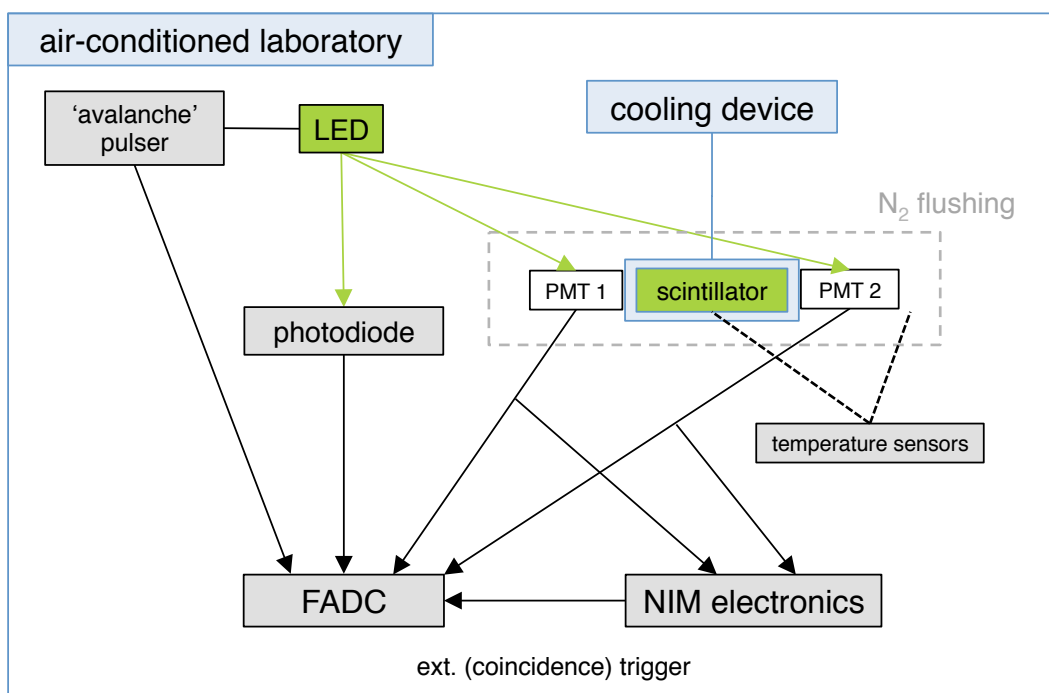


Figure 5.1.3: Schematic drawing of the experimental setup in an air-conditioned laboratory with the liquid scintillator detector inside an insulated box with nitrogen atmosphere. All PMT read-out electronics, temperature sensors as well as the pulser components are outside this box under very stable conditions. Green lines symbolise the light path from the LED light, blue lines indicate cooling and solid black lines the direct read-out by a separate FADC channel.

5.1.2 Commissioning and data acquisition

In order to use such a detector, all components in contact with the liquid scintillator need to be compatible with LAB and all parts of the mixture, free of grease and any kind of water or moisture. The cleaning of the components and their assembly therefore has to be carried out very carefully and is time consuming. All parts were

cleaned with de-ionised water, ethanol and lastly with isopropanol. Dried in a heated vacuum oven and after assembly put into a nitrogen atmosphere.

The compatibility of polished aluminium and quartz glass with LAB is known, but the Viton/DuPont FKM material intended as gaskets (O-rings) had to be separately tested. This was done by exposing the O-rings to pure LAB for several weeks, visual inspection and comparing their UV transmission profiles with a UV spectrometer (see section 5.3). As there was no change observed, this material was accepted to be compatible with LAB and used in this detector.

Before filling the detector with a LAB mixture, the liquid scintillator ideally has to be free of dissolved oxygen and therefore 'washed' with nitrogen (refer to section 4.2). A special gas-washing bottle was modified to (nearly) gap-less fill the liquid into the setup, all under nitrogen atmosphere. In order to be able to compare different mixtures, the usual total disassembling of such a detector for a change of the liquid is disturbing, since the mount of the PMTs and their optical connection can never be exactly the same. That is why a technique of fill - empty - refill was developed, in such a way that the detector does not need to be taken apart and re-assembled. This provides better comparability, even though the optical properties of the liquid itself can oppose problems in doing so.

Data acquisition and basic analysis

As explained in the previous section and depicted in Fig. 5.1.3, once the coincidence logic is triggered by a scintillation event, another square shaped voltage pulse triggers the read-out of all four channels on the FADC. The data from these channels (**1**: PMT₁, **2**: PMT₂, **3**: Photodiode, **4**: LED Trigger) can all be acquired with different dynamic range, but have to be on the same time base and sampling interval. An example with many pulse shapes in a 2D histogram is shown in Fig. 5.1.4.

In order to extract a reliable information about the detected amount of light from these pulse traces, the integral of the pulse is used, instead of a peak height information. The maximum voltage output is much more likely to be distorted by noise on the signal, than the pulse area. A simple sum of the two integrals provides some information about the total amount of light in the detector. A much better measure is the geometric mean of both integrals, due to the geometry of the device.

Considering isotropically produced light and homogeneous reflectivity on the vessel walls, the following simple estimation illustrates the advantage of using the geometric mean: The PMTs are separated by the scintillator of the length l . For each point x along this axis, the intensity of light generated at x , reaching PMT₁ and PMT₂ can be estimated by:

$$I_1(x) = I_0 \times e^{(-\lambda x)} \quad \text{and} \quad I_2(x) = I_0 \times e^{(-\lambda(l-x))} \quad (5.1)$$

the geometric mean leads to:

$$I(x) = \sqrt{I(x)_1 \times I(x)_2} \quad \text{thus} \quad I = \sqrt{I_0^2 \times e^{-\lambda(x+l-x)}} \quad (5.2)$$

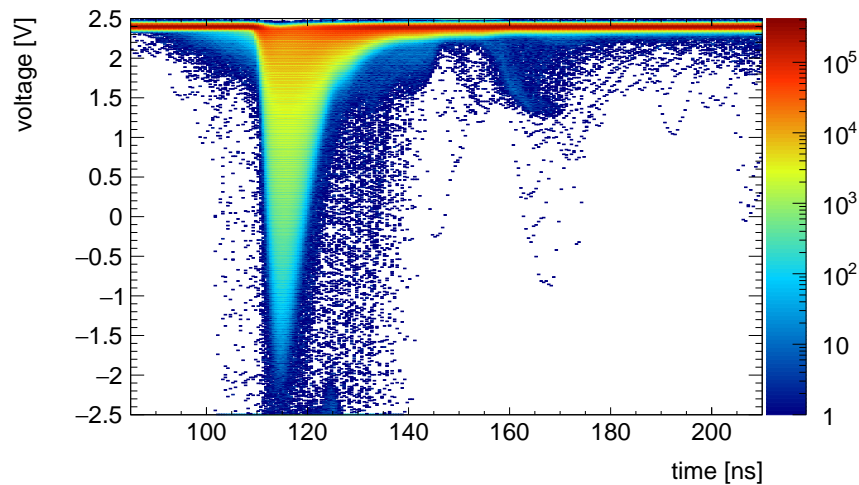


Figure 5.1.4: Pulse shapes from $\approx 1,5$ million events detected with one PMT in LAB + 5 g/l PPO + 25 mg/l bis-MSB and a ^{60}Co calibration source placed on the detector. The colour code indicates the entries per bin. The smaller 'bump' after the main scintillation peak is due to overcompensation of the PMT base at events with very high voltage output from the PMT. These are typically caused by cosmic ray muons, for more details on this refer to section 5.6.

which is only dependent on the total length of the scintillator, but not on the position x of the light generation:

$$I(l) = I_0 \times e^{-\frac{1}{2}\lambda l} \quad (5.3)$$

A comparison of the two single spectra with the geometrical mean spectrum can be seen in Fig. 5.1.5. In order for this technique to work, the gain of the two PMTs needs to be matched correctly, assuring that the same amount of light generates the same voltage pulse area on both PMTs. This is done by placing a gamma-ray source at the centre of the detector (± 0.5 mm) and adjusting the PMT high voltage in fine steps accordingly.

5.1.3 Detector developments

While building the detector and running it for the first measurements with pure LAB scintillator (LAB + 3 g/l PPO), it was noticed that the setup did not achieve an energy resolution as good as previous measurements with similar LAB mixtures in other detectors at HZDR.

A first step in addressing this, was a measurement campaign to find the best values for the coincidence time window, the type of discriminator (constant fraction vs. leading edge), discriminator threshold and the type of coincidence logic (AND vs. OR). Energy spectra of gamma ray calibration sources, energy resolution and background rates were compared. A clear preference for the constant fraction discriminator (CFD) and AND-logic was found. The CFD thresholds were then kept for all measurements at 20 mV and the coincidence window adjusted to 30 ns.

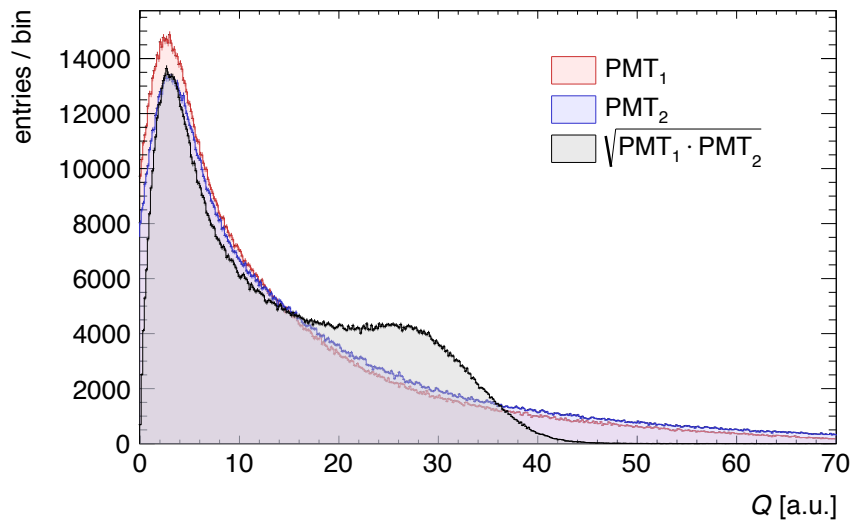


Figure 5.1.5: Pulse area spectra from a ^{60}Co calibration source placed on the detector that is filled with LAB + 5 g/l PPO + 25 mg/l bis-MSB. Due to the gamma-ray energy, the full energy peak is not visible, only the Compton-Edge is clearly pronounced. A detailed explanation of the calibration spectra can be found in section 5.4.

Secondly, as the inside of the aluminium cuvette was only polished aluminium, an improved reflectivity and thus better light collection, seemed to be a reasonable improvement. A special two component TiO_2 paint (Bicron BC-622A) is especially chemical resistant to aromatics and thus is also compatible with LAB and has a good reflectivity profile, shown in Fig. 6.1.1a.

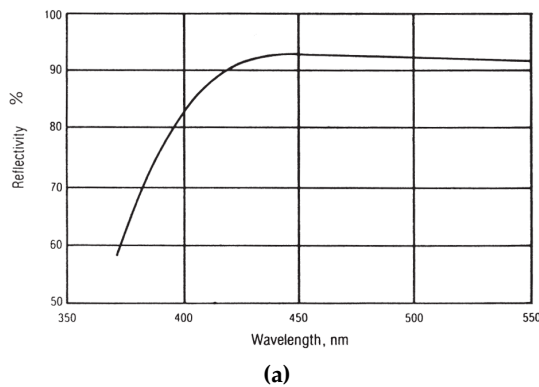


Figure 5.1.6: (a) Reflectivity spectrum of BC-622A white titanium dioxide paint. Taken from [Sai14]. (b) White paint on the inside of the aluminium cuvette. The filling hole and one hole for one of the thermometers is visible on the right.

The paint was applied to the inside of the aluminium cuvette, which was sanded before application in order to assure good adhesion and homogeneous coating. The same colour was applied to the outside of the acrylic light guides.

In Fig. 5.1.6, it is clearly visible that the reflectivity of the paint drops significantly below ≈ 420 nm. Since this is also the case for the sensitivity of the photomultiplier tubes (see Fig. 5.2.2a in section 5.2.1), the addition of a second wavelength-shifting fluor (bis-MSB) seemed beneficial. This shifts the emission maxima of the liquid scintillator towards $\approx 400 - 420$ nm and therefore increases the amount of detected light effectively. The combined effect of these measures is depicted in Fig. 5.1.7.

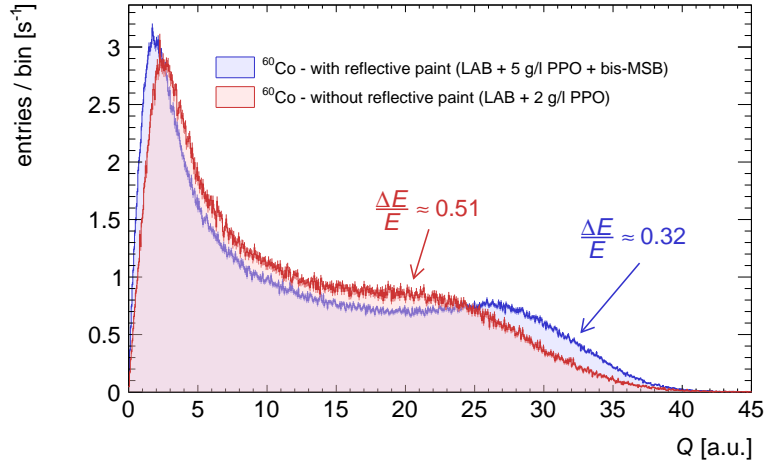


Figure 5.1.7: Comparison of two ^{60}Co charge spectra. In **red**, the original scintillator mixture with LAB + 2 g/l PPO and no reflective paint. In **blue**, LAB + 5 g/l PPO + 20 mg/l bis-MSB and reflective paint inside the cuvette and outside the acrylic light guides.

The effect of a significantly improved energy resolution at the position of the Compton edge (E_c), from

$$\frac{\Delta E_c}{E_c} = 0.51 \pm 0.05 \quad \text{without white paint, to} \quad \frac{\Delta E_c}{E_c} = 0.32 \pm 0.04$$

with the coating, is clearly visible. Even though this is a great improvement for the whole setup and measurement campaign, this is unfortunately still not good enough to distinguish the two close gamma lines of ^{60}Co at 1173 keV and 1332 keV. In this special case, the arithmetic mean of the energies has been used to approximate the energy resolution.

5.2 PMT sensitivity control

As already briefly noted in section 5.1, the major objective of this work is to detect the scintillation light from temperature changing liquid scintillator. It has also been stated that the design of the setup incorporated a thermal decoupling of the PMTs from the cooled or heated aluminium cuvette and the liquid. With a thermal conductivity of $\lambda \approx 0.2 \text{ W m}^{-1} \text{ K}^{-1}$, the acrylic light guides insulate the PMTs well, but not 100%. Also the box, in which the detector is placed to be bathed in a nitrogen

atmosphere, reaches a thermal equilibrium with the cuvette after some hours. That is why temperature changes of up to $\mathcal{O}(10^\circ\text{C})$ on the PMTs are expected.

The sensitivity and light amplification of the PMTs varies significantly with temperature [Lau58; Ham07; Fly02]. An overview for Hamamatsu PMTs is shown in Fig. 5.2.1. The 'anode sensitivity temperature coefficient' shown, combines wavelength dependent temperature effects on the photocathode sensitivity and the wavelength independent gain changes of the dynodes. The flat profile of the temperature coefficient for bi-alkali tubes (as they are used in this setup) leads to a coefficient of $\approx -0.4\%/^\circ\text{C}$.

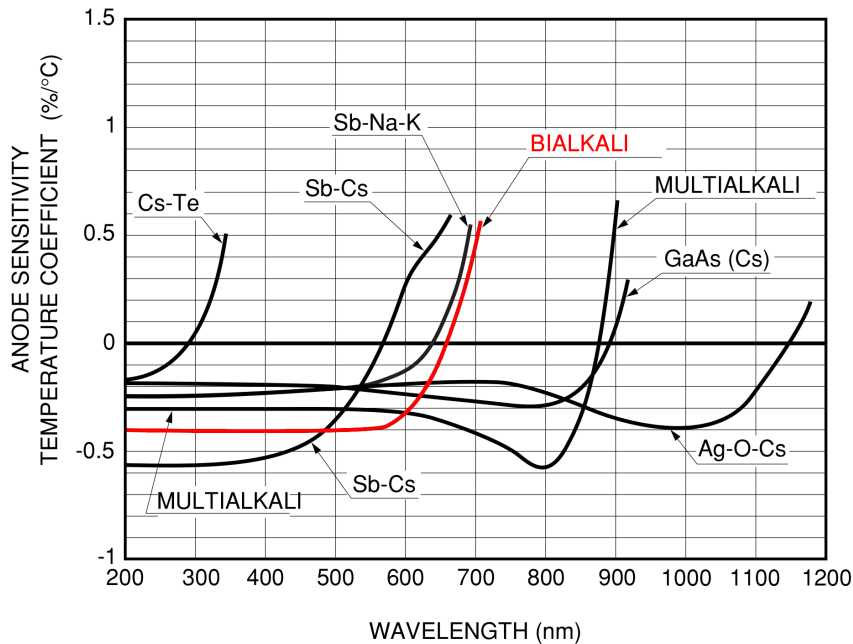


Figure 5.2.1: Anode temperature sensitivity coefficients for different photocathode materials in Hamamatsu PMTs, taken from [Ham07]. The bi-alkali type that is used in this setup is shown in red.

As these changes occur on long timescales in an evacuated phototube, they are difficult to quantify for individual and not identical phototubes, a dedicated control of the PMT sensitivity is necessary. The following sections shall describe how this PMT sensitivity control was developed, tested and applied to the measurements with varying temperature.

5.2.1 Hardware

The schematic overview in section 5.1 (Fig. 5.1.3) already shows the main concept of the sensitivity control: A custom built pulser drives a light emitting diode with a variable frequency to generate very short light pulses of $\mathcal{O}(10\text{ ns})$ that are as similar as possible to the light emitted from the liquid scintillator. This light is then split and lead simultaneously on to the two PMTs and a separate (and thermally fully decoupled) silicon pin-photodiode outside the N_2 -box. The photodiode (Alphas

UPD-200-PS) is insensitive to temperature changes [Alp] and operated under very stable conditions inside the air-conditioned laboratory room. This independent signal serves as normalisation and control that the amount of emitted light from the LED is constant. As the same light hits the PMTs coincidentally, every pulser-event generates a real coincidence event and is triggered by the detector logic. Every time the driver generates a pulse with the LED, a square shaped trigger pulse is sent to one of the FADC channels. This is later used as a tag for LED events, that can then be 'cut' from the actual physics data set. The adjustable frequency of the pulser allows to adjust to different signal activities and avoid random coincidences. This is important for measuring times, the statistics of LED pulses on the PMTs must not be too low.

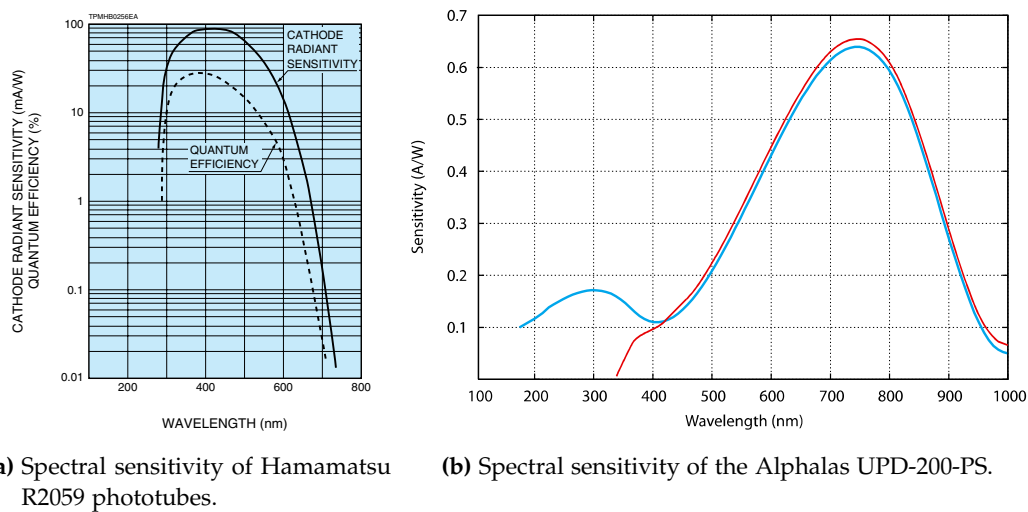


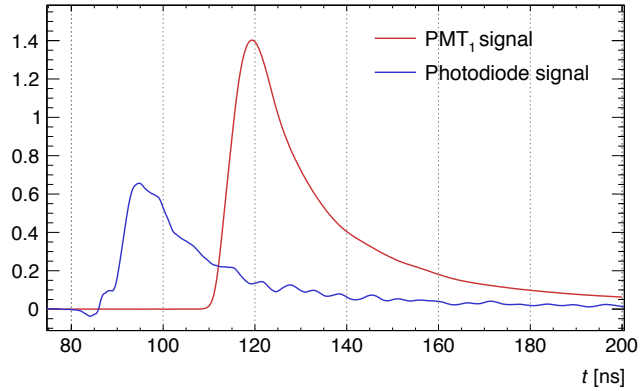
Figure 5.2.2: Comparison of the sensitivity of the PMTs [Ham10] (a) and photodiode [Alp] (b) used in the detector setup. Note that the LED peak wavelength is 428 nm.

A problem encountered are the different sensitivities of the PMT and the photodiode. As can be seen in Fig. 5.2.2, the overlap of the spectral sensitivities of the two components is small. Tests with several LED types and wavelength have been carried out and as a result a LED (Vishay TLHB44K2M1) with 428 nm peak wavelength has been chosen. This suites not only the spectral overlap of the two light sensing components, but is also in the range of the liquid scintillator emission spectrum (see section 5.3), as intended. Figure 5.2.3 shows pulse shapes from both, phototubes and photodiode, as they are generated by the light emitting diode.

5.2.2 Proof of concept

Before starting 'real' measurements with α emitting isotopes or gamma-ray sources, it is very important to show and proof the concept of the sensitivity control. Therefore, extensive test have been undertaken to show that the light reference by the LED pulser is stable, reliable and that it actually can be used to correct for PMT sensitivity changes by ambient conditions.

Figure 5.2.3: Comparison of average pulse shapes from ≈ 1 million LED pulser events as they appear on one PMT and the photodiode. With a rise time shorter than 175 ps, the photodiode is able to resolve small 'ripples' of the LED signal, caused by the LED driver circuit. The time shift is solely caused by the trigger logic delay.



In order to do so, long time measurements of up to 24 h were made to guarantee thermal equilibrium of all parts and gain insights into time stability. As the background rates in the pure LAB (+ 5 g/l PPO + 20 mg/l bis-MSB) mixture are very low, with ≈ 40 Hz (integral over the whole energy spectrum) and a coincidence time window of 30 ns, random coincidences with the pulser are negligible:

$$R_{\text{random}} \approx 2 \times \tau \times R_{\text{background}} \times R_{\text{pulser}} = 2 \times 30 \text{ ns} \times 40 \text{ Hz} \times 20 \text{ Hz} = 4.8 \times 10^{-5} \text{ Hz}$$

These long measurements were then divided into hour-'slices' to observe changes on this time base. A pulser rate of 20 Hz results in 72,000 events per hour on the PMTs and photodiode and thus enough statistics for such an analysis. The resulting gaussian shaped peaks in the charge spectra were fitted with a standard Gaussian and the mean and the fit uncertainty on the mean were extracted. A graph for this analysis with one PMT and the photodiode is shown in Fig. 5.2.4 and Fig. 5.2.5, respectively. In this case, after 24 h at room temperature, the cooling device was used to lower the temperature of the liquid scintillator to $\approx 5^\circ \text{C}$. This temperature change can be seen on the left side of the diagrams. After ≈ 4 h, the final temperature is reached, and kept stable by constant cooling. The influence on the PMT sensitivity of the ambient temperature change is clearly visible. It seems that after about 5 h a thermal equilibrium is reached and the differences between the hourly data points turn into a more or less random scatter of the order $\mathcal{O}(0.1 - 0.2\%)$. Note that these data points are hour averages and the deviation from the overall mean.

From this observation it was concluded that a time of at least 6 h needs to be in between the set of a new temperature on the cooling device and actual data taking. In practise, the cool down and warm up periods were during the night and the time span before measuring at least 18 h. Furthermore, it could be shown that the LED pulser and / or the photodiode read-out is long time stable to $\pm 0.1\%$. This allows to measure changes in the amount of light hitting the PMTs of the order $\mathcal{O}(1\%)$, which was the prerequisite to test the influence of ambient temperature on the light yield.

In a second step, the application of a correction to real data, that was taken at different temperatures, needs to be shown.

As explained before, since the pulser trigger signal is also recorded every time the LED is lit, these events can be 'cut' from the data-set and analysed separately. Because these pulses are gaussian distributed around their mean, a standard gaussian

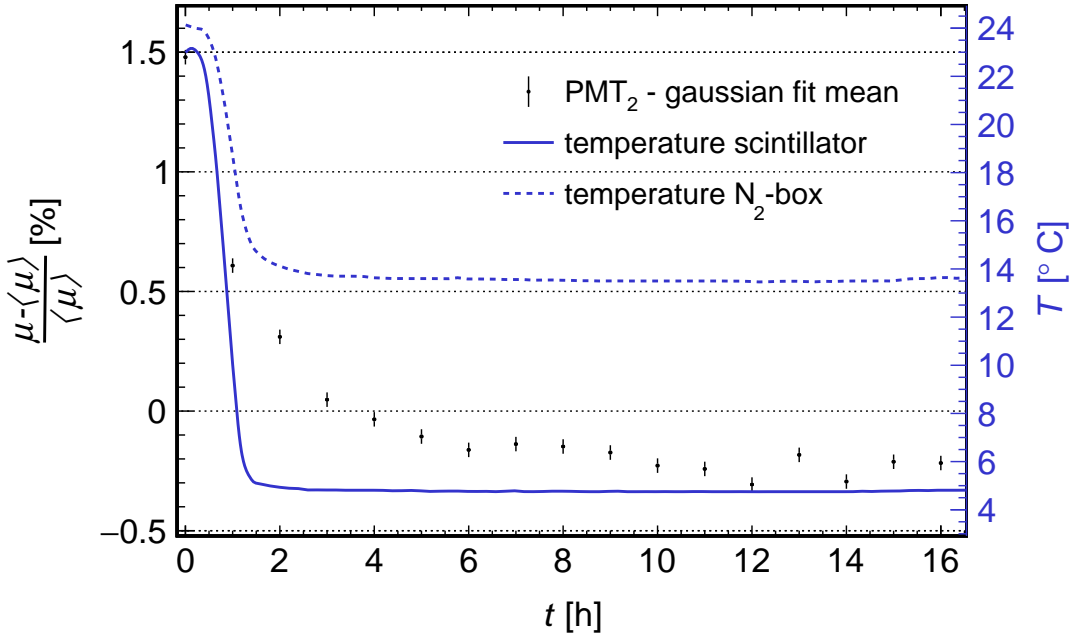


Figure 5.2.4: Time analysis of PMT sensitivity during a temperature change of the liquid scintillator. The solid blue line indicates the temperature and the black data points are the mean values from a gaussian fit to the charge spectra, for one hour each. The error bars show the $\pm 1\sigma$ uncertainty from the fit.

function is used to fit the data and to extract the mean value and fit uncertainty (e.g. see Fig. 5.2.6). Once this is done for both measurements, the correction factor can be calculated simply as the ratio of the two LED pulser mean values.

Since the signal from the photodiode is meant to be very stable, any shift from this source can then be subtracted from the correction quotient, as this would indicate a slight change in the light that hits the PMTs. This correction factor can then be used to scale the pulse integral on an event by event basis. As a test, two measurements with a ^{22}Na calibration source were carried out, one at room temperature and one at $\approx 5^\circ\text{C}$. In this case, the calculated factors are: $C_{PMT-1} = 1.024 \pm 0.001$, $C_{PMT-2} = 1.015 \pm 0.001$ and $C_{Diode} = 1.0014 \pm 0.0003$. The comparison of the spectra from the LED signal and the ^{22}Na calibration source can be seen in Fig. 5.2.7 and 5.2.6 respectively. A closer look at Fig. 5.2.7 reveals a small change of the Compton edge towards higher charge values for the cooled scintillator. With the application of the gain correction, this effect is reduced and the corrected spectra ‘moved’ towards the room-temperature position. This is the expected behaviour of the sensitivity correction via a separate light source, as it is applied in this setup.

A last, yet very important test is the effect of temperature changes on the pulse shapes of the LED on the PMTs. While the photodiode is perfectly thermal decoupled from the cooling device, the PMTs undergo temperature changes. With its 2 GS/s, the FADC has the capability to record the pulse shape of the PMT voltage pulses. This

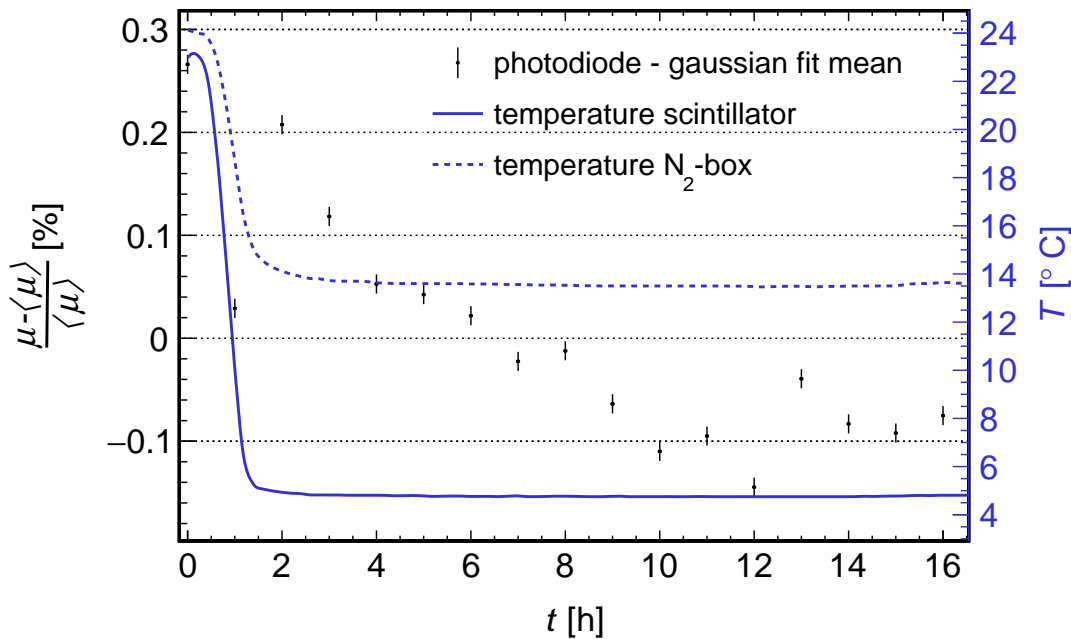


Figure 5.2.5: Time analysis of photodiode signals during a temperature change of the liquid scintillator. The solid blue line indicates the temperature and the black data points are the mean values from a gaussian fit to the charge spectra, for one hour each. The error bars show the $\pm 1\sigma$ uncertainty from the fit.

is in fact done for all measurements from all light sources. Here, only the tagged LED pulses are of interest, at different temperatures. Fig. 5.2.8 shows an overlay of average pulse shapes of LED pulser events on PMT-1, at five temperatures. As it will be also the case later, the arithmetic average of the voltage value is calculated at each sample position (0.5 ns bin), as well as the variance of the voltage values. Since the variance is very small and the amount of pulses large (≈ 150 k), the uncertainties are too small to be visible here. It can be noted that, clearly the temperature variation has no effect on the shape of the LED pulses on the PMTs and therefore that the PMTs do not produce different pulse shapes at different temperatures.

5.3 LAB absorption and emission spectroscopy

Before using the cooling capability of the detector, it is necessary to test the overall chemical stability of the different LAB mixtures especially at lower temperatures, as the solubility of fluors and surfactants decrease. Therefore two standard measurements are undertaken, one with a device testing the light transmission, and one that is able to excite the fluorescence and detect the emitted light. Both are able to change the temperature of the sample, yet not in the same way and quality. Changes in the transmission or emission spectra with temperature could hint to some kind of precipitation of the dissolved ingredients in the LAB.

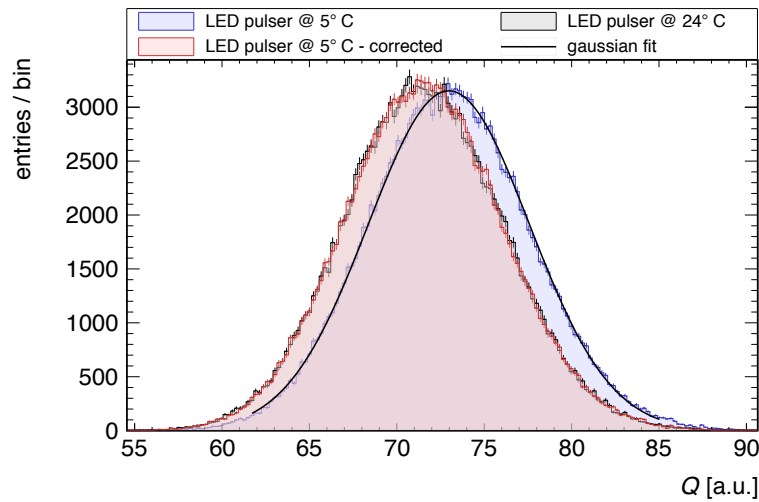


Figure 5.2.6: Comparison of charge spectra from the LED pulser, obtained at $\approx 5^\circ\text{C}$ (blue) and $\approx 24^\circ\text{C}$ (black). The red one is generated from the same data as the one in blue, but with the correction applied, event by event. The solid black line shows the gaussian fit to the low temperature data.

First the transmission of light in the wavelength range of 190 nm to 600 nm is tested at three temperature points (24°C , 5°C , -4°C) with a UV transmission spectrometer, Jasco J-815. The chosen temperatures are rather limited due to the intended use of the device for bio-chemical studies. The J-815 makes use of a Peltier element for thermoelectric cooling and heating. The UV-transparent acrylic cuvette is placed inside a cavity that is air-tight sealed and flushed with nitrogen, in order to prevent condensation on the sample. The temperature of the sample is constantly monitored and waiting times of several minutes ensure that the very small liquid volume of about 3 – 6 ml has reached thermal equilibrium. In the case of these measurements a 5 mm thick sample was used. The absorption profile of the empty cuvette was acquired first and then subtracted from all following data. Also a base line correction is applied. The results for ‘pure’ and Samarium loaded LAB (see sec. 5.7) at three temperatures each, can be seen in Fig 5.3.1.

Both mixtures show the same overall trend with good transparency above 410 nm wavelength and steep rise of absorption in between 400 nm and 360 nm. Below that, both are nearly opaque. The pure LAB solution shows a very smooth curve at all temperatures, without distinct features. At room-temperature and 5°C , the absorption is mostly the same, only below 400 nm is the cooler LAB slightly less transparent. A somewhat overall larger opacity is observed for the pure LAB at -4°C . This might be due to a baseline shift or offset, especially since this behaviour is not observed for Samarium loaded LAB. According to the manufacturer, the accuracy of the device is $\sim 2.3\%$ which could, to some extent, account for this effect.

In a custom built and well designed setup, Xia et al. [Xia14] explicitly measure the transmittance of light with a wavelength of 430 nm in a temperature range of $[-40^\circ\text{C}, 25^\circ\text{C}]$ and report a constant behaviour with an uncertainty of 2%. This

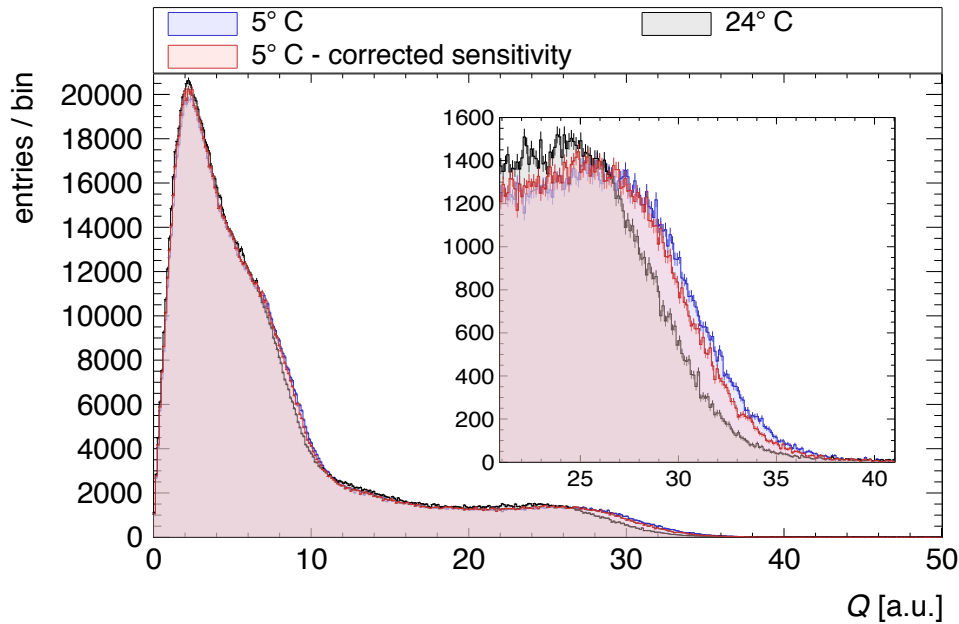


Figure 5.2.7: Comparison of two ^{22}Na charge spectra. The higher Compton edge is clearly visible. The lower one is less pronounced at this low energy and merged with the back-scatter feature. In black, the spectrum obtained at $(23.65 \pm 0.04)^\circ\text{C}$, and in blue the one from the measurement at $(4.80 \pm 0.04)^\circ\text{C}$. The red spectrum is generated from the same data as the blue one, but with the sensitivity correction applied, event by event. Inlay shows a zoom at the upper Compton edge.

strengthens the interpretation that the larger increase in absorbance at -4°C is probably caused by an offset of the device.

As expected, the Samarium loaded LAB shows a few small features not visible in the pure LAB absorption profile. They are very much the same at the three temperatures and show only small differences below 400 nm.

One fact that has been so far neglected is the density change of the liquids with temperature. The density of 'pure' LAB 0.86 g/cm^3 at room-temperature [Pet09] increases about 1.4% at 5°C and about 2% at -4°C [OKe09], which in principle should decrease the transparency slightly. This should affect the whole absorbance spectrum, which is not observed for 5 of 6 measurements shown in Fig. 5.3.1. And as it is also not seen by Dong-Mei et al. in completely independent investigations, one might conclude that the effect is too small to be visible in this type of measurement and its uncertainties.

Nevertheless it can be stated that temperature changes down to -4°C do not influence the solubility of the Samarium in the LAB, as much larger changes are expected and not observed. The optical properties also seem not change significantly with temperature variation in this range, which is close to the temperature spectrum that will be used in the later measurements with the new detector.

For the second test the Perkin-Elmer LS 55 fluorescence spectrometer was used. It is able to excite a small liquid volume with UV light of varying wavelength and

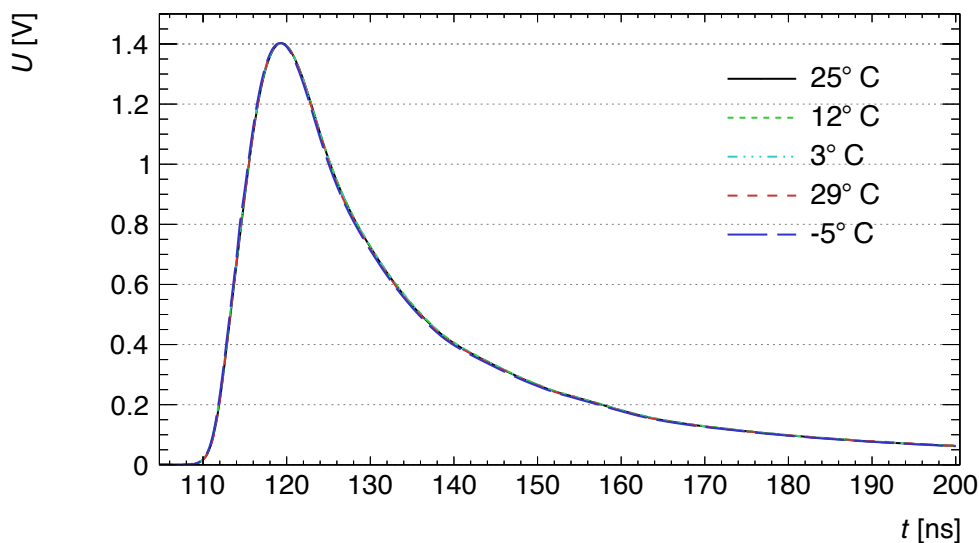


Figure 5.2.8: Average pulse shapes from PMT-1 at five temperatures, generated by the LED pulser. The sample by sample average is generated from ≈ 150 k pulses at each temperature. PMT-2 shows the same behaviour.

simultaneously detect the emitted light. In this case, the chosen excitation wavelength was set to a constant 380 nm. This turned out to be a good compromise of effective excitation and not disturbing the main emission spectrum with its maxima at around 400 nm and 420 nm. Although the original device did not support heating or cooling of the samples, a water cooling circuit was installed subsequently. This obviously limited the temperature range on the lower side to just above 0°C and therefore only two points were measured. Another great disadvantage of the not fully integrated cooling is that the sample volume is not gas-tight or flushed with nitrogen. This is the most likely explanation why the emission spectra for the lower temperature are less intense. Probably some condensation shielded the excitation and emission light at the cuvette surface. Previous investigations by Homma et al. [Hom85a; Hom87] found the opposite effect, more or less expressed. Otherwise both mixtures show the same emission features with the maxima at the same position. Beside the already discussed decrease in intensity, again no significant change in the shape of the cooled samples could be found.

In conclusion, combining both investigations, it can be stated that the cooling of the samples did not destabilise the mixtures or that any precipitation or crystallisation took place. The optical properties did not change in a significant way with varying temperature.

5.4 Energy calibration

One of the most important steps in building a particle detector and performing reliable and reproducible measurements, is a thoroughly carried out energy calibration.

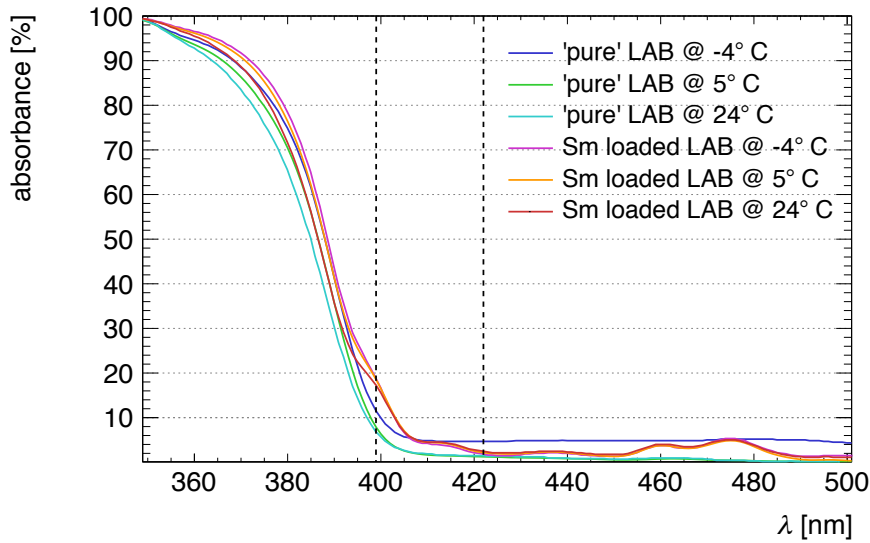


Figure 5.3.1: Absorption of light in the UV and visible range in 'pure' LAB (+ 5 g/l PPO + 20 mg/l bis-MSB) and Samarium loaded LAB (+ 5 g/l PPO + 20 mg/l bis-MSB + 2% ^{nat}Sm), at three temperatures each. Dashed lines mark the position of the emission maxima, refer to Fig. 5.3.2.

Not only does this help to understand the energy spectra, but also does it give a lot of information about the capabilities of the setup. Furthermore, comparison with other experiments is only possible on a well defined 'universal' scale, in this case the electron equivalent energy. This section shall describe the measurements and analysis of the energy calibration with the different LAB mixtures of interest.

The results of calibration measurements at different temperatures, making use of the principles described here, will be shown in the next section (sec. 5.5).

As the internal contaminations of any alpha- or beta isotopes is not known for this new detector, the natural choice for calibration sources is gamma-ray emitting isotopes. In contrast to alpha- and beta radiation, gamma-rays with energies greater than ≈ 200 keV easily penetrate the ~ 2 cm thick aluminium walls of the detector, without problematic attenuation. A disadvantage of these standard calibration sources is the fact that the dominant interaction mode in liquid scintillator at these energies is Compton scattering. Due to the very low average atomic number in LAB ($\langle Z_{LAB} \rangle \approx 2.9$), the interaction cross-section for Compton scattering is much larger than for the photoeffect. This is illustrated in Fig. 5.4.1, showing the cross-sections vs. energy of 0.001 – 10 MeV gamma-rays with Carbon. It is clearly visible that the incoherent scattering is several orders of magnitude stronger expressed than the photoelectric effect, which would lead to full energy deposition in the liquid scintillator.

One option to still obtain the energy resolution and calibration would be a Compton scatter experiment in which another detector would be placed under a well defined angle (e.g. by collimation) to only detect Compton-scattered gamma-rays under this angle, in coincidence with the actual liquid scintillator detector. As

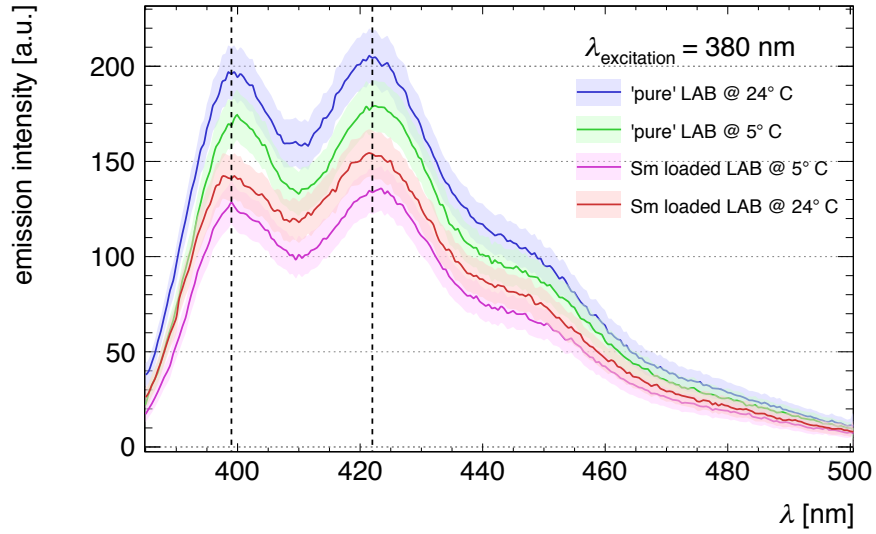


Figure 5.3.2: Fluorescence spectra of 'pure' LAB (+ 5 g/l PPO + 20 mg/l bis-MSB) and Samarium loaded LAB (+ 5 g/l PPO + 20 mg/l bis-MSB + 2 % ^{nat}Sm), at two temperatures each. The shaded areas mark the 1σ statistical uncertainties. The dashed lines only emphasise the emission maxima.

this approach requires an additional detector with good timing, energy resolution and detection efficiency, and more infrastructure, another option was chosen.

In this work, the energy resolution and calibration was obtained by fitting the upper edge of the Compton continuum in the charge spectra. The graphical representation of the following description can be found in Fig. 5.4.4. Also, the broad range of gamma-ray emitting isotopes used in this work is summarised in Tab. 5.4.1.

Firstly, the ideal Compton spectrum needs to be calculated for the individual isotope energies, making use of the analytic cross-section calculation by Klein and Nishina [Kle29]. Accordingly, the energy transferred to the electron is:

$$E'_e = E_\gamma \times (1 - P(E_\gamma, \Theta)) \quad (5.4)$$

with E'_e as electron energy, E_γ the incident gamma energy, Θ the scattering angle, and $P(E_\gamma, \Theta)$ as the ratio of photon energy after and before the collision:

$$P(E_\gamma, \Theta) = \frac{1}{1 + (E_\gamma/m_e c^2)(1 - \cos \Theta)} \quad (5.5)$$

The upper edge is then defined by scattering under 180° , as this marks the maximum photon energy transfer to the electron:

$$E'_e(\Theta = 180^\circ) = \frac{2E_\gamma^2}{m_e c^2 + 2E_\gamma} \quad (5.6)$$

The gamma-ray energies used during this calibration are all well above 400 keV, thus a correction factor for the cross-section, as calculated by Grodstein [Gro57], is neglected. This ideal spectrum is generated for each individual gamma-line, and those

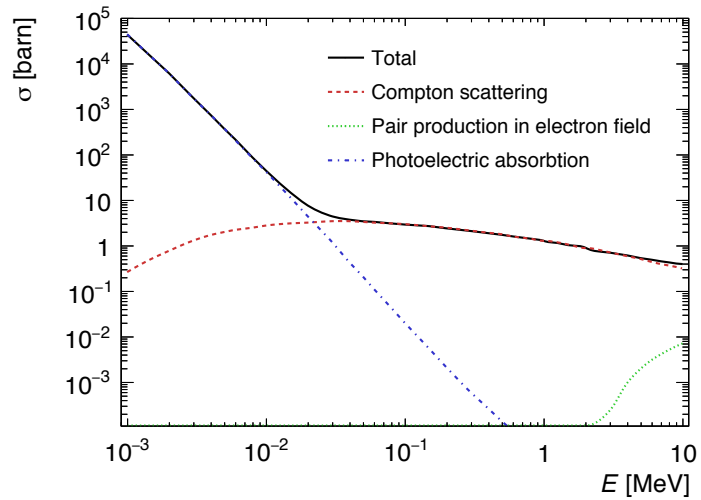


Figure 5.4.1: Cross-sections for photon interaction with Carbon. Generated with data from [Web].

are then combined into a sum-spectrum with the exact branching ratios for the individual decays (see solid black line spectra in Fig. 5.4.4).

Table 5.4.1: List of gamma-ray isotopes used for calibration in this work. The grey coloured lines were not included in the final analysis, since they are either too low or too close in energy.

isotope	branching ratio [%]	Compton energy [keV]	full γ -energy [keV]
^{137}Cs	85.1	477	662
^{22}Na	200	341	511
^{22}Na	99.94	1062	1275
^{60}Co	99.97	963	1173
^{60}Co	99.98	1118	1332
^{207}Bi	97.74	393	570
^{207}Bi	74.5	858	1064
^{207}Bi	6.87	1546	1770
^{88}Y	93.7	699	898
^{88}Y	99.2	1612	1836

Secondly, the physically sharp Compton edge is ‘smeared’ by the energy resolution of the detector. This needs to be taken into account when calculating / simulating the Compton spectrum, and can be used to determine the energy resolution. In order to achieve such a convolution with a finite energy resolution, every bin entry in the ideal spectrum is multiplied by a factor randomly chosen from a normalised gaussian function centred at the bin position. The ideal spectra convoluted with an energy resolution are drawn with solid red lines in Fig. 5.4.4.

For every gamma-line, the Compton edge needs to be fitted locally, since the energy resolution is energy dependent itself. From each edge-fit the position and energy resolution can be extracted. A fit to the upper and middle Compton edge of a ^{88}Y calibration spectrum are shown in the top and middle histogram in Fig. 5.4.4,

respectively. After a first, rough 'by hand' approximation, the extracted parameters for the position and resolution are used to start a full likelihood fit, using the Minuit routines of the CERN root software packages. The energy calibration and energy depending energy resolution obtained from these fits are shown in Fig. 5.4.2 and 5.4.3, respectively. While a linear fit is used to determine the parameters for the calibration function, the energy resolution can be described with:

$$\frac{\Delta E}{E} = \sqrt{\frac{p_1}{E^2} + \frac{p_2}{E} + p_3} \quad (5.7)$$

with p_1 as parameter to describe the finite resolution due to electronic noise, p_2 regarding statistical effects of photon and photo-electron generation and p_3 the influence of the position of the light generation and attenuation of the same.

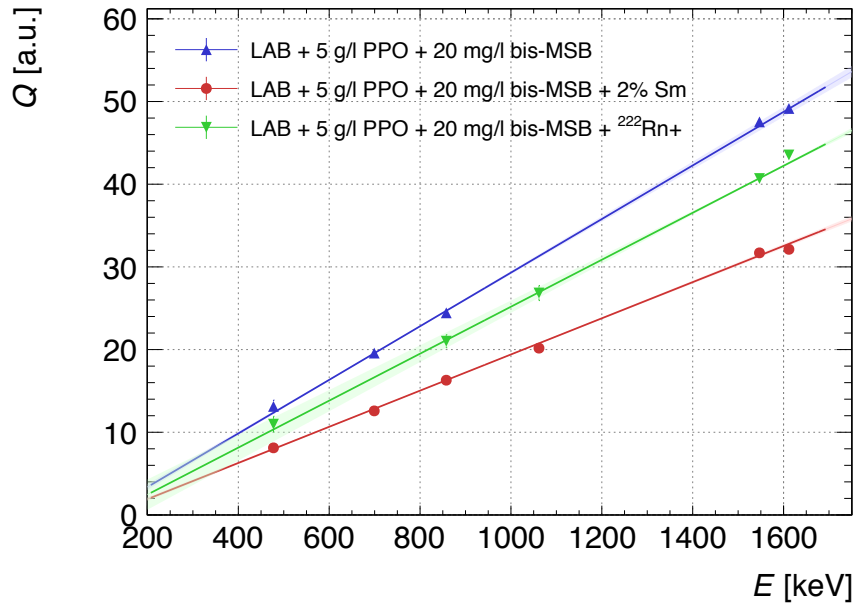


Figure 5.4.2: Energy calibration for three mixtures: 'pure' LAB + PPO + bis-MSB (blue), Samarium loaded LAB (red) and Radon loaded LAB (green). The linear function is shown with its 1σ uncertainty band, obtained from the fit. The uncertainties on the individual data points are mostly too small to be visible.

As expected, the LAB mixture with metal loading emits much less light (see Fig. 5.4.2), or more precisely, much less light is detected, due to the worse optical properties of the scintillator. This effect is again seen in separate UV/VIS measurements (refer to section 5.3). It is also the main reason why the energy resolution is worse for Samarium loaded LAB. Another factor increasing mainly the uncertainty of the energy resolution for lower energies in this scintillator mixture, is the alpha peak from the ^{147}Sm , disturbing the Compton edge fitting.

Moreover it can be seen that the energy resolution in 'pure' scintillator mixture (LAB + 5 g/l PPO + 20 mg/l bis-MSB) is not affected when ^{222}Rn is added to the

liquid only by diffusion, see green and blue data in Fig. 5.4.3. Details of the loading process will be discussed in sec. 5.8. The reason why the green data points are below the blue ones in Fig. 5.4.2 is the fact that for the Radon loaded LAB measurement a lower high voltage on the PMTs had to be used, since they were different PMTs (though same type) and the activity of the Radon was quite high.

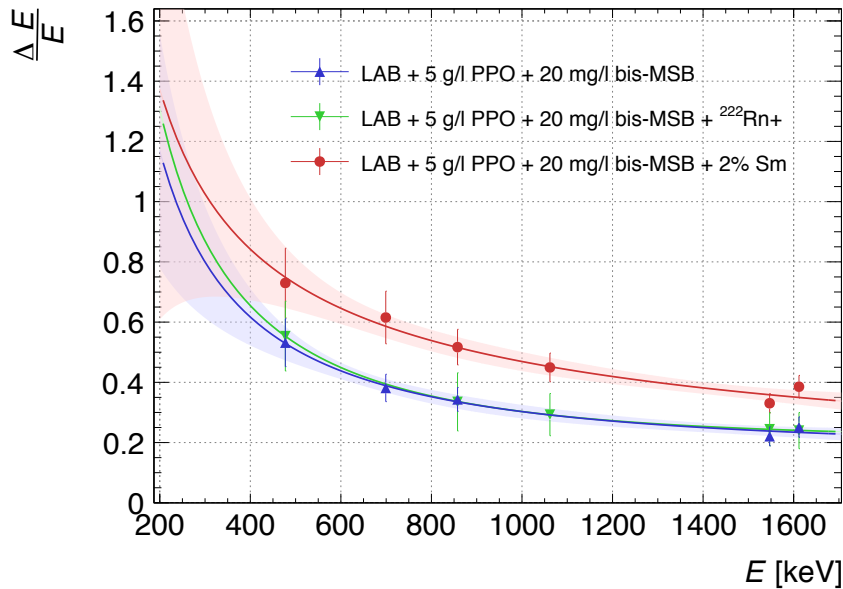


Figure 5.4.3: Energy dependent energy resolution for three mixtures: 'pure' LAB + PPO + bis-MSB (blue), Samarium loaded LAB (red) and Radon loaded LAB (green). The fit function (see Eq. 5.7) is shown with its 1σ uncertainty band, obtained from the fit.

In conclusion it was found that a good energy calibration can be obtained by fitting the Compton edge of gamma-ray calibration sources, placed outside the detector. Also, the energy dependent resolution is reasonable for this type of detector and in the expected order of magnitude.

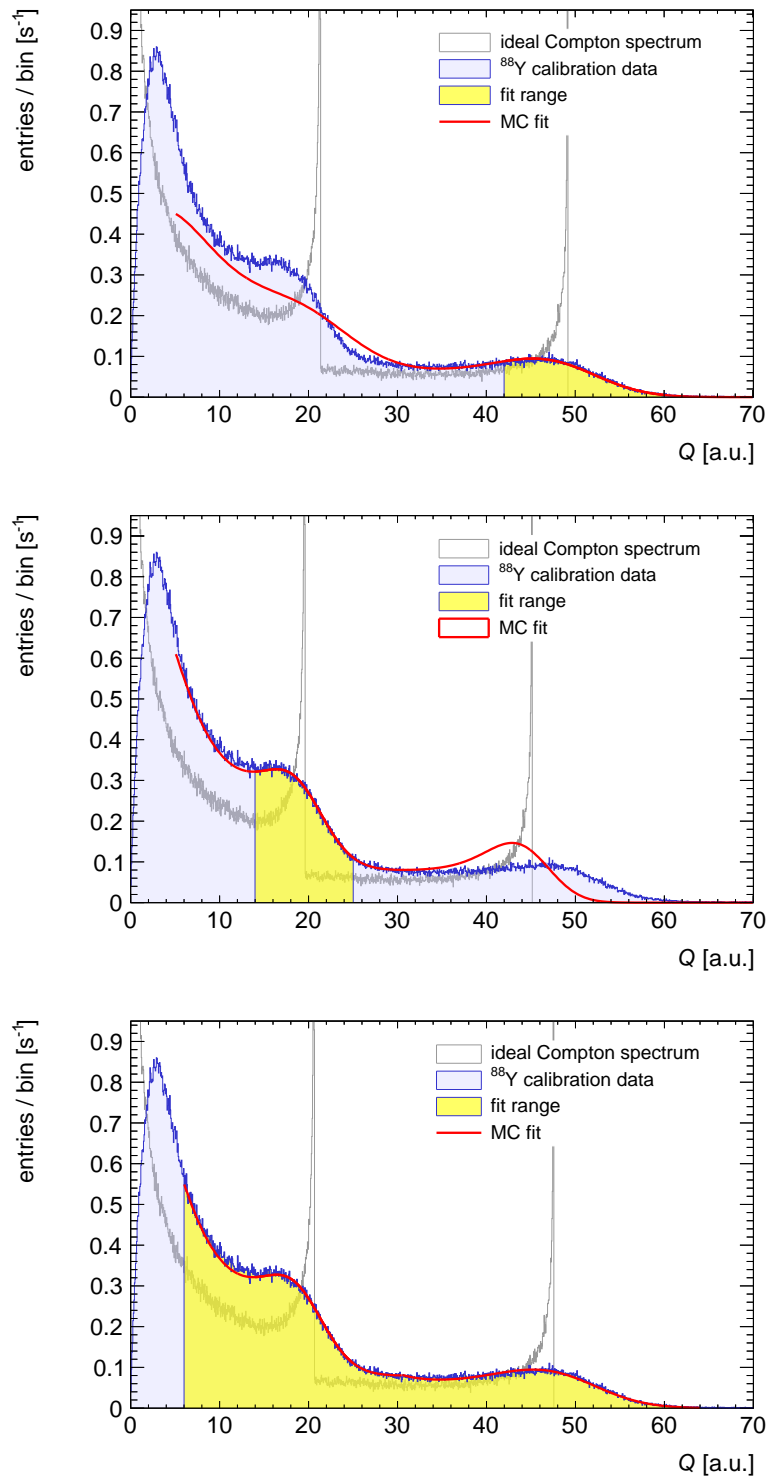


Figure 5.4.4: ^{88}Y calibration spectrum, obtained with LAB + 5 g/l PPO + 20 mg/l bis-MSB. (Top) - fit to the upper Compton edge. (Middle) - fit to the lower Compton edge. (Bottom) - fit over the full range, making use of the energy resolution function shown in 5.4.3. All three plots show in blue the actual data, in grey the ideal Compton spectrum and in red the Monte-Carlo (MC) simulated and fitted spectrum. The yellow areas mark the range of the fit.

5.5 Energy calibration at different temperatures

Since previous studies by Homma et al. [Hom85b; Hom85a; Hom87], Buontempo et al. [Buo99] and especially Xia et al. [Xia14], have shown or at least indicated that an increase in electron light yield with lower temperatures has to be expected (refer to detailed discussion in sec. 4.4), the calibration technique described in the previous section is applied at different temperatures. This is especially important to differentiate a possible difference in the temperature quenching between α -particles and electrons.

Three different gamma-ray emitting isotopes (^{22}Na , ^{207}Bi and ^{137}Cs) with four different energies were used to determine the position of their Compton edges at five temperatures. Combining the individual results for each energy, Fig. 5.5.1 shows the change in charge versus temperature. The slope of the linear fit is $-0.173 \pm 0.018 \text{ \%}/^\circ\text{C}$, indicating a change in light yield in the same order of magnitude as the results reported in [Xia14]. Unfortunately only diagrams with data points and splines are presented there and no linear approximation is performed. Therefore only a very rough 'by hand' estimate of $\approx -0.32 \text{ \%}/^\circ\text{C}$ can be used for comparison with the data obtained in this work. For a more detailed literature discussion see section 4.4.

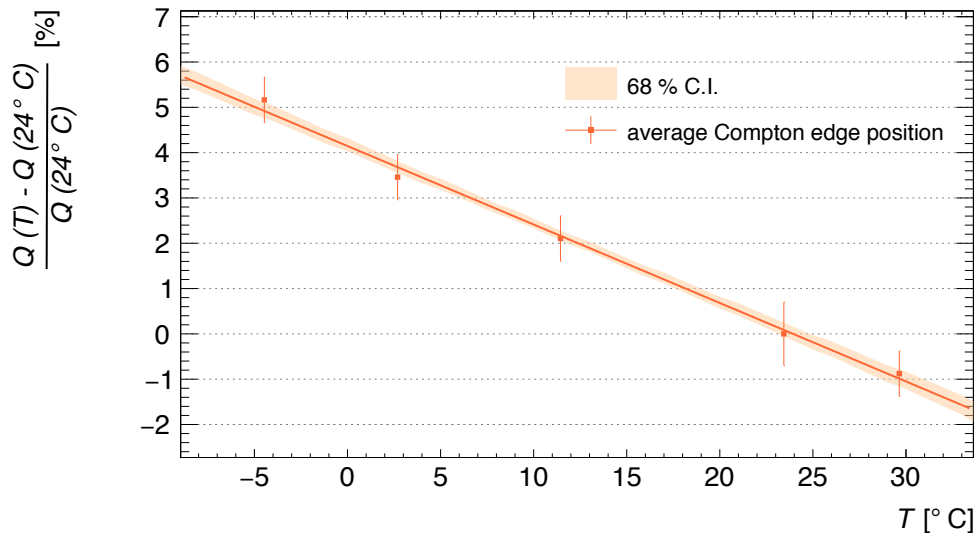


Figure 5.5.1: Charge (light yield) deviation of fitted Compton edges at five different temperatures. Each data point contains the combined data for four energies and is normalised to the room-temperature value (23.44 ± 0.04) $^\circ\text{C}$. Uncertainties consist of the variance between the values from the different energies and the fit uncertainty. The light orange band shows the 68% confidence belt, taken from the linear fit (solid orange line).

A comparison of the linear fit slopes for the individual isotopes and their energies will be presented in final discussion of all results in section 5.9.

5.6 Pure LAB background spectrum

In order to be able to measure alpha radioactivity precisely, as intended in this work, potential background of unwanted events interfering with the actual measurement needs to be assessed. Therefore many background measurements with only LAB as solvent, 5 g/l PPO as primary-, and 20 mg/l bis-MSB as secondary fluor, were carried out. Even though there is no calibration source or any other known radioactive source present during the measurement, the event rate for these measurements is ≈ 40 Hz as the integral over the whole energy spectrum. This already indicates that there is some activity inside the pure LAB mixture and/or the vessel, contaminating the detector to some extent.

The main reason why these very low activities are even visible in such a small detector, is the very high detection efficiency, especially for low energetic radiation of all kinds. Nearly everything dissolved in the liquid scintillator is detected, as long as enough light is generated to pass the detection threshold. Which is of course also true for everything in direct contact with the LAB mixture, such as O-rings, the inside of the aluminium cuvette or the quartz glass windows. These materials themselves are very low radioactive or contain radioactive contaminations from the environment. Even though the detection efficiency is very high, the low energy resolution at small energies makes it difficult to exactly identify background sources, as will be shown here. Figure 5.6.1 shows an overview over the full energy spectrum from the 'pure' LAB mixture, obtained in a 22 h background measurement.

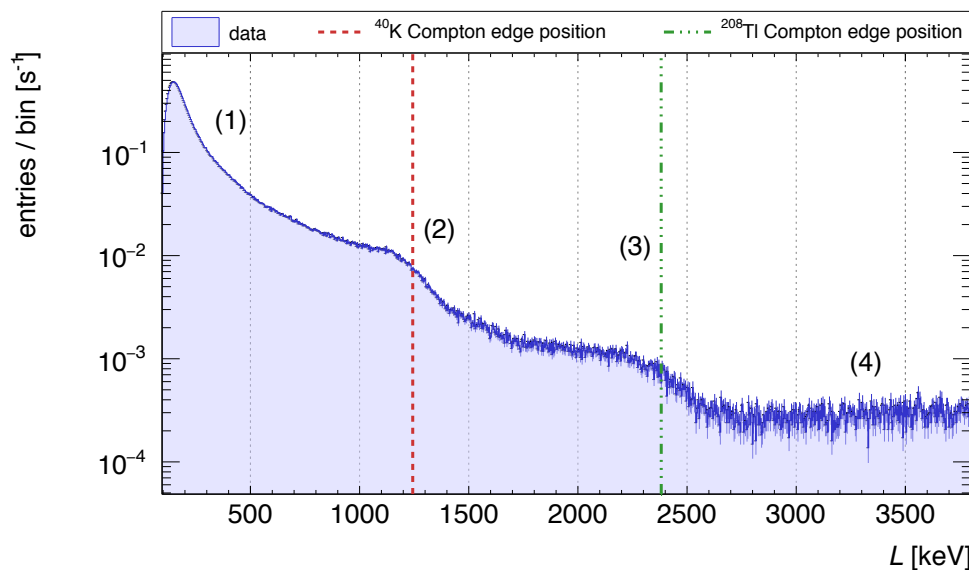


Figure 5.6.1: Full background spectrum for LAB + 5 g/l PPO + 20 mg/l bis-MSB. Obtained in a 22 h measurement. Features: (1) - various low energy backgrounds, (2) - Compton edge position of ^{40}K , (3) - Compton edge position of ^{208}Tl , (4) - likely cosmic ray muons. For a detailed explanation, refer to the text description.

The four prominent features are likely identified as the following:

- (1) **Various low energy backgrounds** that are very difficult to identify exactly. These include low energy alpha-, beta- and gamma-emitting contaminations of the setup, as well as gamma-ray and neutron backgrounds from the environment. Single contributions can not be identified here, since the energy resolution is very poor in this region and overall activity is too low to produce clear features.
- (2) ^{40}K Compton edge position for a possible potassium contamination of the detector and/or liquid scintillator. Since potassium is a very common human contamination in low background experiments, it is very likely that this was introduced during assembly of the detector or mixture of the liquid scintillator. A Compton edge fit was attempted but did not prove to be useful since the edge (if it is the Compton edge of ^{40}K) is only very weakly pronounced (note the logarithmic scale in Fig. 5.6.1).
- (3) ^{208}Tl Compton edge position for a possible environmental thallium contamination of the aluminium body of the detector or the PMTs. The same argument (as for (2)) for not fitting the edge applies here.
- (4) **Cosmic ray muons** seem to be the most likely explanation for these high energy events in the detector. This has been seen constantly in all measurements with all liquid scintillator mixtures, and scales linear with measuring time. The very high energy already excludes natural occurring gamma lines and disfavours also many alpha and beta isotopes. These events extend up to ~ 10 MeV, where they also mark the end of the energy spectrum, no events have been observed above this energy. Since cosmic ray muons deposit about 2 MeV/cm in liquid scintillator (see sec. 6.1), the observed energy distribution seems reasonable. The integral from 3 MeV to 10 MeV yields an event rate of 0.49 Hz. Taking the integral muon intensity on the earths surface of $70 \text{ m}^{-2}\text{s}^{-1}\text{sr}^{-1}$, for muons above 1 GeV, the approximate value for a horizontal detector is $\approx 1 \text{ cm}^{-2}\text{min}^{-1}$ [Pas93; Gri01]. With the slice plane area of $(4 \times 9) \text{ cm}^2$, the figure of merit is 0.5 Hz of muon events in this detector, which is surprisingly close to the observation. Since the average energy deposition is high, distributed over a wide range in the energy spectrum and the event rate is very low, the installation of an external muon veto was not necessary.

All these features in the background spectrum show activities that are not threatening to the following α -particle measurements, which are providing at least one order of magnitude more activity. An exact fit to the shapes (2) and (3) has been attempted but did not yield useful results, since these are extremely flat. Nevertheless seems their position to coincide well with the position of the well known and common contaminations of ^{40}K and ^{208}Tl .

Taking all the previously in this chapter presented measurements and tests into account, one can conclude that this detector is well suited to perform relative light yield measurements of α -particles and electrons in LAB based liquid scintillators, at different temperatures. These will be presented in the following sections.

5.7 Samarium loaded LAB measurements

The BNL has been able to load natural Samarium into LAB based liquid scintillators, using the surfactant TMHA in a single-stage solvent-solvent extraction procedure, which can be used to form stable compounds of inorganic elements (metals) and an organic liquid. This technique was initially developed to load Neodymium into liquid scintillator, but was in this case used to study α -Quenching in LAB in general.

Natural Samarium contains 15.01(3) % of the isotope ^{147}Sm , which is α -instable and decays with a half-life of $T_{1/2} = 1.070(9) \times 10^{11}$ y and a Q-Value of 2.233 MeV [Kos09]. The mixture used for the measurements in this work contained about 2 % natural Samarium, resulting in a 'constant' activity of about 200 Bq in the 100 ml volume of the detector used, from this decay. Although natural Samarium also contains 11.24 % of the α -instable isotope ^{148}Sm , its half-life of $T_{1/2} = 7 \times 10^{15}$ y [Tab99] is four orders of magnitude larger, resulting in a negligible activity of $\approx 2 \times 10^{-3}$ Bq.

One fundamental difference between Samarium loaded and 'pure' LAB (+ 5 g/l PPO + 20 mg/l bis-MSB), is the increased density and worse optical properties of the metal loaded scintillator. The density can be calculated to be 0.99 g/cm^3 , using an LAB density of 0.86 g/cm^3 [Pet09] and a Samarium density of 7.54 g/cm^3 [Gre88], though the here given calculated value has not been measured yet. As worse optical properties, such as shortened scattering length and different absorption features, are well known for other metal loaded liquid scintillators, the UV/VIS measurements in section 5.3 (see Fig. 5.3.1) and energy calibration measurements in section 5.4 show the same effects for Samarium loaded LAB. All of this results in less detected light from this LAB mixture and therefore significantly less energy resolution. This makes it difficult to directly compare the unloaded LAB spectrum with the Samarium loaded one.

5.7.1 Spectral analysis

Despite the mentioned disadvantages, measurements of the temperature behaviour of the α -peak could be performed. Figure 5.7.1 shows a calibrated spectrum in electron equivalent energy at room temperature. A natural first choice for a fit function was a Gaussian, though as the samarium peak showed some kind of unidentified high energy tail, other shapes were tried too. As a Landau distribution did not fit well, a skewed normal distribution was tried as well but only improved the goodness of fit to a minor degree. Thereafter the more or less model independent gaussian shape was revisited. This seemed to be the most conservative choice, especially as no physics motivation for any other shape was found. The overall activity in the setup was too low for pile-up events, and for ^{147}Sm no database entry of any x-ray emission was found.

Therefore for all $^{\text{nat}}\text{Sm}$ -LAB temperatures the following fit routine was applied: First a simple gaussian fit with a wide range is performed, to roughly identify the peak position and width. In second step the fit range is confined to 1σ around the mean of the first fit. The second (actual) fit is in this case restricted to 1σ to avoid any distortion due to the high energy tail. This is incorporated in the final analysis

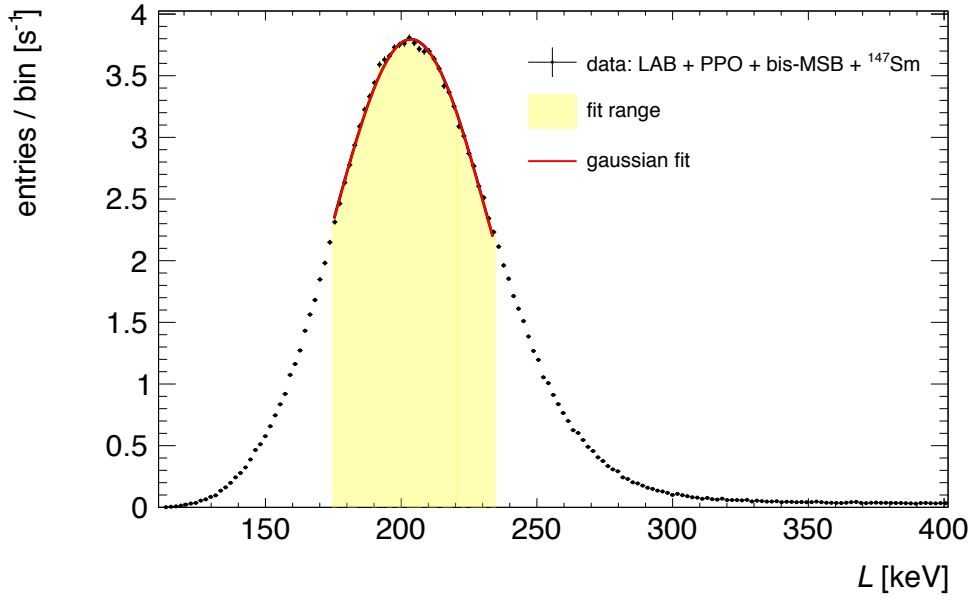


Figure 5.7.1: Light yield spectrum at room-temperature (24.62 ± 0.04 °C) of LAB + 5 g/l PPO + 20 mg/l bis-MSB + 2% ^{147}Sm . The yellow shaded area marks the 1σ fit range for the gaussian fit.

and evaluation with a **fit range uncertainty**, which is calculated as the variance of the fit mean values of gaussian approximations with 1σ , 2σ and 3σ fit range. For the room-temperature measurements a list of the individual uncertainties considered is given in Table 5.7.1.

Table 5.7.1: List of uncertainties considered in the analysis of the ^{147}Sm -loaded LAB mixture at room-temperature (24.62 ± 0.04 °C).

uncertainty	value [%]
fit	0.08
fit range	0.47
pulser stability	0.35
variance between rep. measurements	0.2
sum	1.1

In a previous work at Technische Universität Dresden (TUD) and HZDR, Krosigk et al. used this mixture in a smaller, different detector setup, and found the light yield from ^{147}Sm to be $L = 0.157 \pm 0.032$ MeV, corresponding to a quenching by a factor of 14.2 ± 2.9 , compared to electrons [Kro16]. This study found a light yield at room-temperature of $L = 0.204 \pm 0.014$ MeV, resulting in a quenching by a factor 10.9 ± 1.0 , with the by far largest uncertainty originating from the energy calibration (see Table 5.7.1). As this seems to be also the case for the first result, the smaller uncertainty in this work can be attributed to a smaller uncertainty in the energy

calibration. The measured value is in a small tension to the result obtained by Krosigk et al. ($\sim 1\sigma$). As the accuracy on the electron equivalent energy scale is not crucial for the relative measurements with varying temperature, this small discrepancy is not important for the conclusion of the temperature behaviour studies.

All temperature varied measurements have been performed at least twice, except the one for 30°C , due to an unfortunate data loss, so that only the data for one measurement is available. The sequence of the measurement was chosen for practical reason to $24^\circ\text{C} \rightarrow 5^\circ\text{C} \rightarrow 14^\circ\text{C} \rightarrow 24^\circ\text{C} \rightarrow -4^\circ\text{C} \rightarrow 24^\circ\text{C} \rightarrow 30^\circ\text{C}$ and then repeated without the two 24°C steps in between. As this does not allow to check for any systematic effects of the T changes in the detector system, such as some kind of hysteresis, a more systematic approach for the temperature sequence was chosen in the Radon loaded LAB studies, presented in the next section, 5.8.

As room-temperature seems to be a natural scale for liquid scintillator measurements, all changes observed with temperature are being normalised to the room-temperature value. Figure 5.7.2 gives an impression of how the temperature change affects the ^{147}Sm peak position, after the PMT sensitivity correction is applied, to correct for any ambient temperature effects on the PMTs.

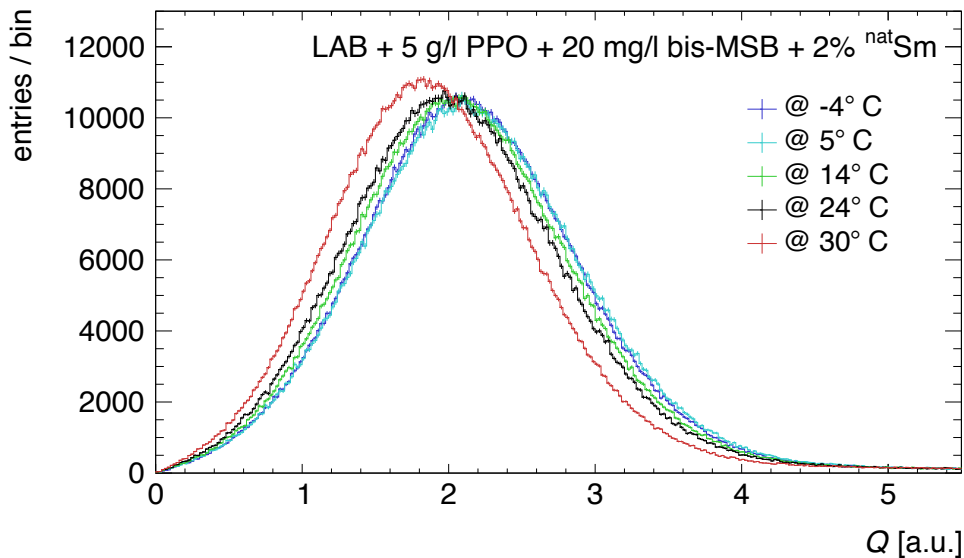


Figure 5.7.2: Comparison of ^{147}Sm loaded LAB charge spectra at different temperatures, with the PMT sensitivity correction already applied.

In Figure 5.7.2 the systematic shift towards a higher light yield with decreasing temperature is clearly visible. The data for the 30°C measurement seems to be shifted disproportionately towards lower charge values. The visual effect is increased by the odd observation that the peak is also narrower. Also in the final analysis of the peak shift, the 30°C data seems to deviate of the seemingly linear trend of the other data points, see Fig 5.7.3.

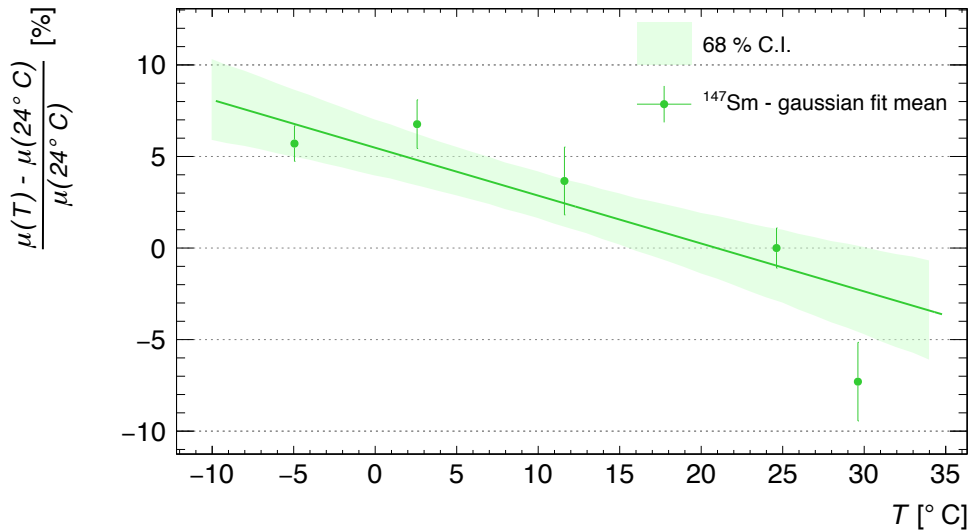


Figure 5.7.3: Shift of the gaussian fit mean values versus liquid scintillator temperature, for the ^{nat}Sm loaded LAB measurements. Each data point contains the combined values for the repeated measurements and is normalisation to the room-temperature value, $(24.62 \pm 0.04)^\circ\text{C}$. The green shaded area marks the 1σ confidence band obtained from the linear fit.

5.7.2 Pulse shape analysis

Since the Acquiris FADC is able to take a voltage sample from the PMTs every 0.5 ns, it is possible to perform pulse shape analysis (PSA) with this experimental setup. As the variations between individual pulse shapes are very large (due to wide energy spectrum etc.), averaged pulses will be used for comparisons and fits. For a given pulse ensemble, at each sample point, the arithmetic average of the voltage values is calculated, as well as the variance between these pulses. With a typical size of one million pulses, the uncertainty (variances) are very small, and mostly not visible in the following graphs.

Figure 5.7.4 shows a comparison of averaged pulse shapes from the ^{147}Sm α -peak, at different temperatures. At all temperatures the pulses show the typical, very fast rise to the maximum, a slower falling slope, followed by an even less steep slope. Already discussed in the previous chapter, usually these different slopes are attributed to a fast and slow decay component. The slight kink visible at ≈ 123 ns might be attributed to this change in decay constants. Although it can be demonstrated that it is not originating from any PMT effects (see PMT pulse shapes in section 5.2 and Fig. 5.2.8), these deviations from a perfectly smooth curve can not be fully explained.

It is clearly visible that the shapes change between 115 ns and 140 ns. With lower temperatures, the falling slope of the pulses becomes less steep. In contrast, the rising edge is the same for all temperatures. A full discussion of this phenomenon is done at the end of this chapter, taking into account also the measurements at different α -energies and electron data. Although it can already be noted that the

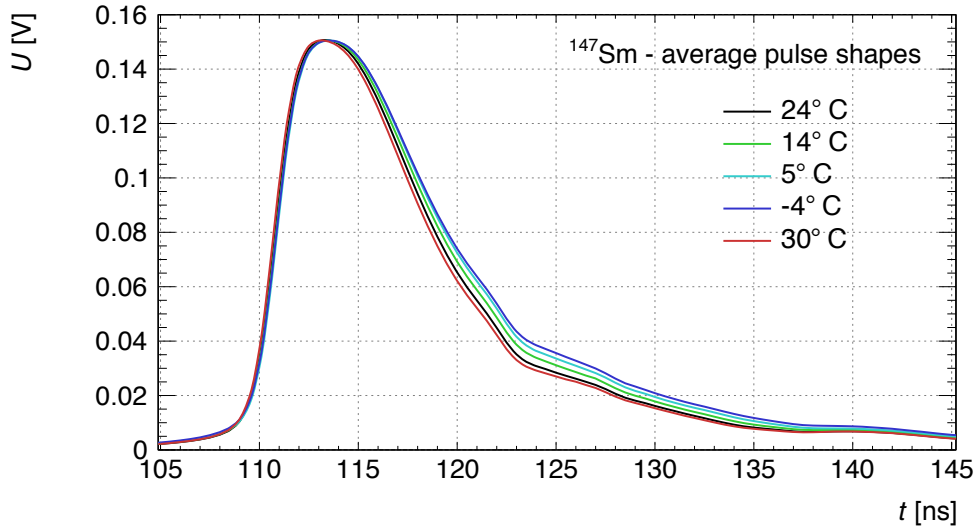


Figure 5.7.4: Average pulse shapes from ^{147}Sm α -peak, acquired at different temperatures. Each line is calculated from ~ 1 M pulses, and normalised to the height of the room-temperature shape.

prolonged pulses seem to be a likely explanation for the observed increased light yield in Fig. 5.7.3.

In order to quantify the changes in the slopes, the following composition of two exponential functions was chosen and fitted to the average pulse shapes, inspired by equation 4.1 in chapter 4:

$$U(t) = e^{c_1 - t/\tau_{fast}} + e^{c_2 - t/\tau_{slow}} \quad (5.8)$$

with U - voltage, t - time, τ_1, τ_2 - decay constants and c_1, c_2 - position parameters. It was found that a two component exponential function fitted the data best, all attempts with a third component lead to fits with a vanishing third part. Also the rising edge was not included here, since it is the same for all temperatures. Once c_1 and c_2 are fixed to their fit value at room-temperature, the approximations for the other temperatures reveal the change in the decay constants. These are at room-temperature $\tau_{fast} = (4.48 \pm 0.01)$ ns and $\tau_{slow} = (16.90 \pm 0.01)$ ns for the fast and slow component respectively. The changes that these constants undergo is illustrated in Figure 5.7.6. It is quite clear that the second, slow component is stronger expressed with lower temperatures. While the very small change in the fast component fits very well do a linear fit, the change in τ_{slow} might be even better represented by a non-linear approximation. Again the full implications from these findings will be discussed in broader scope in section 5.9.

5.8 Radon loaded LAB measurements

In the previous sections it could be seen that the light yield of LAB based liquid scintillator, that is loaded via a surfactant with 2% natural Samarium, showed some

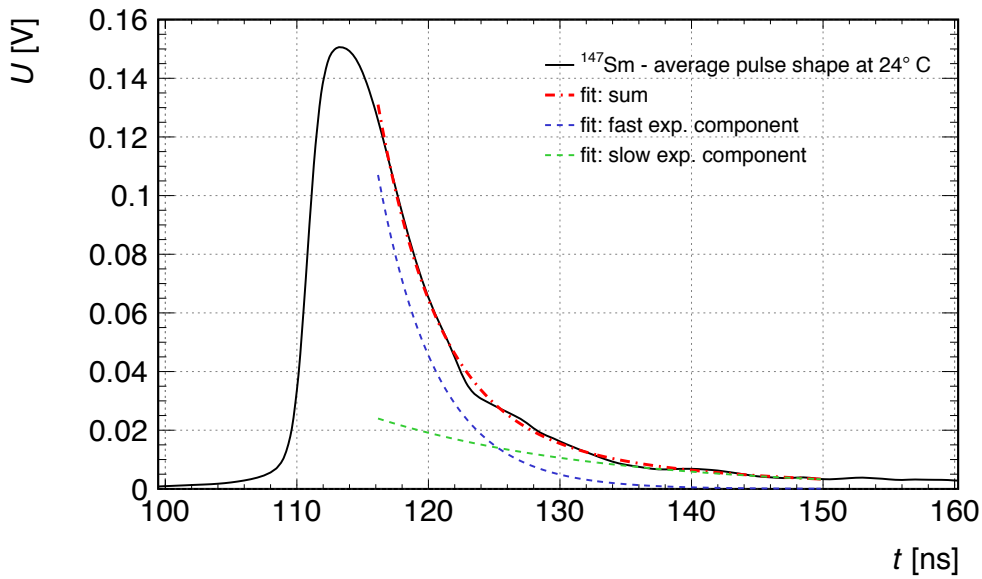


Figure 5.7.5: Exponential fit to average pulse shapes from ^{147}Sm α -peak, acquired at $(24.62 \pm 0.04)^\circ\text{C}$. The red dashed line shows the actual fit function, whereas the blue and green dotted lines depict the fast and slow exponential component, respectively.

seemingly systematic temperature dependence, which is also expressed in a change of the decay constants in the pulse shapes. To some extent, this behaviour is also observed in electron spectra, generated by gamma-ray sources, at different energies.

To extend the investigations further, it was chosen to try another approach into 'loading' the liquid scintillator with α -emitting isotopes, preferably at higher energies. This would shed light into several things. Firstly, if the observation and amount of the light yield change is the same for other alpha isotopes. Secondly, making use of a different technique in introducing the α -isotopes into the LAB, could clarify if there is an influence of the surfactant loading technique. And thirdly, extending the energy range helps identifying any energy dependence.

To avoid using another chemical binding technique, introducing the isotope simply via diffusion is sensible. Taking advantage of the broad range of radioactive isotope samples at the Institut für Kern- und Teilchenphysik (IKTP), a ^{226}Ra source with an activity of ~ 10 MBq proved suitable for the use of the subsequent ^{222}Rn decay chain.

^{226}Ra is an 100% α -emitting isotope with a half-life of $T_{1/2} = 1600$ y, decaying solely to ^{222}Rn . As Radon is a gas, the isotope escapes the porous ceramic Radium source and can be transferred via gas exchange. This Radon gas is used in a nitrogen atmosphere to 'bubble' through a LAB mixture. For better comparison, the same 'pure' LAB + 5 g/l PPO + 20 mg/l bis-MSB (without Samarium) solution was used. The setup to 'activate' the liquid scintillator with the Radon gas from the Radium source is depicted in the scheme in Fig. 5.8.1.

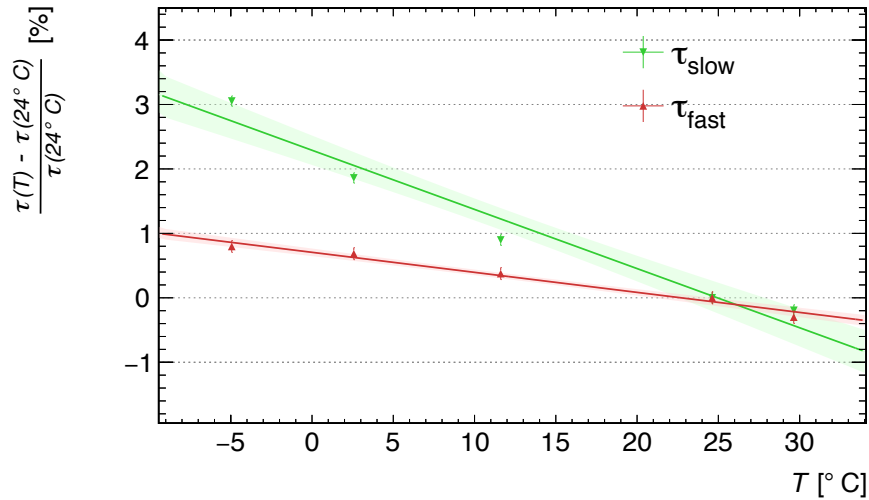


Figure 5.7.6: Change of the decay constant fit values of averaged pulse shapes from ^{147}Sm at different temperatures. The shaded areas show the 68 % confidence band of the linear fit.

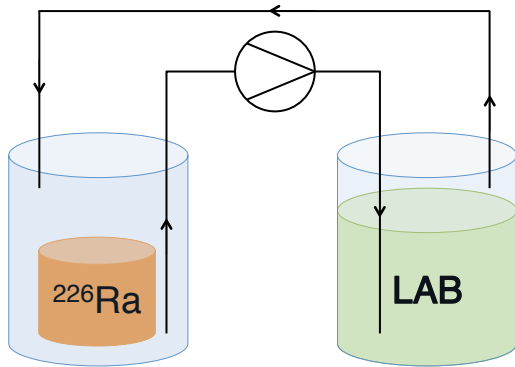


Figure 5.8.1: Schematic drawing of the Radon gas circulation setup. On the left, in orange, the porous Radium ceramic, emitting ^{222}Rn gas into the N_2 atmosphere that is present in the whole circuit. A peristaltic pump that is squeezing a silicone hose, is moving the atmosphere in this closed circuit. On the right side, a gas-washing bottle ensures an even spread of the gas bubbles.

After circulating the Nitrogen - Radon atmosphere for about 72 hours, an activity of about 200 kBq was introduced into the LAB mixture. This high activity was far beyond any expectation and the setup had to rest for several weeks to reduce the activity to about 1 kBq. Otherwise the large amount of light produced would have damaged the PMTs on full high voltage.

The ^{222}Rn starts a decay chain that ends at the stable ^{206}Pb . For the purpose of this work, already the isotope ^{210}Pb presents the end of the chain with an half-life of $T_{1/2} = 22.2$ y, which leads to an activity too small to be visible in this detector, in the scope of the used measuring times. This short chain produces three α -particles and has two β^- -decays, this is illustrated in detail in the diagram in Fig. 5.8.2. The first α -decay of ^{222}Rn has the longest half-life of $T_{1/2} = 22.2$ y. As the other isotopes decay with minutes and micro-seconds, the chain is very fast at secular equilibrium. The first α -energy of 5.49 MeV is close to the one from the following ^{218}Po (6.00 MeV) and can therefore not be distinguished with this detector setup. Nevertheless, in a combined fit, it will be possible to extract the individual light yields. The resulting

^{214}Pb decays via β^- -emission to ^{214}Bi , with an end-point energy of 1.0 MeV. Subsequently ^{214}Bi changes to ^{214}Po , emitting an electron with the maximum energy of 3.3 MeV. Its very short half-life of $T_{1/2} = 164.3 \mu\text{s}$ proves useful for tagging this and the following α -decay to the final ^{210}Pb . This last α -decay has an energy of 7.69 MeV, which separates it nicely from the preceding alphas. All decays have branching ratio of at least 99.98 %, [Tab99].

This LAB mixture with dissolved Radon was used to observe any light output changes at five temperatures, in the following sequence: $24^\circ\text{C} \rightarrow 10^\circ\text{C} \rightarrow 5^\circ\text{C} \rightarrow -4^\circ\text{C} \rightarrow 5^\circ\text{C} \rightarrow 10^\circ\text{C} \rightarrow 30^\circ\text{C} \rightarrow 24^\circ\text{C} \rightarrow 10^\circ\text{C} \rightarrow 5^\circ\text{C}$. No systematic effect has been observed, repeated measurements continued to scatter around their mean randomly, without a preference for a sign.

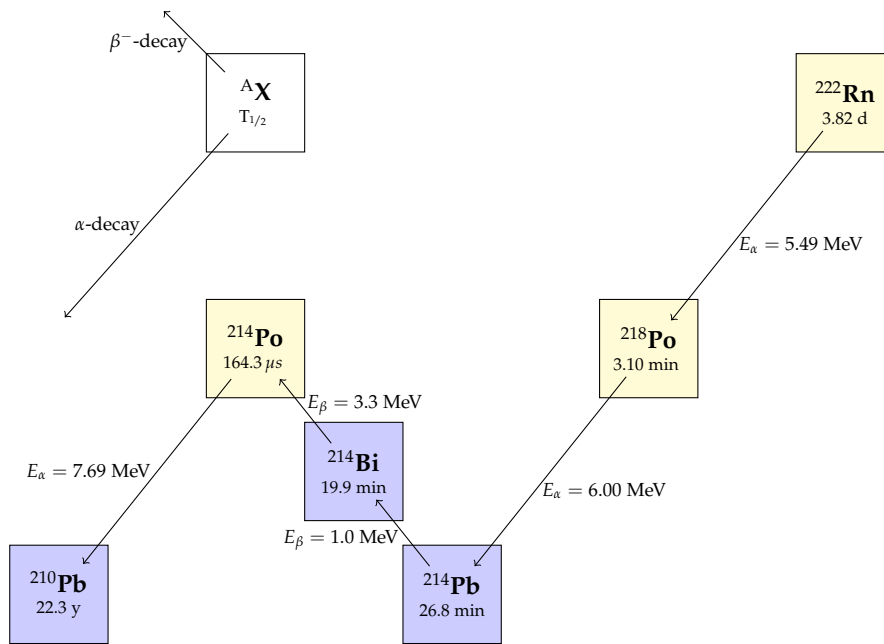


Figure 5.8.2: Scheme of a part of the ^{222}Rn decay chain. Legend in the upper left. All decays have a branching ratio of at least 99.98 %.

5.8.1 Spectral analysis I - no energy or time cuts

The charge spectrum shows the expected features and can be calibrated in the same way as it has been done for pure and Samarium loaded LAB. Although in this case, the energy calibration was performed after the Radon activity fell below $\approx 20 \text{ Bq}$, after the measurements with temperature variation had been done.

A calibrated light yield spectrum is shown in Fig. 5.8.3. Since another Radon decay chain spectrum has already been evaluated by Krosigk et al. [Kro16], in a first step a similar fit was chosen. Krosigk et al. analysed a 1 l LAB + 2 g/l PPO sample that was placed inside the water-filled SNO detector in 2008. The liquid scintillator was also ‘contaminated’ with dissolved Radon gas and the energy spectrum

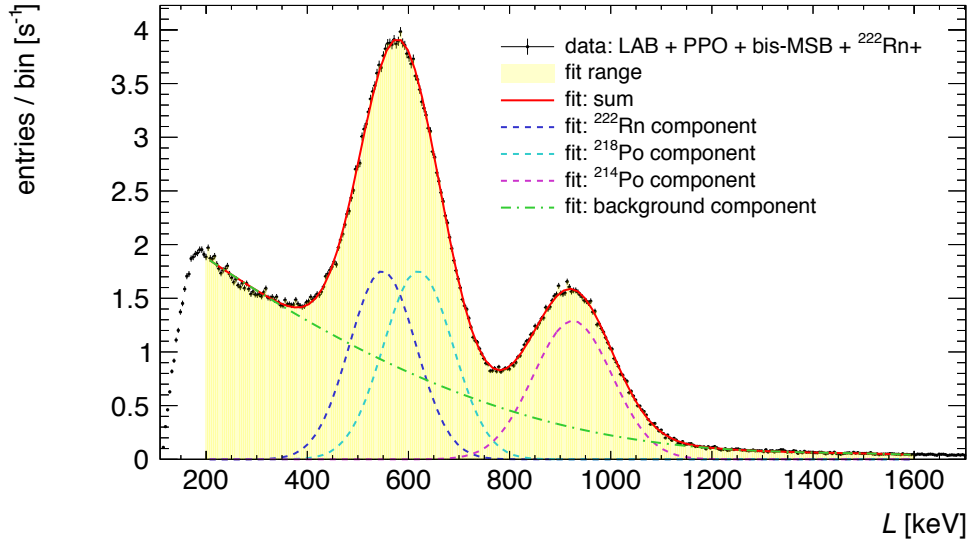


Figure 5.8.3: Calibrated light output of Radon loaded LAB (+ 5 g/l PPO + 20 mg/l bis-MSB) at room-temperature. The fit function (red line) is the sum of three gaussian functions (dashed blue, cyan and pink lines) and a 6th order polynomial (dashed green line).

shows very similar features as are visible in Fig. 5.8.3 (see Fig. 10 in [Kro16]). The background is mainly consisting of the two β -decays, was approximated with a 6th order polynomial and then subtracted. Krosigk et al. excluded the α -peak region from their background fit, in a seemingly arbitrary range. This is neglecting the tails from the α -decays, that are quite wide in a detector with this energy resolution. With this over-estimated background too much is subtracted from the spectrum, imposing some kind of bias on the resulting α -spectrum.

In the analysis of this work, the α -peaks and the β -backgrounds were fitted in one combined fit, visible in Fig. 5.8.3. The fit function is the sum of three gaussian functions and a 6th order polynomial. In order for this fit to properly converge, some of the 15 parameters needed to be constrained, mainly those of the two close α -peaks. As they stem from subsequent decays with no other branches, they have the same activity. The strength parameter was therefore the same for both gaussian, yet it could float almost freely. Also the mean-parameters (μ) of the first two Gaussians are constrained, such that they can not take the same value. The μ of the first gaussian has to be in a range below their sum-gaussian peak mean and vice versa. With these rough constraints, the fits proved to be very stable and well converging throughout the analysis, also for different temperatures. The room-temperature results for the peak positions are listed in Table 5.8.1 and are well compatible with the values obtained by Krosigk et al.

When analysing the full energy spectrum with the described fit at different temperatures, changes of the individual α -peak positions can be extracted. The resulting slopes are shown in Fig. 5.8.4 and amount to $(-0.37 \pm 0.02) \text{ \%}/^\circ\text{C}$ for ^{222}Rn , $(-0.41 \pm 0.02) \text{ \%}/^\circ\text{C}$ for ^{218}Po and $(-0.35 \pm 0.02) \text{ \%}/^\circ\text{C}$ for ^{214}Po . The repeated

Table 5.8.1: Gaussian fit mean values for α -particles in the ^{222}Rn decay chain in LAB (at room-temperature). The light output is given in electron equivalent energy, after calibration. Uncertainties stem from energy calibration and the fit.

α -emitter	E_α [MeV]	L [MeV] [Kro16]	L [MeV] (this work)
^{222}Rn	5.49	0.56 ± 0.02	0.55 ± 0.02
^{218}Po	6.00	0.64 ± 0.02	0.62 ± 0.02
^{214}Po	7.69	0.92 ± 0.02	0.93 ± 0.02

temperatures vary less than 0.5°C , and for the final analysis their average has been used. Of course, also the PMT sensitivity correction is applied before analysing the spectra.

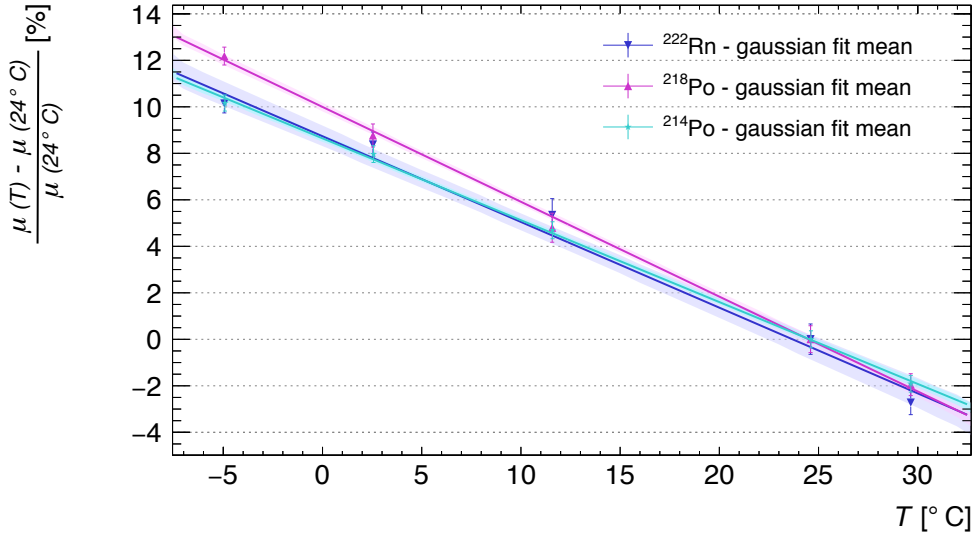


Figure 5.8.4: Shift of the α -peak mean values (from the combined fit in Fig. 5.8.3) vs. liquid scintillator temperature. Each temperature point is the average of the repeated individual measurements and these are normalised to the average room-temperature value at $(24.5 \pm 0.04)^\circ\text{C}$. The shaded areas depict the 1σ confidence band, obtained from the linear fit.

5.8.2 Spectral analysis II - application of energy and time cuts

When taking a closer look at the decay scheme in Fig. 5.8.2, the ^{214}Po decay deserves special attention with its very short half-life of $164.3\ \mu\text{s}$, compared to the other isotopes. This is an opportunity for a time coincidence analysis, which will be used as a first cut in this part of the analysis. A closer look at the times in between two events is insightful, this spectrum from one measurement is shown in Fig. 5.8.5. Theoretically, the time-difference distribution between ^{214}Bi and the subsequent ^{214}Po event should

be an exponential with a decay constant of 4219 s^{-1} . When looking for this structure in the time-difference spectrum in Fig. 5.8.5, it can be found at the left end of the spectrum in the interval $[0 \mu\text{s}, 500 \mu\text{s}]$. Events with the less steep slope in centre belong to the other decays with smaller decay constants and therefore longer half-lives.

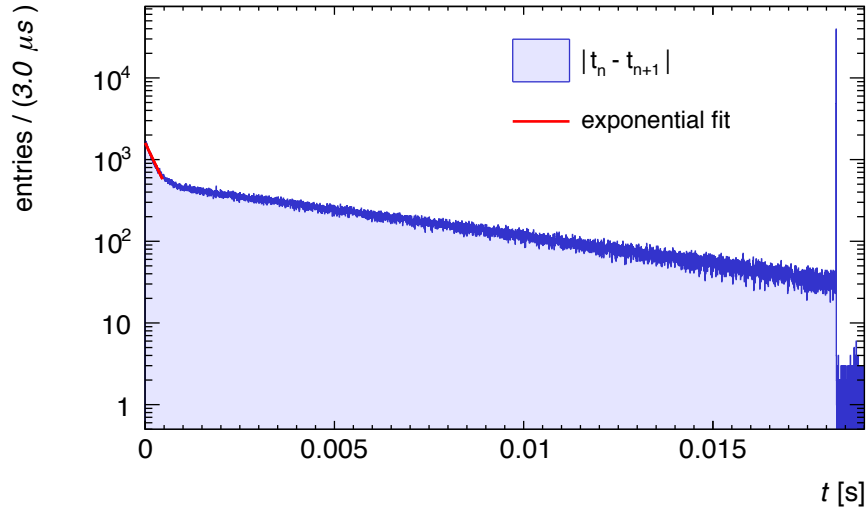
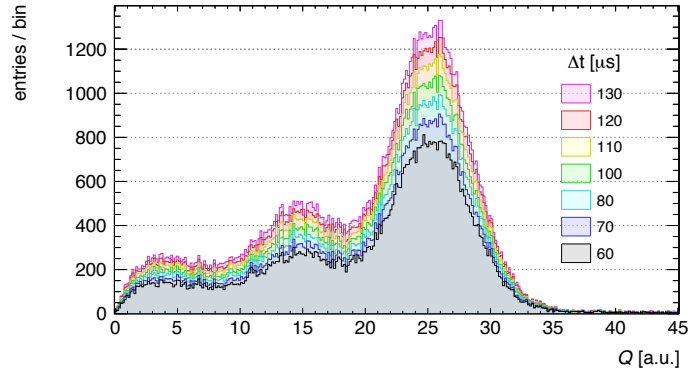


Figure 5.8.5: Spectrum of time difference between two events in Radon-loaded LAB. The peak at 18 ms is caused by the LED pulser, marking the longest possible time difference. Events right of this structure are just possible due to the finite dead-time of the FADC. The change in the slope at the very left side is due to the ^{214}Bi - ^{214}Po coincidence, which is fitted with an exponential function (red solid line).

It is clearly visible that the spectrum is continuous and that the overall activity is quite high, which is not beneficial for this kind of analysis. This high activity of about 1 kBq at the beginning of the measurements was chosen due to practical reasons. For each temperature point some hours are needed to perform the measurements and changing the temperature of the liquid scintillator and the detector, so that about one temperature per day could be investigated. Thus making 10 measurements took about 2 weeks, which is just in the range of the ^{222}Rn half-life of $T_{1/2} = 3.82 \text{ d}$.

This relatively high activity mainly disturbs the time coincidence between the bismuth and polonium alpha, which expresses itself in a 'contamination' with unwanted background events in the energy spectra after a time cut is applied. For this reason a heuristic approach for the length of the coincidence time window is chosen. In Figure 5.8.6, energy spectra of the second event (supposedly from ^{214}Po) are plotted, dependent on different coincidence time windows. The $70 \mu\text{s}$ spectrum shows the best peak to background ratio, and was hereafter chosen as time cut to isolate the ^{214}Bi - ^{214}Po coincidence. Although the ^{214}Po α -peak is nicely pronounced and isolated with this first cut, still some events from the β -spectra and the other α events are 'leaking' into these spectra.

Figure 5.8.6: Charge spectra from Radon-loaded LAB, populated with events that are falling into different time windows, ranging from $60 \mu\text{s}$ to $130 \mu\text{s}$. The ^{214}Po α -peak is clearly pronounced, but also background events from the double- α feature and the β -spectra are still visible to the left. The $70 \mu\text{s}$ cut has the best peak to background ratio.



To further improve this selection, a second cut is applied, this time on the energy of either the first or the second event in the coincidence, to clean up the spectra of the other event, respectively.

That means, to improve the ^{214}Bi β -spectra, the following selection of events is performed:

1. events with a time difference of $\leq 70 \mu\text{s}$
2. **first** event of those pairs is taken, if the **second** event lies within the [817,1170] keV energy window (the ^{214}Po α -peak)

The effect of this is demonstrated in Fig. 5.8.7. Although the actual signal sacrifice is large, the improvement on the shape and the strong suppression of disturbing α -events make this cut still useful. Especially for β -spectra it is difficult to quantify any small change of light output with temperature change, since they do not represent a steep, peak-like structure. Already a visual inspection reveals no visible change in the β -spectra with changing temperature. Nevertheless, an analysis of the pulse shapes indicates also a temperature dependence for the decay constants of the betas, see next section.

A similar event selection can be performed to enhance the ^{214}Po spectra:

1. events with a time difference of $\leq 70 \mu\text{s}$
2. **second** event of those pairs is taken, if the **first** event lies above an energy of 0.99 MeV (end-point energy of the ^{214}Pb β -spectrum)

Again, despite a large signal loss, the effect of reducing background events that disturb the shape and therefore also the position of the α -peak, is worthwhile. Beside the greatly improved signal to background ratio (compare Fig. 5.8.5 and Fig. 5.8.8), also the fit range uncertainty decreased from 1.7% to 0.3%. This is already referring to the final analysis of the peak positions, that again is performed in a two step fit procedure. As it has been done for the analysis of the Samarium loaded LAB, here again a first standard gaussian fit determines the rough peak position. Then, in a second step, the mean and sigma from the first fit is extracted to perform the actual gaussian

Table 5.8.2: List of uncertainties considered in the analysis of the ^{214}Po α -peak at room-temperature ($24.62 \pm 0.04^\circ\text{C}$) in Radon loaded LAB.

uncertainty	value [%]
fit	0.15
fit range	0.3
pulser stability	0.35
variance between rep. measurements	0.9
sum	1.7

fit in the 2σ range around this mean. Table 5.8.2 gives an exemplary overview of the uncertainty values for the analysis of the first room-temperature measurement.

An illustration of the effect of the temperature changes on the α -peak position can be found in Fig. 5.8.8, the PMT sensitivity correction is already applied. Also a graphical representation of the fit results versus temperature is given in Fig. 5.8.9.

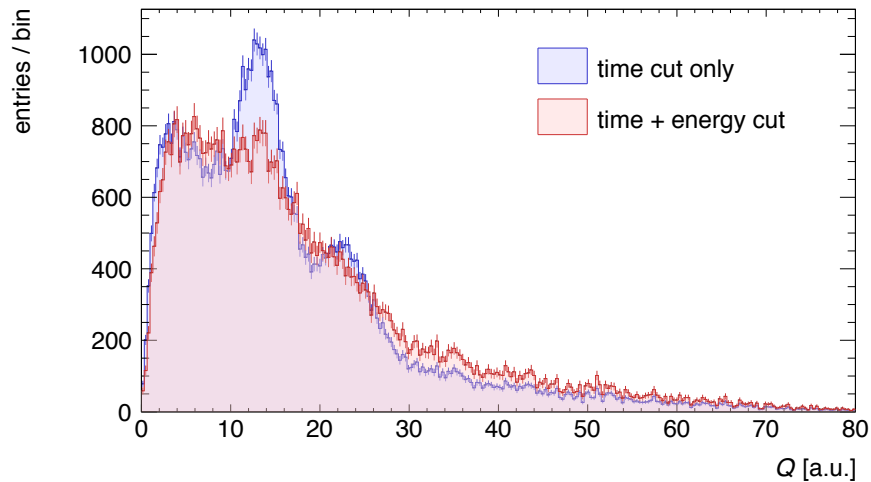
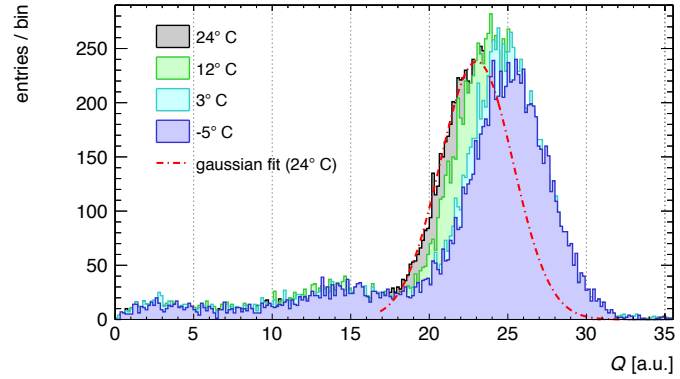


Figure 5.8.7: Comparison of charge spectra obtained from Radon loaded LAB, when applying only time cuts (blue) and constraining also the energy of the following event to the energy of ^{214}Po (red). Clearly, the peak-like features in the blue spectrum are effectively suppressed when applying the energy cut. Since signal sacrifice is large, the red spectrum is normalised to the area of the blue, for better comparison.

In a last variation of the analysis, a fit to the double α -feature of ^{222}Rn and ^{218}Po is performed, mainly for comparison and cross-check. This time, events that fall into the $70\ \mu\text{s}$ coincidence time window of the ^{214}Bi - ^{214}Po time window, are excluded from the analysis. This of course suppresses the ^{214}Po α -peak very effectively as well as the background contribution of the ^{214}Bi β -spectrum. Thus the shape and the position of the double α -peak is less influenced by the tail of the higher energy α - and β -decays. This time, only one single Gaussian is fitted to the double α -feature,

Figure 5.8.8: Comparison of charge spectra from Radon-loaded LAB (+5 g/l PPO +20 mg/l bis-MSB) at different temperatures, time and energy cuts applied, as well as PMT sensitivity correction. The ^{214}Po α -peak is clearly pronounced a well gaussian shaped. The red dash-dotted line shows the gaussian fit to the room-temperature spectrum.



though in the same manner as before. That means a first fit to roughly identify peak position and width and then a second more refined approximation. Since there is still one β -spectrum in the background, the uncertainties are much larger for this rough and simple analysis. Nevertheless the unsurprising results, also shown in Fig. 5.8.9, provide a cross-check and comparison to the outcome of the other analyses.

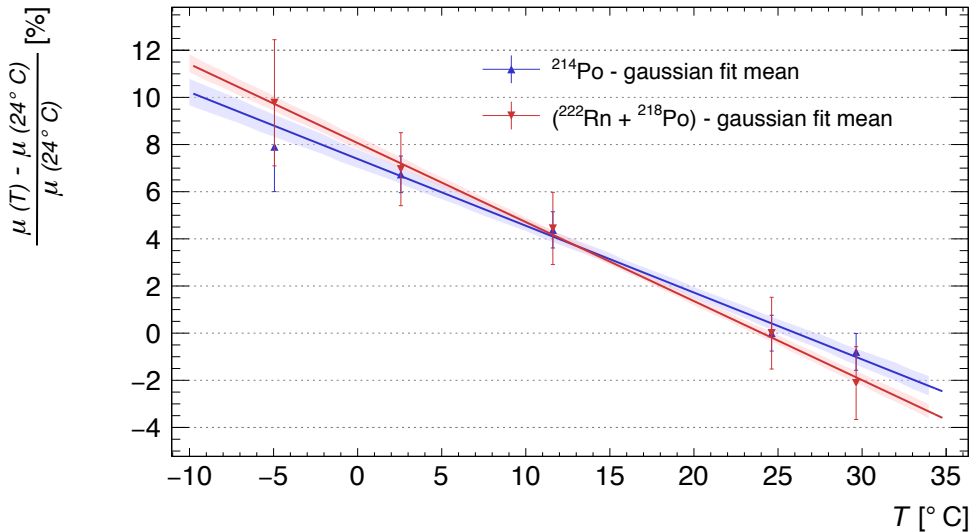


Figure 5.8.9: Shift of the mean values from fitting the ^{214}Po α -peak, after applying time and energy cuts (as in Fig. 5.8.8), in blue. And from fitting the double α -feature of ^{222}Rn and ^{218}Po , in red. Each temperature point is the average of the repeated individual measurements and these are normalised to the room-temperature value at $(24.5 \pm 0.04)^\circ\text{C}$. The shaded areas mark the 1σ uncertainty band from the linear fit.

5.8.3 Pulse shape analysis

For the pulse shape analysis of the Radon loaded LAB measurements, it is very sensible to use the data-sets with the isolated β - and α -events. This is done by applying the same time and energy cuts as they have been described in the last section. Then

again, the pulse shape average is generated by calculating the arithmetic mean of all the pulses in the data-set, for each 0.5 ns sample bin separately. Equally the variance is calculated, though due to the very large number of pulses (~ 1 M) too small to be visible in the following graphs.

When taking a first look at the averaged pulse shapes from the ^{214}Bi β -decays, they seemingly resemble the prolonged pulses that can be seen from the α activity in Samarium loaded LAB (Fig. 5.7.4). Here again, with lower temperatures the pulse get longer, while with rising temperature the slow decay component seems to be suppressed. To also quantify this behaviour and compare with the results from the α -decays, the same fit as for the Samarium loaded LAB is applied, see Fig. 5.7.5, Equation 5.8 and the respective description in sec. 5.7.2. This means fitting the shape with a sum of two exponential functions, first for the room-temperature measurement to find and fix two parameters. Then, the fitting to the other temperature shapes reveal the change in the decay constants. The results for the two decay constants from the fitting are shown in Fig. 5.8.11.

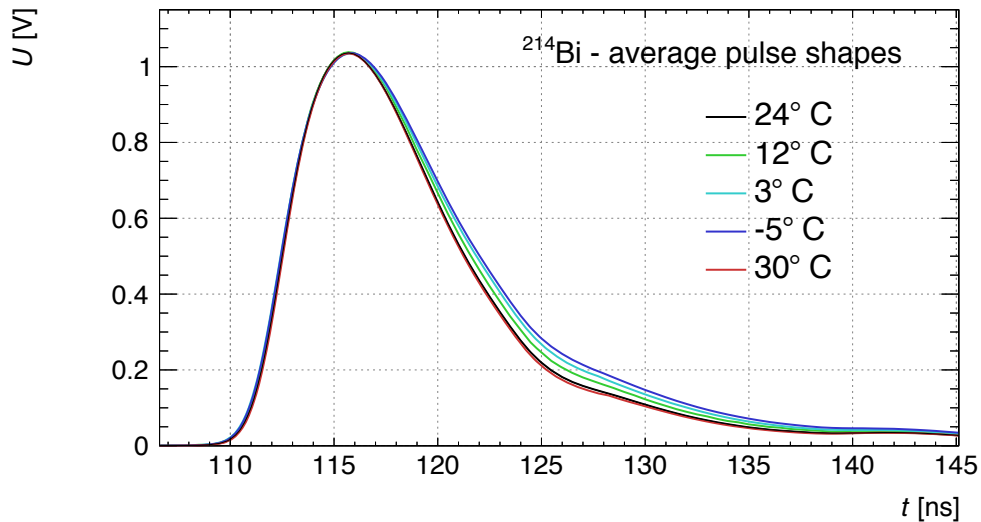


Figure 5.8.10: Average pulse shapes from ^{214}Bi β -decays in Radon loaded LAB, at different temperatures. Each line is calculated from ~ 1 M pulses, and normalised to the height of the room-temperature shape.

As it has been observed for the α -decay of ^{147}Sm , the fast decay component experiences only minor changes with temperature variation of about $\approx 1\%$ over a range of 35°C . Contrary, even though the uncertainties are larger, the slow decay part changes $\approx 5\%$ over the same range. This is significantly more and close to observation of this from ^{147}Sm , even though here it is electrons instead of helium nuclei.

This similar behaviour can again be confirmed with yet another α -source, the well isolated ^{214}Po decay in the Radon loaded LAB. Again, applying the energy- and time-cuts investigated in the last section, ensures the very good separation of the polonium decay from unwanted backgrounds. The averaged pulses can be seen in Figure 5.8.12, and show a now familiar picture.

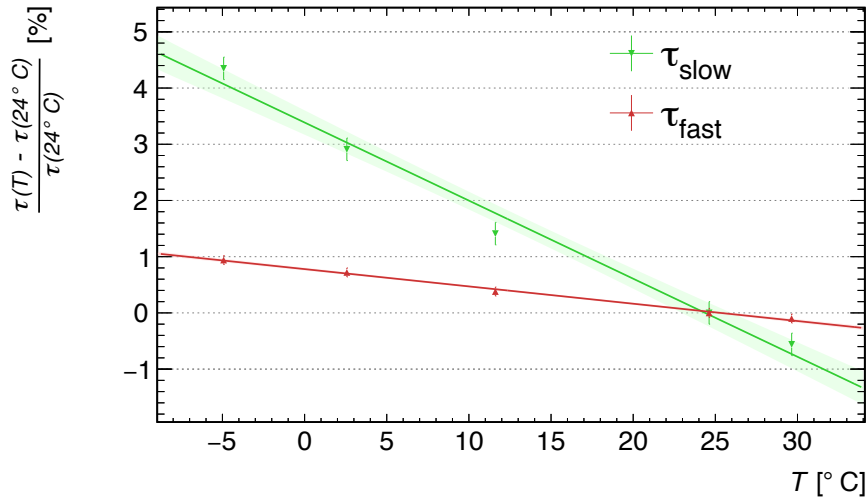


Figure 5.8.11: Change of the decay constant fit values of averaged pulse shapes from ^{214}Bi , at different temperatures. The shaded areas show the 1σ confidence band from the linear fit.

Again, while the fast decay component exhibits only a small change with temperature, the slow decay becomes $\approx 4\%$ stronger at 35°C lower temperature. This is very similar to changes observed from ^{147}Sm , and a bit less than that of the ^{214}Bi β -decays.

5.9 Discussion and Conclusions

This last section of the chapter shall now finally conclude and compare all the obtained results from the various measurements, as well as compare them to outcomes from previous work done by others.

Firstly it can be stated that a detector was designed, built, developed and operated successfully in order to investigate the temperature behaviour of the light generation in LAB based liquid scintillators. The light output and pulse shapes from electrons, generated from gamma-ray interaction, and α -particles from in-situ sources was measured in a temperature range from -4°C to 30°C .

If the results from all energies are combined and a linear approximation is assumed, the temperature coefficient for **electrons** obtained in this work is $(-0.17 \pm 0.02)\%/^\circ\text{C}$. This is in the same order of magnitude as the observation by Xia et al. [Xia14], they show diagrams which correspond to coefficients of $\approx -0.32\%/^\circ\text{C}$. As their setup is one of the very few well designed ones, their result seems trustworthy and find more or less a confirmation with this independent study. Although there are more studies to mention here, namely those by Seliger and Ziegler [Sel56], Laustriat and Coche [Lau60], Homma et al. [Hom87] and Buontempo [Buo99], all of these have significant problems either in their measurement concept or present their data in an untransparent way, so that direct comparison is very difficult. This has already been discussed in detail in section 4.4. Nevertheless, all of

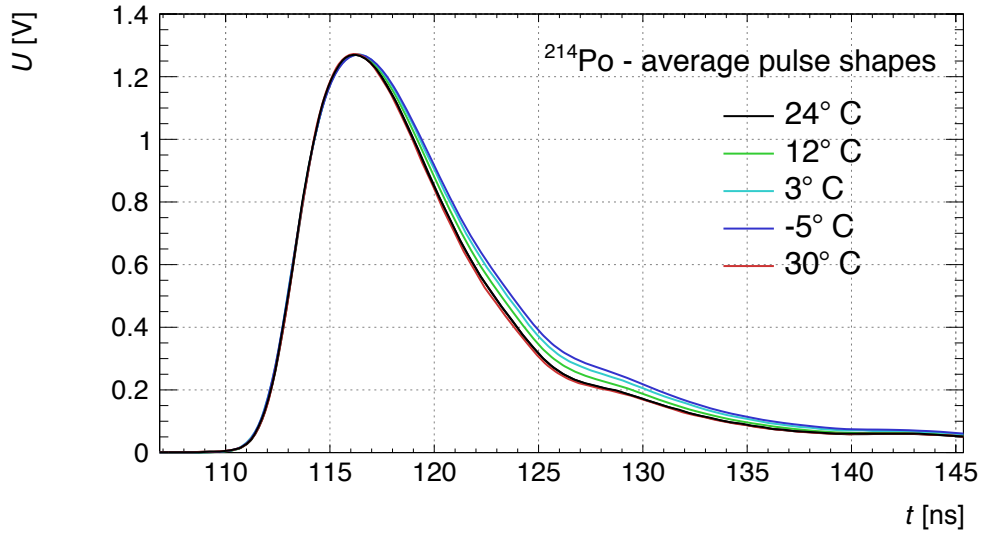


Figure 5.8.12: Average pulse shapes from ^{214}Po α -decays in Radon loaded LAB, at different temperatures. Each line is calculated from ~ 1 M pulses, and normalised to the height of the room-temperature shape.

those publications (except [Sel56]) indicate and show a significant increase in electron generated light output at lower temperatures.

For α -particles previous measurement data is even more scarce, only Homma et al. [Hom85b; Hom87] present pulse-height spectra from ^{241}Am at different temperatures. Unfortunately they do not analyse these spectra quantitatively but show only very coarse diagrams. A very rough calculation from a 'by hand' analysis of the presented spectra, using only two data points for ^{241}Am in a PPO-benzene mixture, results in $\approx -0.5\ \%/^{\circ}\text{C}$. In this work, the combined average temperature coefficient for all energies, including the values for ^{222}Rn , ^{218}Po , ^{214}Po and ^{147}Sm , is $(-0.35 \pm 0.03)\ \%/^{\circ}\text{C}$, which is in the same order of magnitude again and confirms the overall trend.

A last interesting aspect for the comparison of light output temperature behaviour is an analysis of a possible energy dependence. Figure 5.9.1 illustrates the combined data for electrons (generated by gamma-rays) in blue and for α -particles in green. The first observation is the already mentioned overall trend of slightly negative temperature coefficients of less than one percent per degree Celsius. Three very simple models have been tested. Fitting a global constant describes the data very badly (p-value $< 10^{-10}$) but excludes a zero temperature coefficient already by more than 30σ . The fit value for a global constant is $(-0.29 \pm 0.01)\ \%/^{\circ}\text{C}$. A better approximation, but still very bad is possible by assuming a linear function, which yields a p-value of $\sim 10^{-6}$. Out of the three chosen models, a fit with separate constants for **electrons** $(-0.17 \pm 0.01)\ \%/^{\circ}\text{C}$ and **alphas** $(-0.36 \pm 0.01)\ \%/^{\circ}\text{C}$ yields the best result with a probability value of 6×10^{-4} . One reason for the overall bad results in approximating an analytical model is the position and large uncertainty of the ^{147}Sm data point. With these few data points, a final conclusion seems difficult and none of

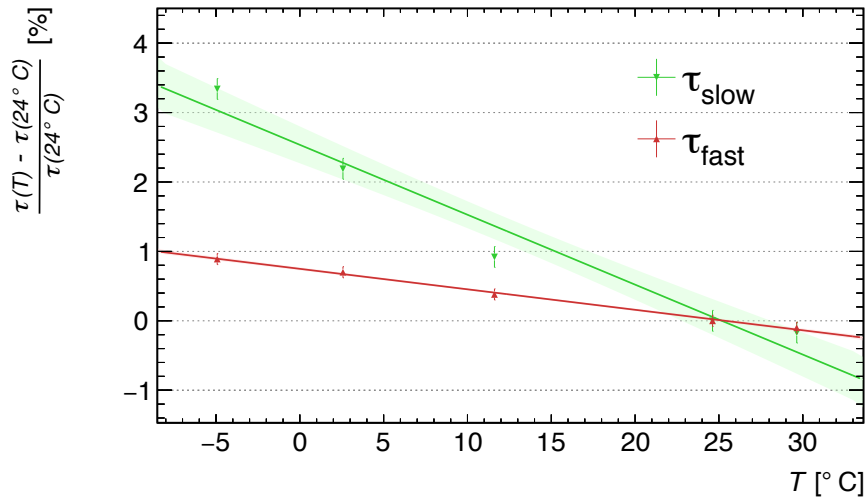


Figure 5.8.13: Change of the decay constant fit values of averaged pulse shapes from ^{214}Po , at different temperatures. The shaded areas show the 1σ confidence band from the linear fit.

the three simple models can describe the data well. Judging purely from the numbers, the *two constants model* has a slight preference. As it is very difficult to measure α sources at even lower energies (due to the ten fold quenching in energy), the only realistic option in clarifying this would be measuring higher energy electrons, in the range above 3 MeV. This might be achievable with high energy gamma rays. The data point estimated from Xia et al. [Xia14] for ^{137}Cs of $\approx -0.32\ \%/^{\circ}\text{C}$ would push the first blue data point in Fig. 5.9.1 down quite a bit and more towards the regime of the alphas.

Useful insights for a physics interpretation are also provided by the comparison of the pulse shape analysis results. For this work, the temperature behaviour of averaged pulse shapes from ^{147}Sm , ^{214}Po and ^{214}Bi have been analysed. All of these are averages of a very large amount of shapes, on the order of 1 million each. They have been fitted by a two part exponential function with two separate decay constants (Eq. 5.8), which turned out to be the only reasonable way to approximate these shapes analytically. All three isotopes show a significant increase in the strength of the later pulse shape with lower temperatures, such that the decay constant characterising the ‘slow’ decay component increases. An overview of some of these values is given in Table 5.9.1. When comparing the diagrams for the relative change of the constants (Fig. 5.7.6, Fig. 5.8.13 and Fig. 5.8.11) the similarities are striking. Especially the trace of the data points for the slow component seem to follow a non-linear curve, maybe quadratic or exponential. Nevertheless, the simplest linear approximation gives the following results for the slope of the slow decay constant versus temperature, for ^{147}Sm ($-0.09 \pm 0.003\ \%/^{\circ}\text{C}$), for ^{214}Po ($-0.1 \pm 0.005\ \%/^{\circ}\text{C}$) and for ^{214}Bi ($-0.14 \pm 0.007\ \%/^{\circ}\text{C}$). As the two alphas might be actually the same, the Bismuth electrons seem to show an even larger increase in the slow decay time with lower temperatures.

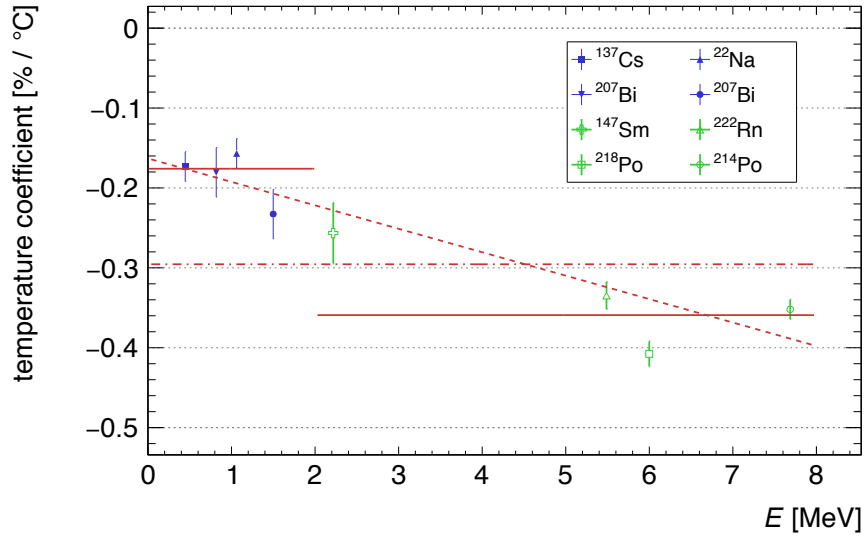


Figure 5.9.1: Temperature coefficients for four gamma-ray emitting isotopes (blue, filled data points) and four α -emitters (green hollow points) in LAB based liquid scintillator. Model testing has been done by fitting a global constant (red dash-dotted line) to separate constants (red solid lines) and a linear function (red dashed line).

Table 5.9.1: Comparison of exponential decay constants for Samarium and Polonium α -isotopes and the Bismuth β -decay, at room-temperature and at -4°C .

isotope	τ_{fast} @ 24°C [ns]	τ_{fast} @ -4°C [ns]	τ_{slow} @ 24°C [ns]	τ_{slow} @ -4°C [ns]
^{147}Sm	4.5 ± 0.1	4.5 ± 0.1	16.9 ± 0.1	17.4 ± 0.1
^{214}Po	4.3 ± 0.1	4.3 ± 0.1	22.8 ± 0.1	23.6 ± 0.1
^{214}Bi	4.2 ± 0.1	4.2 ± 0.1	20.0 ± 0.1	20.9 ± 0.1

A final physics interpretation needs to take a lot of different information into account. Firstly an overall increase in scintillation light with lower temperatures has been reported throughout literature as well as it has been seen in this work. A linear behaviour is likely and hints are found that α -particles and electrons have different temperature coefficients. Secondly, seemingly so far no other study has had the chance to analyse the pulse shapes of these radiations in liquid scintillator at different temperatures. This work found that the slow component of an exponential decay of the scintillation is stronger pronounced at lower temperatures. As the triplet lifetime of benzene matches this slow decay component well [Cun65; Cun70; Li15; OKe11], this result can be seen as an indication that either more triplet states are populated or that the radiative de-excitation of those is more efficient at lower temperatures.

The increased population would fit into the theory of Birks and Conte [Bir64; Con68], who proposed that the energy transfer between solvent-solvent and solvent-solute molecules is mainly due to excimer formation. As excimer formation is enhanced at lower temperatures and higher viscosity, a higher light yield at lower

temperatures would fit into this picture. But Mathad and Umakantha [Mat85] disfavoured this explanation convincingly in their study, as already discussed in 4.4. Considering all the presented arguments, it seems likely that the temperature quenching effect is mainly due to more efficient triplet de-excitation as non-radiative paths are increased with higher temperature, such as collisional processes.

CHAPTER 6

Muons in SNO+

COSMIC ray muons are one of the major background components for all low count rate experiments, no matter if their search is dedicated to neutrinos, dark matter or other rare or undiscovered physics events. Unlike the so-called 'soft' cosmic ray components like electrons, positrons, photons, pions or kaons, muons are not easily attenuated by a shielding. While it is sometimes sufficient to veto muons with special detectors, mostly an actual reduction of the muon flux is inevitable. Due to their relatively low energy loss in even very dense matter, the only practical shielding option for all these very sensitive experiments is to reside in a deep underground laboratory, to some extent escaping the surface muon flux of about $70 \mu \text{m}^{-2} \text{s}^{-1} \text{sr}^{-1}$ [Pas93; Gri01]. Until recently, the site of the original SNO experiment in Sudbury (Canada) was the worlds deepest underground laboratory with an flat overburden of 2.092 km, which amounts to ≈ 6 km in water-equivalent. This provides an excellent shielding for the SNO+ experiment against all cosmic rays and only muons are able to sometimes penetrate this deep into the rock. The flux of muons inside SNO+ is very well known through the measurement by SNO and can be expected as $62.9 \pm 0.2 \mu \text{d}^{-1}$, which is ≈ 23 k muons per year [Arh09].

The residual muons have a via simulations estimated mean energy of 350 GeV [Arh09] and are not only a direct disturbance of the experiments (e.g. by excitation & ionisation), but also produce dangerous isotopes, either directly e.g. by spallation of carbon, or indirectly via electromagnetic- and hadronic showers they induce, which in turn produce radioactive isotopes. According to a measurement and simulations by the KamLAND collaboration, actually at least 60% of the produced radioactive isotopes are generated by showering muons [Abe10]. This observation is supported by independent simulation studies by Galbiati et al. [Gal05] and Zbiri [Zbi10]. A closer look at these interactions and the consequences will be given in the following sections 6.1 and 6.2. One main objective of the muon related part of this thesis is the estimation of these induced backgrounds and if they can be mitigated by a technique that is successfully applied by the Borexino collaboration. This involves a very effective, precise and reliable reconstruction of the muon tracks inside the detector, as a cylindrical fiducial volume cut around this track is used to exclude induced backgrounds. For Borexino this is a crucial part of their background reduction technique as the overburden at the Gran Sasso National Laboratory (LNGS) underground site is much shallower, and the muon flux thus two orders of magnitude higher than at SNOLab.

Therefore, in the scope of this thesis, a similar muon track reconstruction was developed and implemented for SNO+, and a large number of muon events was simulated with the SNO+ software, called Reactor Analysis Tool (RAT), which makes great use of the well known Geant4 software toolkit [Iva03]. The big difference between SNO+ and Borexino, KamLAND and other large scale liquid scintillator experiments is the absence of an external muon tracker at SNOLab. Such a device was present towards the end of SNO, but unfortunately was dis-assembled and removed. In terms of a correct and reliable track reconstruction, this is a major drawback. Despite attempts to accumulate the necessary funding, at the time of this thesis, there is no plan to install such a tracker again for SNO+. Thus, the experiment has to rely entirely

on a simulation based track reconstruction, and it will be pointed out later how this constrains the muon-induced background reduction.

In contrast to the other main part of this thesis, the following work is based purely on simulations and scaling calculations, since the SNO+ detector is not yet filled with water or liquid scintillator. All simulations have been carried out at the centre for high performance computing (ZIH) of the TUD, and the next section will give a brief overview of the standard physics of cosmic ray muons and some simulation details.

6.1 Cosmic ray muons underground

Primary cosmic rays consist to about 85% of protons with energies up to 10^{11} GeV. When colliding with protons and neutrons in the earths atmosphere, they produce mainly pions and kaons, which subsequently decay into muons and neutrinos, e.g. via

$$\pi^\pm \rightarrow \mu^\pm + \nu_\mu(\bar{\nu}_\mu) \quad \text{and} \quad K^\pm \rightarrow \mu^\pm + \nu_\mu(\bar{\nu}_\mu) \quad (6.1)$$

and thus generating high energy muons in the atmosphere. The more abundant positive charge in the primary spectrum and the excess of π^+ mesons in the forward fragmentation region of proton initiated interactions is also visible in the μ^+/μ^- charge ratio, which is $\approx 1.1 - 1.4$ in the energy range of 1 GeV - 100 GeV [Pas93; Mot03]. When the curvature of the earth can be neglected ($\theta < 70^\circ$) and muon decay is also negligible ($E_\mu > 100/\cos\theta$ GeV), the cosmic ray muon flux at the earths surface can be described by the so-called Gaisser parametrisation [Gai90]:

$$\frac{d^2\Phi_\mu}{dE_\mu d\Omega} \simeq \frac{I_0 E_\mu^{-\gamma}}{\text{cm}^2 \text{sr GeV}} \left(\frac{1}{1 + \frac{1.1 E_\mu \cos\theta_\mu}{115 \text{ GeV}}} + \frac{0.054}{1 + \frac{1.1 E_\mu \cos\theta_\mu}{850 \text{ GeV}}} \right) \quad (6.2)$$

with $\gamma = 2.77 \pm 0.03$ as the muon spectral index, $I_0 \approx 0.14$ a normalisation constant, E_μ the muon energy at the surface and θ_μ the azimuth inclination of the muon track. Since the minimum muon energy at the surface has to be at least 3 TeV for it to reach the underground site of SNO+ [Arh09], this formula is a valid approximation and was the basis for the following simulations.

High energy muons passing through matter are loosing their energy mainly through ionisation, bremsstrahlung, pair production (e^-e^+) and photo-nuclear reactions. A common simplified formulation is

$$-\frac{dE_\mu}{dx} = a(E_\mu) + b(E_\mu)E_\mu \quad (6.3)$$

where $a(E_\mu)$ denotes the ionisation energy loss and $b(E_\mu)$ the sum of the three radiative processes. The ratio $E_{\mu c} = a/b$ is known as the 'critical' energy at which ionisation and radiative energy loss are equal. Towards higher energies, the radiation processes become dominant and vice versa. This quantity ($E_{\mu c}$) depends strongly on the chemical composition of the matter the muon is traversing, and can be calculated for standard rock ($\rho = 2.65 \text{ g/cm}^3$ and $\langle Z^2/A \rangle = 5.5$) to $E_{\mu c} \approx 500$ GeV. It

is important to note that below this critical point the dominating ionisation loss can be treated as a continuous process and is well described by the Bethe-Bloch formula, but above this energy, stochastic calculations have to be included to account for single interactions in which a particle can lose a large fraction of its energy.

In Sudbury the exact density and chemical composition of the rock is very well known due to the local mining activities, and they vary only slightly in the vicinity of the mine, with the exception of a large deposition of nickel ore. While the density is slightly lower at the surface than deeper in the mine, the average density is reported as $\rho = 2.83 \pm 0.05 \text{ g/cm}^3$ and the average chemical composition is 45 % oxygen, 26 % silicon, 9 % aluminium and 4 % iron and thus $\langle Z^2/A \rangle = 5.84$ [Arh09]. All this information has been included in a simulation which is propagating the incident cosmic ray muon flux through the rock, down to the depth of the SNO+ detector. This has been done by the MUSIC muon transport code that was developed by Antonioli et al. [Ant97], and the resulting muon energy- and angular distributions at the depth of SNO+ are shown in Fig. 6.1.1.

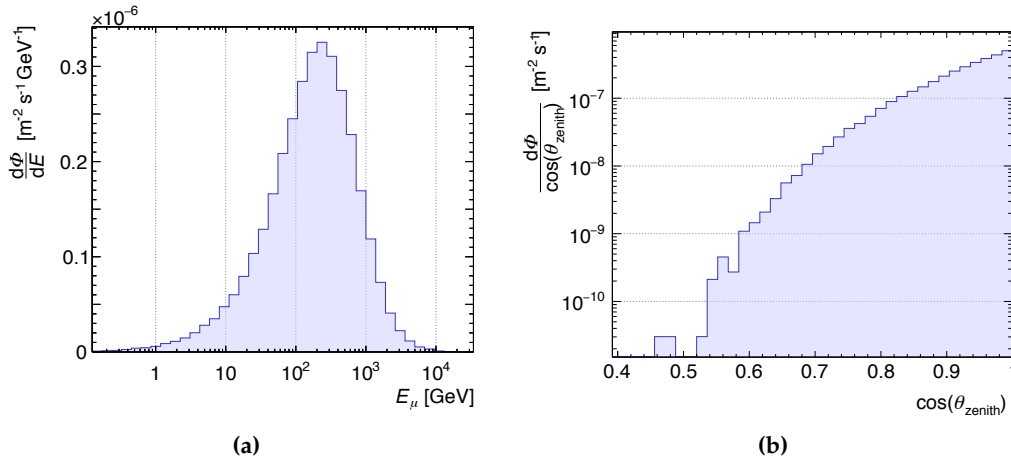


Figure 6.1.1: Energy distribution **(a)** and zenith angle (θ) dependency **(b)** of the muon flux at the site of the SNO+ experiment, as it has been simulated with the MUSIC muon transport code. The initial surface flux was calculated with the Gaisser formula (Eq. 6.2).

The exact integrated underground muon flux was measured by SNO [Arh09] and amounts to

$$\Phi_{\mu} = (3.31 \pm 0.01 \text{ (stat.)} \pm 0.09 \text{ (sys.)}) \times 10^{-10} \text{ cm}^{-2} \text{ s}^{-1} \quad (6.4)$$

6.2 Muon-induced backgrounds

Once the cosmic ray muons have traversed the about 2 km rock overburden, they reach the SNO+ detector and produce Cherenkov light in the water shielding and liquid scintillator, as well as excite the scintillation in the LAB mixture. Some of those highly energetic muons will interact with the nuclei in those compounds, producing

neutrons and radioactive isotopes inside the detector or its vicinity, that are potentially interfering with the measurement goals. Event though some of the neutrons produced in the water envelop may travel towards the fiducial volume inside the AV, this work focuses on the backgrounds isotopes produced in the liquid scintillator, namely in a pure LAB mixture with only 2 g/l PPO added, which is the basic composition of the mixture that will be used in SNO+. Even though a significant amount of tellurium will be loaded into the scintillator for the $0\nu\beta\beta$ -phase of the experiment, this scenario is not considered in this work, mainly focusing on the backgrounds for a pure scintillator (solar phase) of SNO+. In a very recent study, the Double Chooz collaboration reports results of muon capture rates on light elements in their scintillator [Abe15]. These processes have not been taken into account for deep underground experiments yet, but are worthwhile investigating in the future, also for SNO+.

Since LAB is only composed of hydrogen and carbon, ^{12}C presents the main target for muons in this liquid, as it is naturally abundant with 98.93% (and ^{13}C accounting for the rest). A cross-section measurement of muons with a carbon target has been done at the CERN SPS accelerator [Hag00], unfortunately only for two muon energies, 100 GeV and 190 GeV. Nevertheless, the obtained values can be used for a calculation using a power law dependency of the production rate, which will be presented in the next section. A list of possible and relevant isotopes that can be produced by the interaction of muons and their secondary shower particles with ^{12}C is given in Table 6.2.1.

Table 6.2.1: List of relevant radioactive isotopes, their half-lives, radiation types and Q-values as they are produced by muons and their secondaries in liquid scintillator (spallation of ^{12}C), data from [Hag00; Bel13a; Tab99].

isotope	$T_{1/2}$	type	Q-value [MeV]
^6He	0.81 s	β^-	3.5
^8He	0.12 s	β^-	10.6
^8Li	0.84 s	β^-	16.0
^9Li	0.18 s	β^-	13.6
^{11}Li	0.09 s	β^-	20.8
^7Be	53.3 d	γ (10.5%)	0.478
^{11}Be	13.8 s	β^-	11.5
^8B	0.77 s	β^+	13.7
^{12}B	0.02 s	β^-	13.4
^9C	0.13 s	β^+	16.0
^{10}C	19.3 s	$\beta^+ + \gamma$	1.9 + 0.72
^{11}C	20.38 min	β^+	0.96
^{12}N	0.011 s	β^+	17.3

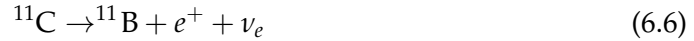
When taking a closer look at Table 6.2.1 it becomes clear that the majority of the isotopes will very likely not present a thread to the physics goals of SNO+ as they are very short lived, especially if they will be produced only in very small amounts, as it

is suggested by the results from other experiments and the measured cross-sections. They can then be easily vetoed by excluding any events in a short time window of $\mathcal{O}(\text{min})$ after a muon event. Exceptions are ^{11}C and ^7Be , with the latter one, although being predicted, has never been measured in any deep underground liquid scintillator experiment. A production of ^7Be is expected while the liquid scintillator is stored at the surface, but purification studies suggest that more than 99 % of this isotope can be removed before the LAB is used in SNO+.

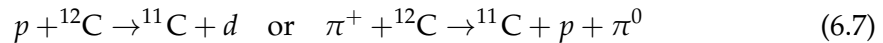
This leaves ^{11}C as 'dangerous' muon-induced background in SNO+ that also will be produced in detectable rates (see next section). Fortunately, this carbon isotope is a β^+ -emitter and has a quite distinct signature, making it effectively detectable. One reason is that in 95 % of the direct production processes, a neutron can be found in the final state:



This neutron is captured from hydrogen in 99 % of the cases within $\approx 250 \mu\text{s}$ [Bel13a] (and the remaining 1 % falls to a capture on ^{12}C) and subsequently emitting a characteristic gamma-ray with an energy of $E_\gamma = 2.2 \text{ MeV}$, making it the second part of a three-fold coincidence, after the initial muon event. The third part is then the β^+ -decay:



with a half-life of $T_{1/2} = 20.39 \text{ min}$ and an end-point of the β -spectrum at 0.96 MeV. As the positron annihilates immediately, the total deposited energy in the detector is 1.2 MeV to 1.98 MeV. In the case of an indirect ^{11}C production, a three-fold coincidence tagging is not applicable, since the neutron in the final state is missing. This is the case when muon-induced electromagnetic- or hadronic showers and thus processes such as



are responsible for the production. Those 'invisible' channels account for about 5 % of the production rate [Gal05]. A more detailed description of the ^{11}C reduction method will be presented in section 6.2.3.

With its energy characteristics, the ^{11}C β^+ -decay is e.g. a major background for a pep-neutrino signal, as about 35 % of the ^{11}C decays would fall into the best energy window of [0.8,1.3] MeV for the detection of these solar neutrinos via ν - e^- -scattering [Gal05], also refer to Fig. 3.3.1 in section 3.3. Therefore quantitative calculations, estimations and simulations of muon-induced backgrounds in the liquid scintillator are sensible and needed as input for complete sensitivity studies and evaluation of the possible physics with SNO+.

In order to perform an estimation of the muon induced isotopes, the number of target atoms needs to be calculated. For the SNO+ LAB, assuming a mean molecular composition of $\text{C}_{17.3}\text{H}_{28.3}$ (refer to sec. 4.3), the ^{12}C number density is $\rho_N(^{12}\text{C}) = 3.72 \times 10^{22} \text{ cm}^{-3}$, which amounts to a total mass of $m(^{12}\text{C}) = 672 \text{ t}$. Furthermore a density of $\rho = 0.854 \text{ g cm}^{-3}$ at 15° C (operating temperature) [OKe09] and a contribu-

tion of 0.171 % PPO has been assumed. This amounts finally to the following number of target atoms of ^{12}C :

$$N(^{12}\text{C}) = 4.54 \times 10^{31} \quad (6.8)$$

To conclude this section, the view shall be directed towards **muon-induced neutron production**. This topic is of great interest in all low count-rate experiments and a lot of theoretical work in form of simulations have been done, as well as attempts to formulate universal laws [Wan01; Kud03; Ara05b; Mei06; Mar07; Ara08; Lin09; Rei13; Aga13]. However, as the neutron detection, and especially the link between an incident muon and neutron production is very hard to establish, only a few measurements are providing reliable values and an incomplete list is presented in Table 6.2.2. One reason is that muons passing the detectors in their vicinity, and are not directly detected, might create fast neutrons in the surrounding rock or shielding, which in turn can reach the sensitive detector volumes. Besides the already mentioned neutron production through carbon spallation (an example for the first item on the following list), high energy muons can produce neutrons directly and indirectly via:

- nuclear disintegration via photon exchange between muon and nucleus - so called 'muon spallation'
- muon capture and subsequent neutron emission from excited nuclei
- photo-nuclear reactions of muon-induced electromagnetic showers
- nuclear reactions of hadronic cascades produced by muons

As a direct consequence of this list, not only electromagnetic- but also hadronic-interactions have to be taken into account in simulations and any kind of analytic predictions. In the next section, it will be shown how this has been done for the simulations that were carried out with the RAT software. An important quantity is the so-called neutron yield Y_n , commonly defined as produced neutrons per muon and muon track unit length in a medium:

$$Y_n = \frac{N_n}{N_\mu} \cdot \frac{1}{\langle l_\mu \rangle \cdot \rho_{scint} \cdot \varepsilon} \quad (6.9)$$

where N_n , N_μ are the numbers of neutrons and muons, respectively, and $\langle l_\mu \rangle$ is the average muon path in the medium with density ρ . The value for the detection efficiency ε is experiment specific and usually composed of several parts, such as neutron detection- and coincidence efficiency. This value is a crucial part in the analysis and comparison of experimental data and has become a topic of diverse discussion.

When analysing the available data in Tab. 6.2.2, the most obvious observation is the increased neutron yield at higher depths, apparently as some kind of function of mean muon energy. Several attempts have been taken to formulate a universal formula $Y_n(\langle E_\mu \rangle)$ for the production of muon-induced neutrons [Wan01; Kud03; Mei06; Aga13]. While predictions from simulations became much better in the last decade by, e.g. including electromagnetic- and hadronic showering, still some inconsistency

remains, especially in comparison with a power-law behaviour. Usually, these studies then assume some corrections for, at times very technical, experimental effects. Whether these assumptions are correct or biased towards a successful approximation, remains a topic of discussion. However, the author considers the most valuable data for comparison with this work, stems from the two to SNO+ most similar experiments Borexino [Bel13a] and KamLAND [Abe10].

Table 6.2.2: Available data on muon-induced neutron production rates in underground laboratories.

measurements	depth [km.w.e.]	$\langle E_\mu \rangle$ [GeV]	$\langle Y_n \rangle$ [$\text{n } \mu^{-1} (\text{g}/\text{cm}^2)^{-1}$]
Hertenberger [Her95]	0.02	13	$(2 \pm 0.7) \times 10^{-5}$
Bezrukov [Bez73]	0.025	14.7	$(4.7 \pm 0.5) \times 10^{-5}$
Boehm [Boe00]	0.032	16.5	$(3.6 \pm 0.31) \times 10^{-5}$
Bezrukov [Bez73]	0.316	55	$(1.21 \pm 0.12) \times 10^{-4}$
Enikeev [Eni87]	0.75	120	$(2.15 \pm 0.15) \times 10^{-4}$
KamLAND [Abe10]	2.7	260	$(2.8 \pm 0.3) \times 10^{-4}$
Aglietta LVD [Agl99]	3.1	270	$(1.5 \pm 0.4) \times 10^{-4}$
Borexino [Bel13a]	3.8	290	$(3.1 \pm 0.15) \times 10^{-4}$
Aglietta LSD [Agl89]	5.0	346	$(5.3 \pm 1.1) \times 10^{-4}$

6.2.1 Scaling calculations

Since simulations can only be as good as their physics input, it is sensible, at least for comparison, to calculate production rates of muon-induced isotopes by making use of real data that was reported by similar experiments, such as KamLAND [Abe10] and Borexino [Bel13a]. This can be done in the following two ways, making the appropriate assumptions. Table 6.2.3 gives an overview of the muon characteristics at the experimental sites of the three similar liquid scintillator experiments, including SNO+. The major difference is the two to three magnitudes smaller muon flux at the SNOLab site. The overall higher mean muon energy for SNO+ might be somewhat misleading, as this is only a result of an overall much smaller flux and much less low energy muons.

Table 6.2.3: Comparison of the main muon characteristics at three major liquid scintillator experiments.

	Φ_μ [$\text{cm}^{-2}\text{s}^{-1}$]	$\langle E_\mu \rangle$ [GeV]	$N(^{12}\text{C})$
KamLAND	$(1.49 \pm 0.14) \times 10^{-7}$	260 ± 8	4.30×10^{31}
Borexino	$(3.22 \pm 0.08) \times 10^{-8}$	289 ± 19	4.51×10^{31}
SNO+	$(3.31 \pm 0.10) \times 10^{-10}$	350	4.54×10^{31}

A **first method** is to **extrapolate the measured cross-sections** (at two energies) from Hagner et al. [Hag00] for a production rate calculation. In this publication, it is

assumed that the energy dependence of the cross-section can be described by a power law

$$\sigma_{tot}(E_\mu) \propto (E_\mu)^{\alpha_{meas}} \quad (6.10)$$

where the exponent α_{meas} is derived as the normalised logarithmic ratio of the cross-sections at the two energies:

$$\alpha_{meas} = \frac{\ln(\sigma_{190}/\sigma_{100})}{\ln(190 \text{ GeV}/100 \text{ GeV})}. \quad (6.11)$$

In order to calculate the production rate, it is necessary to either include the differential muon energy spectrum at the underground site, or approximate the mean muon energy. In the first case, the production rate per isotope i , R_i is given by

$$R_i = N(^{12}\text{C}) \cdot \sigma_i(1 \text{ GeV}) \int_0^\infty \left(\frac{E_\mu}{1 \text{ GeV}} \right)^{\alpha_i} \frac{dN_\mu}{dE_\mu} dE_\mu \quad (6.12)$$

with the number of target atoms $N(^{12}\text{C})$ and the cross-section σ_i at a muon energy of 1 GeV. This can also be written in the following way [Hag00]:

$$R_i = \pi r_{AV}^2 \Phi_\mu t \int_{E_1}^{E_2} \int_{0.2}^1 \int_{b=0}^{r_{AV}} \int_{\phi=0}^{2\pi} \left(\frac{\rho(^{12}\text{C}) \sigma_i(E_\mu) P(E_\mu, \cos \theta) f(b)}{S(E_\mu)} \right) d\phi db d(\cos \theta) dE_\mu \quad (6.13)$$

with E_1 and E_2 as the initial- and final energy of the muon on its track through the liquid scintillator, $S(E_\mu)$ the stopping power, the time t , the impact parameter distribution $f(b)$ and the muon energy and zenith angle distribution $P(E_\mu, \cos \theta)$. The following steps were taken to perform these integrations. A large set of muons in SNO+ (≈ 15 k) are simulated with the RAT software, which is based on the well known Geant4 software toolkit. For these muons, the impact parameter distribution $f(b)$ is assumed uniform in area and the energy- and angular distribution shown in Fig. 6.1.1 is used. The initial condition such as energy (E_1), impact parameter b and direction are chosen randomly and the energy integral is approximated with a summation in 1 k steps. The individual amounts of produced isotopes are listed in Table 6.2.4.

In the second case, when approximating the muon energy distribution by a simple mean energy $\langle E_\mu \rangle$, the production rate per isotope can be formulated as

$$R_i = N(^{12}\text{C}) \cdot \sigma_i(190 \text{ GeV}) \cdot \beta_\alpha \left(\frac{\langle E_\mu \rangle}{190 \text{ GeV}} \right)^{\alpha_i} \Phi_\mu \quad (6.14)$$

where Φ_μ denotes the underground muon flux and β_α a correction factor for the averaged muon energy $\beta_\alpha = \langle E_\mu^\alpha \rangle / \langle E_\mu \rangle^\alpha$. The individual rates can then be calculated using the weighted mean $\langle \alpha \rangle = 0.73 \pm 0.10$, a $\beta_\alpha = 0.87 \pm 0.03$ [Hag00], the mean muon energy $\langle E_\mu \rangle = 350 \text{ GeV}$ [Arh09] and the respective values for the number of target atoms and muon flux for SNO+ from 6.8 and 6.4. Again, the resulting amounts for the individual isotopes can be found in Table 6.2.4.

A **second method** is the **extrapolation** of actually **measured data** of isotope production in similar deep underground liquid scintillator experiments. Assuming simple rate proportionalities, such as

$$R_i \propto (E_\mu)^{\alpha_i} \cdot \Phi_\mu \cdot N(^{12}\text{C}) \quad (6.15)$$

the evaluation of the ratio R_i/R_{data} can be used to estimate the production rates in SNO+ via

$$R_i = R_{data} \cdot \left(\frac{\langle E_\mu \rangle}{\langle E_{\mu,data} \rangle} \right)^{\alpha_{i,sim}} \cdot \frac{\Phi_\mu}{\Phi_{\mu,data}} \cdot \frac{n(^{12}\text{C})}{n_{data}(^{12}\text{C})} \quad (6.16)$$

here the used power law exponents $\alpha_{i,sim}$ are obtained from a fit to simulated production yields, as they are presented by the KamLAND collaboration [Abe10], because these values are available for more isotopes.

However, some of the $\alpha_{i,sim}$ values have in turn been replaced by those from another study by Zbiri [Zbi10]. In this work, Zbiri simulated mono-energetic muons (only μ^-) in the energy range from 10 GeV to 380 GeV in a setup with a 1 m thick rock wall (SiO_2) that surrounds a 10 m cube of dodecane liquid scintillator ($\text{C}_{12}\text{H}_{26}$). It is demonstrated that especially the production of neutrons and secondaries in muon-induced electromagnetic- and hadronic showers enhances the radioactive isotope production significantly. The in [Zbi10] published neutron yields as a function of muon energy are those in best agreement with available data so far, and are also describing very well the published KamLAND data. Therefore the $\alpha_{i,sim}$ from this study were used instead of those from the original KamLAND publication. A comprehensive list with the used α values for the individual isotopes can be found in the appendix Table A.0.1.

The following analysis of the scaling calculation results, as shown in Tab. 6.2.4, can be done. First of all, it is obvious that all values obtained by scaling measured cross-sections, and using the integral of the full muon energy spectrum, are systematically lower than with the usage of a mean energy. This is mainly due to the fact that the energy spectrum as shown in Fig. 6.1.1 is asymmetric towards lower energies and that the cross-sections are also smaller at lower energies (refer to Table A.0.1). Thus, using a mean muon energy overestimates the isotope yield. This is partly also the reason why the up-scaling of measured production rates from KamLAND and Borexino are resulting in much higher values. Furthermore they are across all isotopes very well consistent with each other, and the fact that they stem from actually measured data supports the prediction. Therefore a value of about $(1.14 \pm 0.2) \times 10^3 \text{ kt}^{-1} \text{ yr}^{-1}$ decays of ^{11}C , produced through in-situ muon spallation of ^{12}C in LAB, can be taken as an approximate upper limit for SNO+. This value will be compared to the results from simulations with the RAT software in the next section.

6.2.2 Simulations with RAT

To gain further information and to support the expectations on muon-induced backgrounds, additionally a study with the SNO+ simulation- and data analysis software

Table 6.2.4: Calculated production rates of the relevant muon-induced isotopes in SNO+, as presented in Tab. 6.2.1. The second and third column show the numbers that were derived by scaling the cross-sections measured in [Hag00] (in the table as σ -method), with a mean value approximation for the muon energy (6.14) and the integral muon energy distribution (6.13), respectively. The values in column four and five are gained by scaling the results obtained by the KamLAND [Abe10] and Borexino [Bel13a] experiments with the respective mean energy, muon flux and number of target atoms of SNO+.

isotope	R_i [kt ⁻¹ yr ⁻¹]			
	σ - mean E_μ	σ - integral E_μ	KamLAND	Borexino
⁶ He	10 ± 1	3 ± 1	—	46 ± 16
⁸ He	1.3 ± 0.2	—	1.1 ± 0.6	< 2
⁸ Li	2.5 ± 0.9	1 ± 1	16 ± 4	8 ± 7
⁹ Li	—	—	3 ± 0.3	3.6 ± 0.3
¹¹ Li	—	—	—	—
⁷ Be	140 ± 18	55 ± 15	—	—
¹¹ Be	1.5 ± 0.1	—	1.5 ± 0.4	< 8.5
⁸ B	4 ± 1	2 ± 1	10 ± 3	16 ± 6
¹² B	—	—	60 ± 5	69 ± 3
⁹ C	3 ± 1	—	4 ± 2	< 19
¹⁰ C	70 ± 10	24 ± 6	23 ± 3	22 ± 5
¹¹ C	560 ± 56	190 ± 30	1135 ± 200	1050 ± 120
¹² N	—	—	—	< 2

RAT has been performed. The Reactor Analysis Tool is widely based on the Geant4 software toolkit and was customised for the SNO+ experiment, i.e. the detailed detector geometry is implemented as well as models for the PMTs and their Winston cones, data acquisition, LAB properties and all other relevant details.

As it was pointed out earlier, the comparison of data and simulations indicates that especially the electromagnetic- and hadronic showers, that are induced by highly energetic muons, contribute significantly to the production of radioactive isotopes. A first strong indication was delivered by Galbiati et al. [Gal05] with ab-initio calculations and simulations and comparing those to measured cross-section data. Nevertheless, the most important study on this issue is presented by the KamLAND collaboration [Abe10], explicitly showing that for all measured isotopes the fraction of what is produced by showering muons is at least 60%. This is further supported by the simulation studies of Zbiri [Zbi10], showing that the consideration of secondaries, even in the vicinity of the detector, yields much better results in comparison with actual data.

With these findings in mind, a new physics list for hadronic interactions was implemented into RAT, in order to correctly account for the effects of showering muons. In [Bel13a], Bellini et al. present a very important and useful comparison of the simulation results with the actual measurements of Borexino for the relevant isotopes and neutrons, delivering a powerful benchmark for the Geant4 software. This study com-

pares four different physics list compilations and evaluates which models are most successful in describing the data. All combinations are systematically underestimating the isotope production by about 50 %, and the performance of these lists varies for the different isotopes. On the other hand, neutron production is well predicted by most models. The best overall combination was adapted for the use in RAT and Tab. 6.2.5 gives an overview of the used models in the respective energy range for the relevant particle types. An extensive description of the models and their individual advantages can be found in the Geant4 physics reference manual [Gea].

Table 6.2.5: List of hadronic physics models implemented in RAT in order to correctly predict isotope production in muon-induced hadronic showers. The model abbreviations are: HP = High precision neutron model, Bertini = Bertini cascade model, LEP = Low Energy Parametrised model, QGS = Quark-Gluon String model (here combined with the pre-compound model) and 'generic' refers to the standard Geant4 model for these energies. A thorough description of the models is given in [Gea].

energy	protons	neutrons	π^\pm & K^\pm
elastic			
< 4 eV	generic	HP thermal	generic
4 eV \rightarrow 20 MeV	generic	HP elastic	generic
inelastic			
0 MeV \rightarrow 20 MeV	generic	HP	generic
20 MeV \rightarrow 10 GeV	Bertini	Bertini	Bertini
10 GeV \rightarrow 100 TeV	QGS	QGS	QGS

With these prerequisites, a number of about 23 k muons, approximately the amount that passes through SNO+ in one year, has been propagated through the detector with the RAT software, and the following observations were made.

First of all, the production rates for the generated isotopes can be found in the following Table 6.2.6. As expected, the amount of produced ^{11}C is the highest for all isotopes, but likely underestimated as it has been consistently seen in previously reported simulations by Borexino [Bel13a] and KamLAND [Abe10]. Both compare their actual measurements to the simulations and find that both, Geant4 and FLUKA, underestimate the ^{11}C production by 50 %. This is also the case for most other isotopes, with only a few exceptions e.g. the ^{10}C data is represented with about 15 % less events in the those simulations. Table 6.2.6 shows a comparison of the production rates from this RAT simulation campaign and the simulated rates as reported by Borexino and KamLAND. The most interesting value for ^{11}C is about a third of that reported by the others and about a tenth of what is expected via the scaling calculations, listed in Tab. 6.2.4. When taking the mentioned discrepancy of the other groups into account, SNO+ would actually have to expect about 200 ^{11}C events per kilotonne and year, judging from these simulations. However, when choosing a conservative approach, the numbers from the scaling calculations should be used and the SNO+ collaboration can be optimistic that the final numbers will be smaller.

Table 6.2.6: Production rates of radioactive isotopes as **simulated** in this work (first column), by Borexino [Bel13a] (second column) and KamLAND [Abe10] (third column). Borexino and this work used a Geant4 based simulation software with an adapted hadronic physics list as reported in [Bel13a]. KamLAND used the FLUKA simulation software. The uncertainties for the values obtained in this work are purely statistical.

isotope	R_i [kt ⁻¹ yr ⁻¹] SNO+	R_i [kt ⁻¹ yr ⁻¹] Borexino	R_i [kt ⁻¹ yr ⁻¹] KamLAND
⁶ He	-	7 ± 0.3	9 ± 0.5
⁸ He	-	0.2 ± 0.05	0.3 ± 0.05
⁸ Li	4.5 ± 1	-	17 ± 1
⁹ Li	2.5 ± 1	1.3 ± 0.1	2.5 ± 0.2
¹¹ Li	-	-	-
⁷ Be	20 ± 4.5	-	82 ± 5
¹¹ Be	-	0.4 ± 0.1	0.7 ± 0.1
⁸ B	4.5 ± 2	1 ± 0.1	4.5 ± 0.3
¹² B	13.5 ± 3	18.5 ± 0.5	22 ± 2
⁹ C	2.3 ± 1	0.8 ± 0.1	1 ± 0.1
¹⁰ C	16 ± 4	32 ± 1	15 ± 1
¹¹ C	127 ± 10	324 ± 21	325 ± 21
¹² N	2.3 ± 1	2.4 ± 0.2	0.6 ± 0.06

Beside the amount of muon-induced backgrounds, also their movement inside the AV and the lateral distance to the muon track at their production are insightful values. The distribution of the length of the ¹¹C path is gaussian shaped around a mean of 3.5 μm in this simulation. This is an important value as it is a main prerequisite for the reduction technique presented in the next section. Even though this is probably a number too small under realistic conditions, the assumption that the produced isotopes do not move much inside the liquid scintillator seems well justified, as measurement with ²²²Rn show [Shi03] that the radon moved less than one meter in its mean life of 5.5 days. Figure 6.2.1 shows the distribution of the distance to the muon track at which ¹¹C is produced, which is very similar for the other isotopes. The majority of the carbon is produced within the first 10 cm around the track, falling off slowly towards 1 m, after which the production is negligible. The overall mean distance is $\langle d(\mu - {}^{11}\text{C}) \rangle \simeq 40$ cm.

The neutrons produced associated with the carbon spallation are obviously also very important, especially for the triple-coincidence technique presented in the next section. These neutrons are dominantly produced by photo-neutron reaction at a giant dipole resonance of ¹²C at 23 MeV [Gal05]. Therefore they are generated with significantly less energy and thus their range is much smaller compared to other neutrons produced in the electromagnetic- and hadronic showers. The range distribution for neutrons from the ¹¹C production is shown in Fig. 6.2.2 and their average range is found in these simulations to be $\langle R_n \rangle \simeq 40$ cm.

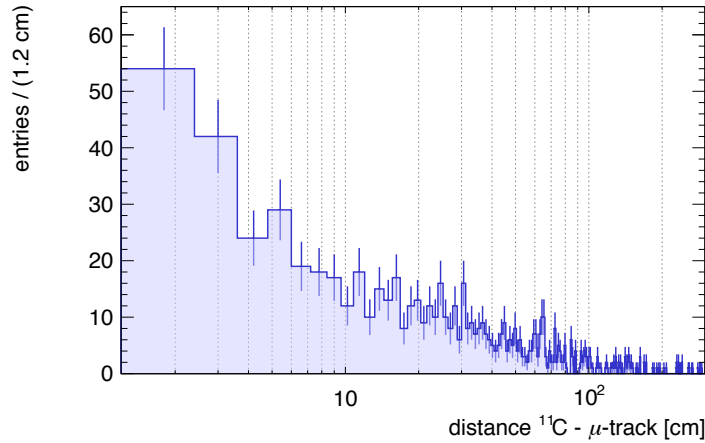


Figure 6.2.1: Distribution of the distance of muon-induced ^{11}C (creation point) to the muon track. Clearly, most of the production happens within 10 cm of the muon track, whereas it is negligible beyond 1 m.

6.2.3 ^{11}C background reduction technique

In the last section it was pointed out that 95% of the ^{11}C production processes involve a neutron in the final state. It was also shown that those neutrons have a range distribution according to Fig. 6.2.2 and a mean path length inside the LAB of $\langle R_n \rangle = 40$ cm. These neutrons are identified by the muon + 2.2 MeV- γ coincidence. The spatial reconstruction uncertainty for these γ -rays is about 10 cm in SNO+, and therefore good enough to construct a spherical veto-volume around the reconstructed neutron site, to account for its initial movement from its actual production point. Ideally this sphere has a radius r that is several times the mean neutron path length $\langle R_n \rangle$. This allows then to veto all events from this volume within a certain time, ideally several of the ^{11}C lifetimes $\tau(^{11}\text{C}) = 29.4$ min. At the latest by now, it becomes very clear that this spherical volume cut is of great importance, since a veto time for the whole detector of ~ 300 min after each muon + 2.2 MeV- γ coincidence would significantly reduce the fiducial mass-time of SNO+. Before discussing the efficiency of such a spherical volume cut in detail, it shall be mentioned that this technique might be improved by the usage of a reconstructed or measured muon track. In case a well reconstructed muon track is available, the spherical veto-volume might be further reduced to the intersection of this sphere with a cylindrical volume around the muon track. This situation is depicted in Fig. 6.2.3, and this technique was initially proposed by [Fra05].

The efficiency for a spherical volume cut around the reconstructed neutron position is composed of two components: one is describing the size of a sphere with radius r , and therefore the effectiveness $\zeta(r)$ of including the ^{11}C atom, and one is concerning the time window t in which the carbon β -decay is expected inside this volume, hereafter $\eta(t)$. Thus the total efficiency ε is

$$\varepsilon = \zeta(r) \cdot \eta(t) \quad (6.17)$$

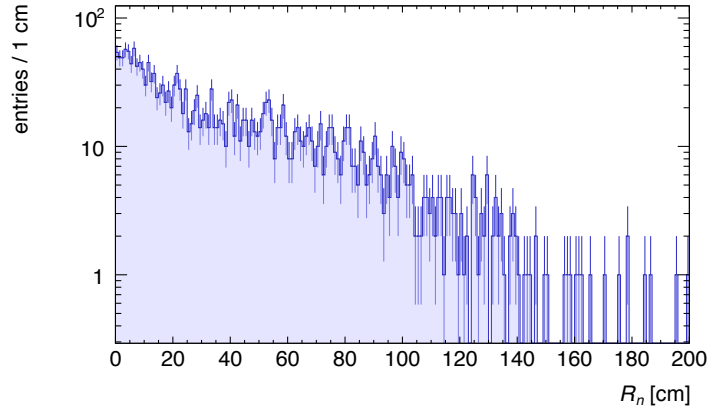


Figure 6.2.2: Distribution of the muon-induced neutron range R_n for neutrons associated with ^{11}C production. The path length is reduced due to the lower energy of these neutrons, caused by their production reaction.

As the ^{11}C decays exponentially with a lifetime constant $\tau(^{11}\text{C}) \approx 30$ min, the efficiency of including all decays in the time window t can be considered as

$$\eta(t) = 1 - e^{-t/\tau} \quad (6.18)$$

Furthermore, considering the lateral distribution of neutrons from their creation point $f_n(x)$, as found in the RAT simulations and presented in Fig. 6.2.2, the spatial efficiency component can be calculated via

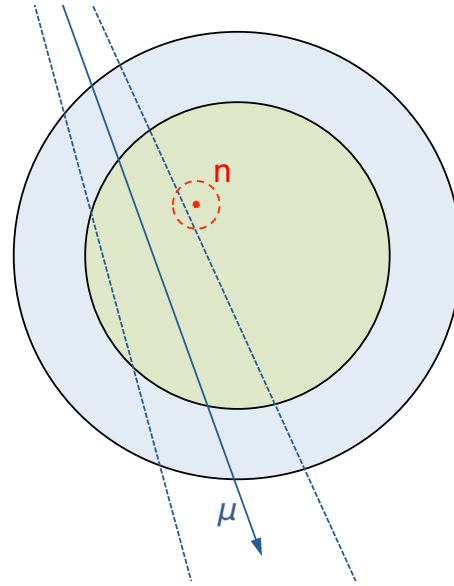
$$\zeta(r) = \frac{\int_0^r f_n(x) dx}{\int_0^\infty f_n(x) dx} \quad (6.19)$$

Obviously these efficiencies are maximised when increasing the radius r and time t , and sensible values for those variables can be derived considering the signal (S) to background (B) ratio $R = S/B$ for a desired observable and mass-time fraction loss L , defined the following way, [Gal05]. Firstly R can be estimated as

$$R = \frac{S/B_0}{F + (1-F)(1-\varepsilon)} \quad (6.20)$$

where the Signal rate S can be for example the amount of expected **solar pep and CNO neutrinos** in a respective energy window, in this case [0.8,1.3] MeV. B_0 is then the 'raw' number of background events in this energy region, without any cuts applied. For this example the more conservative value for ^{11}C decays from the scaling calculations will be used. And $F \simeq 0.05$ accounts for the fraction of ^{11}C produced through 'untaggable' invisible channels without a neutron. This definition is of course a coarse simplification of the situation as it is neglecting all other possible backgrounds and concentrating solely on ^{11}C . For a fictional 100% efficiency ε , and a sum signal rate for pep and CNO neutrinos of 2.0 events per day in 100 tonnes of liquid scintillator [Gal05], the signal to background ratio in SNO+ would then be 112/1.

Figure 6.2.3: Schematic 2D-drawing of a muon track (solid blue arrow) and a volume around it (dashed blue lines), based on the track reconstruction. The different reconstruction uncertainties for the entry- and exit point of the muon will be explained in the following section, and result in a volume of ‘truncated cone’-shape. The red dashed circle shall illustrate the uncertainty on the neutron position due to its movement from the creation point (red point). The green and blue circles represent the acrylic vessel, filled with liquid scintillator, and the PSUP, filled with water, respectively.



This is of course constraint by the finite coincidence time window and radius of the sphere, which is expressed in the mass-time fraction loss L which is describing the lost mass \times time, due to the spherical cut around the neutrons identified in the muon + 2.2 MeV- γ coincidence [Gal05]:

$$L = 1 - e^{-4/3 \pi r^3 \rho t N} \quad (6.21)$$

with ρ as the scintillator density and N the neutron rate per unit mass and time fraction. Using these equations, an example calculation illustrates the very good prospects of SNO+ using this technique. With a time window of 300 min, a radius of 80 cm for the neutron sphere, the efficiency is $\varepsilon \approx 85\%$. This is leading to a signal to background ratio of $R \approx 6.5$, under the assumption of 2.0 /d/100 t pep and CNO neutrinos in the energy window of [0.8,1.3] MeV [Gal05] and an ^{11}C rate of 0.356 /d/100 t, which is the conservative upper limit from the scaling calculations of 1300 events/yr/kt. This corresponds to a mass-time fraction loss of $L < 1\%$.

6.3 Track reconstruction

In the last part of the last section, it has been shown how information about the muon track can be beneficial in reducing volume cuts in case of muon-induced ^{11}C production. In this section, the for this work implemented muon reconstruction will be explained in detail.

Since several large scale spherical shaped, water- and liquid scintillator experiments necessarily had to deal with muons (KamLAND, Borexino, SNO, Super-Kamiokande), a first logical step was to review the work that already had been done by others. From studying the available documentations, it became clear that mainly two types of track reconstructions are in use, or were used, by other comparable experiments. These are always either evaluating light patterns with analytical

approaches and functions or making use of a likelihood minimisation in a more statistical manner. As it is not possible to judge on the performance of either technique a priori, in a particular case, practical considerations have to be taken into account.

In the latter case, typically a large number of muon events is simulated with the respective software and so-called 'look-up tables' are generated for these. With simulating as many different inclinations and radii as possible, a library of events is generated that tries to include all probable muon tracks, or at least as many as are possible. For these simulated events, the PMT hit times are stored in a large database and later compared to real events. A minimisation routine finds the most likely simulated track for a PMT hit time pattern generated by a real event, and calculates an approximate path. This is then the reconstructed muon track. As this technique requires a lot of computing power to generate and store the very complex look-up tables (e.g. in the case of SNO several 100 MB), the analytical approach was chosen for this thesis, and will be explained hereafter.

The muon events in SNO+ can be classified into four main categories. To illustrate this geometrical classification, Fig. 6.3.1 shows the possible muons paths in the detector and its vicinity. Starting from the outside, muons are passing by the detector entirely in the rock surrounding the cavity ((1) in Fig. 6.3.1) are obviously of no importance for any track reconstruction, though they might produce neutrons which could enter the cavity and influence the experimental background.

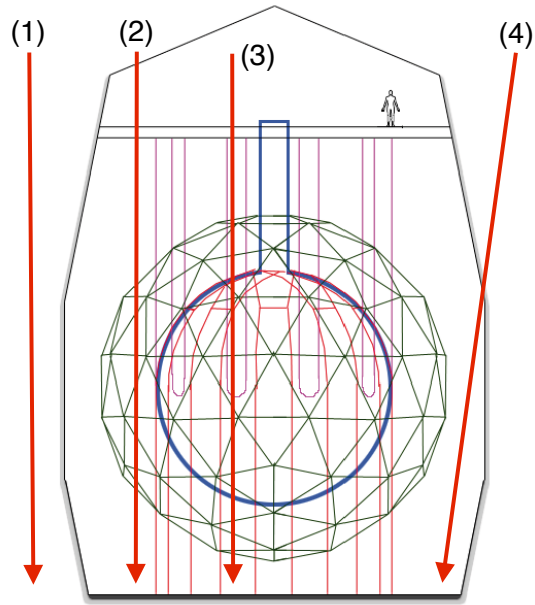
For muons passing through the water shielding outside the PSUP (4), basically the same can be said, except that they are potentially more dangerous in terms of background event generation. As they are actually going to be detected through the OWL PMTs by their Cherenkov light, a coincidence with detected background events inside the PSUP might give a figure of merit how many neutrons (produced by these muons) are passing through the water shielding, towards the inside of the setup.

The third category are muons entering the inside of the PSUP, but not the AV (2). While they are not in contact with the liquid scintillator, they only produce Cherenkov light and will be hereafter called '**water-only**' events. Again these are creating backgrounds while hitting water molecules, and especially the induced neutrons might travel significant distances.

All the other muons interact with the liquid scintillator and are creating both, Cherenkov- and scintillation light (3). Since the light creation and propagation is very different, the PMT hit time patterns for such events differs significantly from the aforementioned. This demands adapted fitting algorithms, different for the latter two event topologies, upon which the focus will be laid in the following sections. From simply calculating the geometrical cross-section for muons with the inner SNO+ detector, one can estimate that half of the muon events will be water-only- and the other half will be scintillator events, not considering muons outside the PSUP.

In the preceding SNO experiment, the muon trigger condition was developed experimentally and can be summarised the following way. For an event to be tagged as muon event, at least 5 OWL tubes need to be hit and the time between two OWL events must not be longer than $5 \mu s$. Furthermore the amount of normal, inward facing PMTs that register at least one hit (N_{hits}) has to be at least 150. Especially

Figure 6.3.1: Drawing of the SNO+ detector with the four possible muon topologies. Those only passing through the rock surrounding the cavity (1), as well as muons going through the water shielding outside the PSUP (4). Relevant for the track reconstruction are ‘water only’ muons inside of the PSUP but outside the acrylic vessel (2) and those interacting with the liquid scintillator (3). A detailed description of the detector can be found in chapter 3. Taken from [And16].



this last number probably has to be reduced for SNO+, as the light yield of the liquid scintillator is much higher than that of Cherenkov radiation in water. Also a more technical issue has to be addressed once SNO+ is actually filled with liquid scintillator. The so-called neck of the detector connects the acrylic sphere with the deck above the detector cavity (refer to Fig. 6.3.1). This creates a light leak on the upper end of the PSUP, and light that was produced inside the PSUP might hit OWL PMTs. Therefore some restriction on the amount of photomultiplier tube hits in the vicinity of the neck and their timing with respect to the OWL hits will be used for a ‘neck event’ veto. This rather simple combination of hit numbers of outward looking PMTs and normal PMTs proved to be extremely efficient in tagging muon events for the SNO experiment. With small adjustments, a similar performance can be expected for SNO+.

Once an event is tagged as muon-like, this version of the muon fitting algorithm applies an event classification considering two variables, N_{hits} and the total collected charge of all hit PMTs, hereafter denoted with Q_{tot} . For both variables, the distribution against the impact parameter b (shortest distance of the track to the origin of the sphere) of the muons can be seen in Fig. 6.3.2 and Fig. 6.3.3, respectively. The dependence of N_{hits} on the impact parameter is strongly pronounced, so that a cut demanding at least 9000 PMT hits, already selects muon tracks inside the AV ($b < 6$ m) very efficiently. In a simulation set of about 15.5 k muons, this one variable cut mis-classifies only 35 muons as scintillator events, even though their track is actually outside the AV, yielding an efficiency of already 99.77%. Furthermore, when combined with a second criteria for the charge, e.g. demanding $Q_{\text{tot}} > 6 \times 10^6$, the efficiency reaches 99.90%, and therefore a satisfactory level.

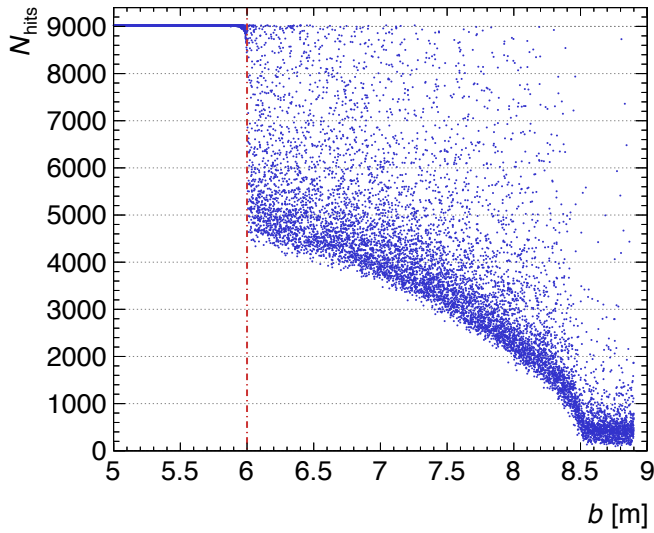


Figure 6.3.2: Distribution of N_{hits} versus the impact parameter b of ≈ 15 k simulated muon tracks. The size of the acrylic vessel is not only very well visible through the shape of the distributions but also marked with by red dash-dotted line.

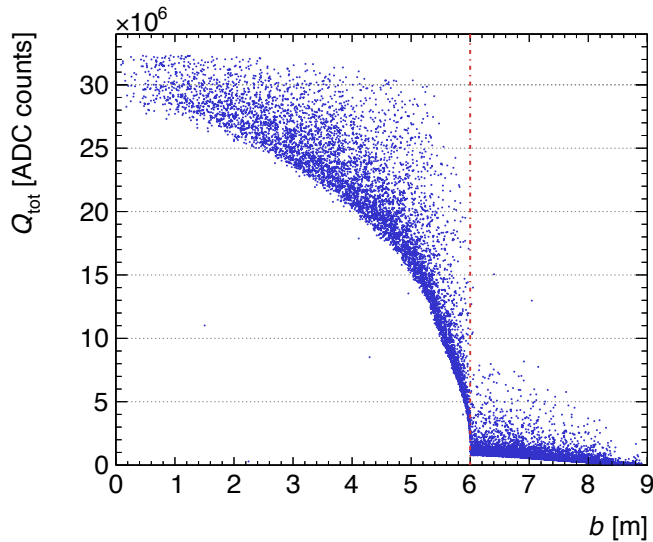


Figure 6.3.3: Distribution of the total collected charge Q_{tot} versus the impact parameter b of ≈ 15 k simulated muon tracks. The size of the acrylic vessel is marked with by red dash-dotted line.

6.3.1 Track reconstruction for muons only in water

As already mentioned in the introduction of this section, muons passing only through the water envelope of the acrylic vessel (AV) are expected to produce a small amount of fast neutrons (refer to section 6.2) and make up about half of the events that are interesting in terms of a track reconstruction.

Even though the optical properties, paths and reflections of photons are very different in this detector setup compared to the entirely water filled SNO, the old analytical track reconstruction algorithm from SNO proved to be a useful starting point. The analytical methods presented hereafter were used as a fitter 'seed' for a fully-fledged likelihood track reconstruction in the SNO experiment. Nevertheless the performance is likely to be good enough for a water-only muon fitter in SNO+.

All analytical methods commonly search for entry point (EP) and exit point (XP) of the muon track in the photomultiplier structure. Since the probability of a signi-

ficant scattering of the muon during its passage is negligible, those two points define a muon track.

The **entry point** reconstruction starts by selecting the first 80 PMT hits and calculating the geometrical centre of their coordinates. Once the first centre is calculated, a second criteria is applied. Now the first 20 PMT hits with an angle Θ smaller than 26° ($\cos \Theta > 0.9$) between the hits and the centre are selected. The reconstructed EP coordinates are then again calculated as the barycentre of those hits.

The **exit point** is computed in a similar way. Here, the fitter calculates the vector pointing towards the reconstructed XP (\vec{V}_{XP}) via the charge weighted barycentre of all hit PMTs, see Equation 6.22.

$$\vec{V}_{XP} = \frac{\sum_{\text{PMT}} (Q_{\text{PMT}} \cdot \vec{X}_{\text{PMT}})}{\|\sum_{\text{PMT}} (Q_{\text{PMT}} \cdot \vec{X}_{\text{PMT}})\|} \quad (6.22)$$

where \vec{X}_{PMT} is the vector pointing from the origin of the detector (centre of the sphere) to the individual PMT and Q_{PMT} s the respective charge collected on the PMT. This can only be done if the muon does not interact with the scintillator, since the very large amount of light produced in that case distorts the charge information from the PMTs [Bel11]. In the case of an entirely water filled detector or a muon passing only through the water outside the AV, the collected charge is a valuable and reliable information.

The performance of this method was tested in dedicated Monte Carlo simulation campaign with the RAT analysis software for SNO+, and the results will be presented in section 6.3.3.

6.3.2 Track reconstruction for muons in liquid scintillator

Once a muon interacts with the liquid scintillator, the situation becomes unequally more difficult. The generated light is now composed of Cherenkov- and scintillation light and propagates in an ice-cream cone-like shape. At the end, a 'ball' of isotropically radiating scintillation and in front a tip of Cherenkov light. Until recently, the common belief was that the scintillation light in LAB will always outshine the Cherenkov component and that therefore the latter can not be used to retrieve a directional information. Simulation studies by the SNO+ collaboration also found that the signal from the Cherenkov component would be too weak, at least for neutrino-induced electrons and those from beta decays. Just very recently, Li et al. [Li15] at BNL found experimentally that at least in the case of muons, the Cherenkov component can actually be separated by a pulse shape analysis. As this was unknown at the time this reconstruction was implemented, it only makes use of this fact in an indirect manner, that will be explained in the following description.

As mentioned earlier, an analytical approach was chosen to reconstruct muon tracks in SNO+ LAB. This method is heavily inspired by the algorithm that was developed by the Borexino collaboration and is well documented in [Bel11]. The following description shall lay out how these principles are implemented for a SNO+ muon fitter.

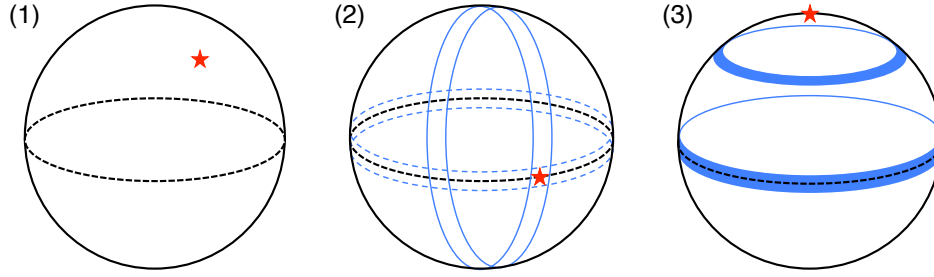


Figure 6.3.4: A scheme illustrating the rotations and selections of PMT coordinates for the muon track entry- and exit point reconstruction. On the left **(1)**, an initial first guess of the EP in normal detector coordinates. In the middle **(2)**, the EP rotated to the equator with the select PMT bands in the ϑ' -plane (solid blue lines) and the φ' -plane (dashed blue lines). And on the right **(3)**, the EP is shifted to the 'north pole' and the selected φ'' -planes are shown with filled blue areas.

The **entry point** reconstruction starts by selecting the PMT hits in a time window of 30 ns after the first hit of an event, and by calculating the geometrical barycentre, resulting in a first guess for the EP position. This is illustrated by part **(1)** in the graphical representation in Fig. 6.3.4. With those coordinates, a rotation \mathcal{R}_{EP} is defined to transform the position of all PMTs, so that the coordinates of the first guess for the EP are shifted to the 'equator'. This helps avoiding topological effects at the poles. Now two 'bands' of PMTs around the guessed EP coordinates are selected, one in the equatorial plane and one perpendicular to it, **(2)** in Fig. 6.3.4. The width of those bands is crucial to the success of the consequent fitting. Starting with a size that incorporates two to three rows of PMTs, the width is incremented step by step until the best fit results are achieved. The PMT hit time patterns in the selected φ' - and ϑ' -planes are of V-like shape due to the geometry of two intersecting spheres, the PSUP and the scintillation light ball. Therefore the patterns are fitted with a two-sided trigonometric function

$$t(\varphi') = a^0 + \begin{cases} a^- \cdot \sin(c^- (\varphi'_e - \varphi')) & \text{if } (\varphi' < \varphi'_e) \\ a^+ \cdot \sin(c^+ (\varphi' - \varphi'_e)) & \text{else} \end{cases} \quad (6.23)$$

where t is the PMT hit time, φ' is the rotated φ coordinate, a^0 the entry time offset and a^+ , a^- , c^+ and c^- are the parameters for the left and right side of the split sine function. The resulting φ'_e and ϑ'_e coordinates can then be transformed to the original coordinate system by the inverse rotation $\mathcal{R}_{\text{EP}}^{-1}$, yielding a vector \vec{V}_{EP} pointing to the reconstructed EP. Examples of good fits for the EP reconstruction in the rotated coordinate system can be found in Fig. 6.3.5 and Fig. 6.3.6, showing nicely the V-like shape of the PMT hits in the selected ϑ' - and φ' -planes. Great care is taken to make sure that there are always enough PMT data points used and that the fits converge to the global minimum in a reliable manner.

The **exit point** reconstruction is somewhat more complex and requires several fits. First, a new rotation is calculated and performed, that shifts all coordinates in such a way that the EP is moved to the 'north' pole of the detector, as if the muon would have entered the detector at the very top of the sphere. This allows then nine

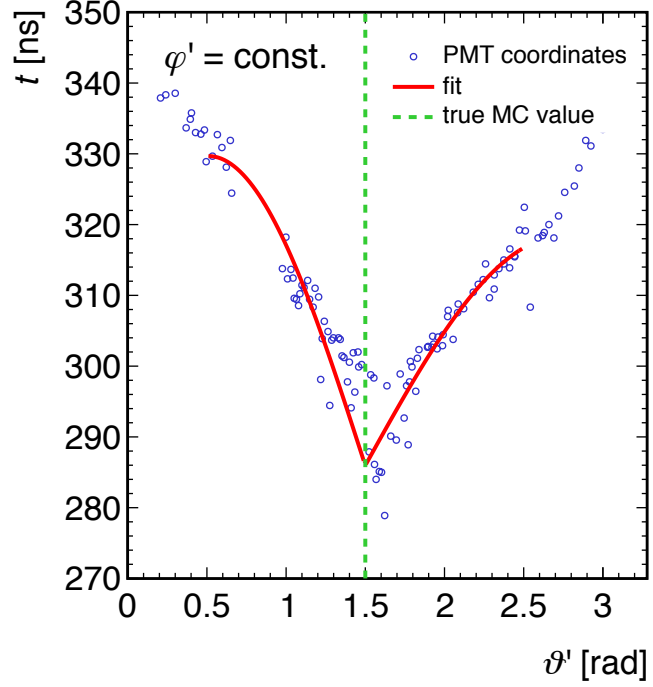


Figure 6.3.5: Fit of function 6.23 (red solid line) to the selected PMT coordinates (hollow blue dots) in the rotated ϑ' -plane (see (2) in Fig. 6.3.4). The green dashed line shows the true entry point of the simulated muon, in the rotated coordinate system, which is in this example matching the fitted ϑ'_e value very well.

'slices' of PMTs to be selected in increasing distance from the north pole, refer to (3) in Figure 6.3.4. The automated fitting of those slices with a cosine-like function is challenging and the original method in [Bel11] had to be simplified, in order to achieve a reliable convergence of all fits. This function is inspired by the expected PMT hit time distribution if the muon track crosses the planes exactly perpendicularly:

$$t(\vartheta'') = \frac{\sqrt{r_s^2 - 2r_s \cdot \cos(\vartheta'' - \varphi_x'')}}{c} + t_0 \quad (6.24)$$

with r_s as the radius of the PSUP, c the speed of light and t_0 the time offset to the case of an exactly perpendicular crossing of a muon. For each slice, a fitting very similar to the approximation routine for the EP reconstruction is applied, and the variable $\varphi_x''^{(i)}$ is extracted for each slice i . At the end, the mean from all nine $\varphi_x''^{(i)}$ values is calculated and weighted by their individual 'goodness of fit' (χ^2/dof). This $\langle \varphi_x'' \rangle$ can then be used to find the so-called symmetry plane. This plane (hereafter P_{exo}) is defined by the coordinates of the EP, the origin (O) of the coordinate system and the XP. A schematic representation is given in Figure 6.3.7. This final plane of PMTs can now be selected with the EP, $\langle \varphi_x'' \rangle$ and the origin, and ideally it will contain the XP. Since the muons in SNO+ will travel faster than the speed of light in the scintillator, the tip of their Cherenkov light cone produces a kink in the hit time distribution of the PMTs in P_{exo} . In order to find this sometimes weakly pronounced kink, the distribution is first fit with the following double gaussian function to find the two peaks surrounding this minimum:

$$t(\vartheta'') = \frac{S_1}{\sigma_1} \cdot e^{-\frac{1}{2} \left(\frac{\vartheta'' - \mu_1}{\sigma_1} \right)^2} + \frac{S_2}{\sigma_2} \cdot e^{-\frac{1}{2} \left(\frac{\vartheta'' - \mu_2}{\sigma_2} \right)^2} \quad (6.25)$$

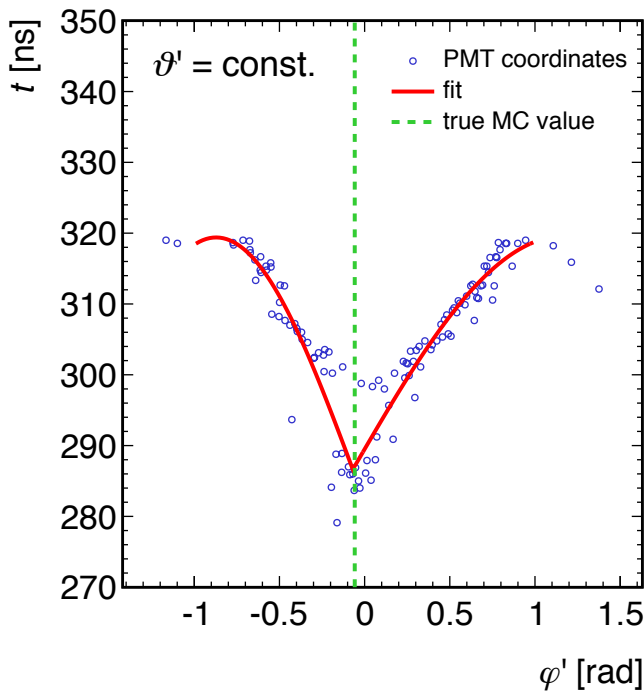


Figure 6.3.6: Fit of function 6.23 (red solid line) to the selected PMT coordinates (hollow blue dots) in the rotated φ' -plane (see (2) in Fig. 6.3.4). The green dashed line shows the true entry point of the simulated muon, in the rotated coordinate system, which is in this example very well matched by the reconstructed φ'_e value.

with t again as time and S_1 and S_2 as individual strength parameters.

Once this is achieved, Equation 6.23 is used again to perform the fit of the kink in between μ_1 and μ_2 . This last fit is shown in an example in Fig. 6.3.8 and proved to be the most difficult, since the sought-after local minimum in the distribution is sometimes very weakly pronounced. The quality of P_{exo} , and therefore the strength of the manifestation of this dip, depends on the quality of all the previous fits. Thus the main weakness of this track reconstruction is the strong dependence in the fitting chain. Small deviations at the beginning will result in large mis-reconstructions for the exit point. This effect is clearly visible in the uncertainties that will be presented in the next section. The here presented example fits stem from an extraordinary well reconstructable event, with deviations for the entry- and exit point coordinates of only $\Delta\Theta_{EP} = 1.25^\circ$ and $\Delta\Theta_{XP} = 1.57^\circ$.

6.3.3 Results

The performance of the implemented muon track reconstructions has been tested in a simulation of ≈ 23 k muon events, using the RAT software framework, the results are summarised in Table 6.3.1 and can be interpreted the following way.

Firstly, once the event is classified into either water-only- or scintillator muon, the performance of the respective track reconstruction algorithms depends strongly on the impact parameter of the incident muon. This is visualised in Fig. 6.3.9 and a simplified conclusion is that the reconstruction is more reliable when the radius (impact parameter) is small and the muon track has a certain distance to the boundaries of either the AV or the PSUP.

Figure 6.3.7: The symmetry plane P_{exo} (shaded orange area) is defined by the entry point (EP), the origin of the coordinate system (O) and the exit point (XP) of the muon track (solid blue line). Once φ_x'' is found, one can select a slice of PMTs around it and fit the resulting hit time pattern to approximate θ_x'' , as the final part of the XP coordinates. Taken and modified from [Bel11].

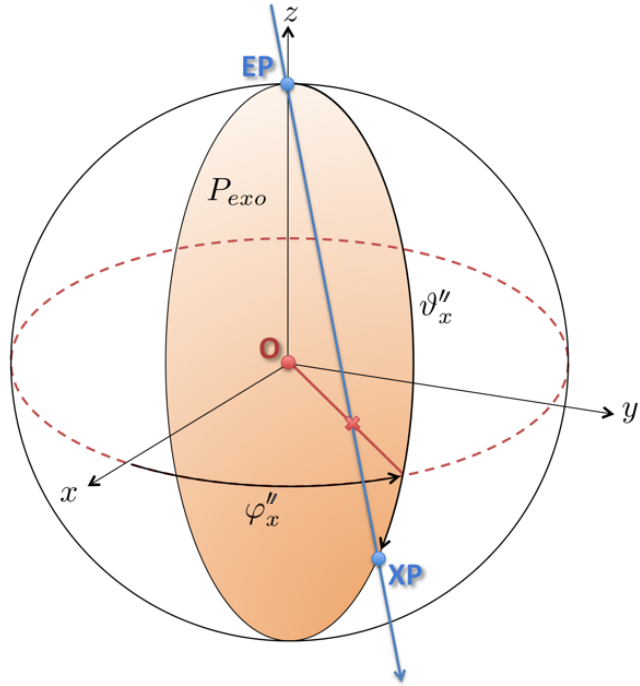


Table 6.3.1: Performance test results of the muon track reconstructions algorithms.

The average mis-reconstruction is calculated from ≈ 23 k muon events simulated with the SNO+ RAT software. Uncertainties are the standard deviation from the mean. To emphasise the different methods, the cells containing the results from water-only muons are shaded grey.

$b < \dots$ [m]	3	5	5.5	6	8	8.8
$\langle \Theta_{mis}(EP) \rangle [^\circ]$	1 ± 0.5	3 ± 1	4 ± 1	5 ± 1	8 ± 1	13 ± 1
$\langle \Theta_{mis}(XP) \rangle [^\circ]$	4.5 ± 0.5	13 ± 1	18 ± 1	23 ± 1	7 ± 1	17 ± 1

Inside the AV the EP accuracy is generally better than for the XP, which to some extent can be explained by the already mentioned fitting chain and the therefore strong dependence on starting values. For both, EP and XP, the mis-reconstruction increases when the track inside the AV gets shorter and the muon travels close to the AV boundary. Especially the exit point uncertainty steeply rises for $b > 5$ m, when EP and XP lie close together. Furthermore, a seemingly systematic structure for the exit points can be found on the left side of Fig. 6.3.9, thus inside the AV. This likely stems from a minimisation problem when fitting the P_{exo} plane.

For water-only tracks inside the PSUP but outside the AV, a similar trend for the EP mis-reconstruction can be observed, refer to the blue points in Fig. 6.3.9. This is not surprising since the basic concept inside the scintillator and outside the AV are the same for the EP reconstruction, namely fitting early PMT hit times. On the other hand, the XP uncertainties are decreasing strongly towards an impact parameter of 8 m, which is then followed by a very steep rising mis-reconstruction towards the PSUP boundary at 8.8 m.

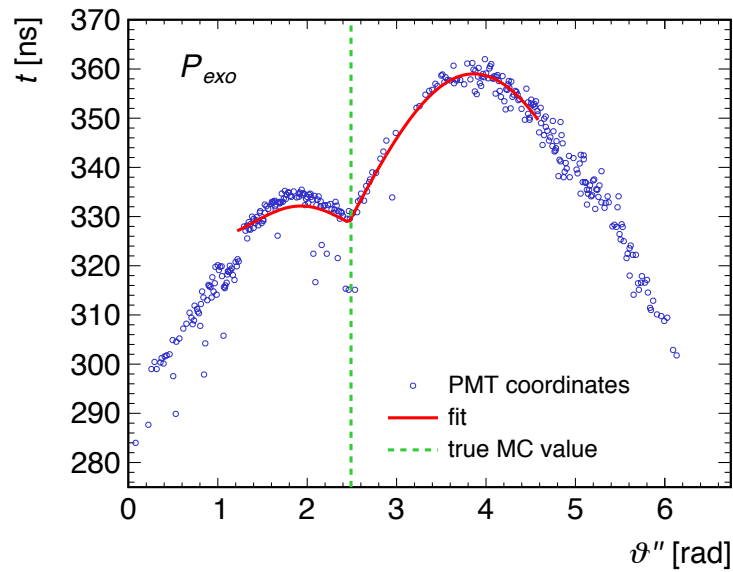


Figure 6.3.8: Final fit of the PMTs in the P_{exo} plane. The local minimum, that is caused by the tip of the Cherenkov light cone of an exiting muon, is in this example strongly pronounced and therefore well approximated with Eq. 6.23 (solid red line). The dashed green line marks the true θ_x'' coordinate of the simulated muon track.

Overall it can be said that for small impact parameters the mean mis-reconstruction is good for the EP but not great for the XP. Thus muons passing through the fiducial volume of SNO+ (depending on the phase) will likely be well reconstructed, but those with higher impact parameter have a much larger uncertainty. As already mentioned in the introduction to this chapter and section 6.2.3, in order to use the reconstructed track for an event-by-event reduction of the fiducial mass-time loss in case of a ^{11}C production, the uncertainty on the track position needs to be as small as possible. Due to the large uncertainties involved with this tracking algorithm, it seems not beneficial to use it for this application, especially without an external muon tracker.

A comparison of the track reconstruction performance with other liquid scintillator experiments is difficult since all of them use an external hardware tracker that greatly improves their accuracy and the reported numbers, if any, always refer to the global tracking. As one example, Borexino reports an angular resolution of $3^\circ - 5^\circ$ in [Bel11], which is obviously much better than what can be achieved with this implementation of the same method, but without an external muon tracker.

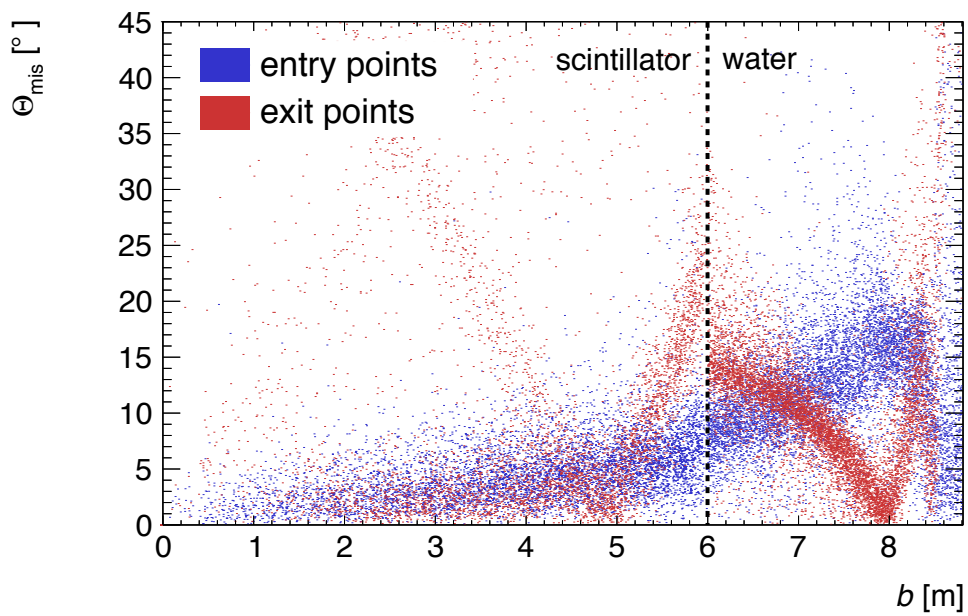


Figure 6.3.9: Mis-reconstruction of ≈ 23 k simulated muon events in SNO+, dependent on the impact parameter of the track. The entry point (blue) and exit points (red) are split into two areas by the dashed black line, marking the AV boundary and thus the change of the used reconstruction method.

CHAPTER 7

Conclusions

THIS work contributes with two parts to the upcoming SNO+ neutrino experiment. Firstly, the active medium of the SNO+ detector, a LAB based liquid scintillator mixture, will be cooled to about 12° C under operating conditions. As previous studies on the temperature behaviour of liquid scintillators are mainly qualitative and reliable data very scarce, this thesis was set out to shed more light into this subject.

In a small scale setup, LAB mixtures similar to those that will be used in SNO+, were cooled over a temperature range of -4° C to 30° C and observed by two PMTs in coincidence. The major challenge was to detect and control all unwanted changes that the temperature variations cause, such as a changing PMT sensitivity. Therefore a setup with a LED pulser that simultaneously emits light onto the PMTs and an external photodiode was built, and it could be shown that this is long time stable to $\pm 0.1\%$. With this control in place the changes of the scintillator light output were measured for signals from γ -ray emitting isotopes (and thus electrons) and α -particles that were dissolved into the LAB mixture. Generally, in agreement with observations of previous studies, a linear negative temperature coefficient was found. The combined value, averaged over all energies and the two particle types, is $(-0.29 \pm 0.01) \%/^{\circ}\text{C}$. Hints are found that electrons and α -particles have actually different values and those are $(-0.17 \pm 0.02) \%/^{\circ}\text{C}$ and $(-0.35 \pm 0.03) \%/^{\circ}\text{C}$, respectively. However this finding is not fully conclusive and further investigations on this particle type dependency are recommended. Furthermore, with decreasing temperature, a consistent increase in the slow decay component of the scintillation light pulse was observed via pulse shape analysis. Taking previous studies on the energy transfer processes in organic liquid scintillators into account, this points to a decrease of non-radiative de-excitations of triplet states of the aromatic scintillation molecules.

The second part of this work concerned muons and muon-induced backgrounds in the SNO+ experiment. Even though it is very well shielded against cosmic rays, SNO+ will have to deal with a cosmic ray muon rate of about 63 muons per day, at an approximate mean energy of 350 GeV. These muons will produce a variety of radioactive nuclides as well as highly energetic neutrons. As most of the induced isotopes have a rather short lifetime, a small veto time after each muon event will exclude most of them efficiently. This is feasible given the low event rate of muons at the SNOLab site. The two major remaining backgrounds are ^{11}C and neutrons.

Predictions for the ^{11}C production can be made by either scaling cross-sections or even production rate data to the respective muon characteristics for SNO+. Especially the from Borexino and KamLAND up-scaled production rates can be considered as conservative upper limit of about 1.3×10^3 decays/kt/yr. This value has been used to generate the ^{11}C β -spectrum in Fig. 3.3.1 and even though a significant reduction is desirable, it is most likely not a crucial thread to the solar (pep and CNO) neutrino signal of interest. Nevertheless a dedicated simulation campaign has been done, especially to investigate a mitigation strategy, involving a three-fold coincidence of muon detection, subsequent neutron capture and the final ^{11}C β^+ -decay. This triple coincidence will be very effective in tagging the ^{11}C decays in almost all cases,

depending on the chosen parameters for veto time, volume size and the connected mass-time fraction loss.

A further improvement of this technique involves the intersection of a sphere, accounting for the neutron movement, and a cylindrical volume around the muon track inside the detector. Unfortunately this track has to be generated in SNO+ via a reconstruction algorithm that is entirely based on Monte Carlo simulations and is therefore always less reliable as methods in comparable experiments, which are employing actual hardware trackers. The muon track reconstruction implemented in this work, performs reasonably well for smaller impact parameters, but worse at the boundaries of the acrylic vessel or PMT structure. Furthermore it shows some systematic uncertainties that emerge from the analytic nature of the algorithm. Another type of reconstruction might improve this situation. Therefore it is not recommended to use this track reconstruction for a fiducial volume cut in the case of ^{11}C events. Fortunately, at this point, it seems not necessary to do so.

List of power law exponents α

Table A.0.1: List of measured cross-sections σ and power law exponents α_{meas} for the isotopes produced via muon spallation of a ^{12}C target at a CERN SPS muon beam with the energies 100 GeV and 190 GeV [Hag00]. The values for α_{sim} are taken from [Abe10] and are generated by fitting production yields of the respective isotopes in Geant4 and Fluka simulations. Those denoted with an asterisk (*) are taken from [Zbi10], who included furthermore the production of the isotopes through secondaries and high energy muon-induced neutrons, also from a rock environment.

isotope	σ_{100} [μb]	σ_{190} [μb]	α_{meas}	α_{sim}
^6He	10.15 ± 1.0	16.02 ± 1.60	0.71 ± 0.22	$0.6819 \pm 0.0077^*$
^8He	—	(^9Li) 2.12 ± 0.35	—	0.926 ± 0.078
^8Li	2.93 ± 0.80	4.02 ± 1.46	0.50 ± 0.71	$0.5349 \pm 0.0211^*$
^9Li	—	(^8He) 2.12 ± 0.35	—	0.801 ± 0.026
^{11}Li	—	—	—	—
^7Be	127 ± 13	230 ± 23	0.93 ± 0.23	$0.5658 \pm 0.0005^*$
^{11}Be	<1.22 (68% CL)	<2.34 (68% CL)	—	0.753 ± 0.051
^8B	4.16 ± 0.81	7.13 ± 1.46	0.84 ± 0.45	$0.3151 \pm 0.1039^*$
^{12}B	—	—	—	0.828 ± 0.009
^9C	—	4.83 ± 1.51	—	0.772 ± 0.039
^{10}C	77.4 ± 4.9	115.4 ± 14.6	0.62 ± 0.22	$0.7621 \pm 0.0004^*$
^{11}C	576 ± 45	905 ± 58	0.70 ± 0.16	$0.6139 \pm 0.0001^*$
^{12}N	—	—	—	0.921 ± 0.045

Acronyms

α -NPO	2-phenyl-5- α -naphtyloxazole	47
ABS	acrylonitrile butadiene styrene	54
bis-MSB	1,4-bis(2-methylstyryl)benzol	38
BNL	Brookhaven National Laboratory	46, 77, 116
CAD	computer-aided design	52
CFD	constant fraction discriminator	57
CP	Charge-Parity	12
EC	electron capture	9
FADC	flash analog-to-digital converter	53, 63, 79
FKM	fluoroelastomer	54, 56
HZDR	Helmholtz Zentrum Dresden-Rossendorf	52, 78
IBD	inverse beta decay	18
IKTP	Institut für Kern- und Teilchenphysik	82
LAB	linear alkyl benzene	2, 38
LCAO	linear combination of atomic orbitals	34
LED	light emitting diode	53
LNGS	Gran Sasso National Laboratory	98
MC	Monte-Carlo	73
NIM	nuclear instrumentation module	53
PBD	2-phenyl-5-biphenyl-oxadiazole	47
PC	1,2,4-trimethylbenzene	38, 44
PET	positron emission tomography	34
PMT	photomultiplier tube	38, 52
POPOP	2,2-p-phenylene-bis-(5-phenyloxazole)	38

PPO	2,5-diphenyloxazole	25, 38, 45, 47
PRS	photoreactive surfactant	46
PSA	pulse shape analysis	79
PSUP	photomultiplier support structure	24
RAT	Reactor Analysis Tool	98, 105
ROI	Region Of Interest	14
SNEWS	supernova early warning system	20
SNO	Sudbury Neutrino Observatory	2
SNO+	SNO + liquid scintillator	2
SSM	Standard Solar Model	15
TMHA	3,5,5-trimethyl-hexanoic acid	45, 77
TUD	Technische Universität Dresden	78, 99

Bibliography

- [Aba91] A I Abazov et al. "Search for Neutrinos from the Sun Using the Reaction ${}^{71}\text{Ga} (\nu_e, e) {}^{71}\text{Ge}$ ". In: *Physical Review Letters* 67.24 (1991), p. 3332.
- [Abe08] S. Abe et al. "Precision measurement of neutrino oscillation parameters with KamLAND". In: *Physical Review Letters* 100 (2008), p. 221803. doi: [10.1103/PhysRevLett.100.221803](https://doi.org/10.1103/PhysRevLett.100.221803). arXiv: [0801.4589](https://arxiv.org/abs/0801.4589).
- [Abe10] S. Abe et al. "Production of radioactive isotopes through cosmic muon spallation in KamLAND". In: *Physical Review C* 81.2 (2010), p. 025807. doi: [10.1103/PhysRevC.81.025807](https://doi.org/10.1103/PhysRevC.81.025807).
- [Abe11] C. Aberle, C. Buck, F. X. Hartmann et al. "Light output of Double Chooz scintillators for low energy electrons". In: *JINST* 6.P11006 (2011).
- [Abe12] Y. Abe et al. "Reactor ν_e disappearance in the Double Chooz experiment". In: *Physical Review D - Particles, Fields, Gravitation and Cosmology* 86.5 (2012). doi: [10.1103/PhysRevD.86.052008](https://doi.org/10.1103/PhysRevD.86.052008). arXiv: [1112.6353](https://arxiv.org/abs/1112.6353).
- [Abe15] Y. Abe et al. "Muon capture on light isotopes in Double Chooz". In: (2015). arXiv: [1512.07562](https://arxiv.org/abs/1512.07562).
- [Aga13] N. Yu. Agafonova and A. S. Malgin. "Universal formula for the muon-induced neutron yield". In: *Physical Review D - Particles, Fields, Gravitation and Cosmology* 87.11 (2013). doi: [10.1103/PhysRevD.87.113013](https://doi.org/10.1103/PhysRevD.87.113013). arXiv: [1304.0919](https://arxiv.org/abs/1304.0919).
- [Agl87] M. Aglietta, G. Badino, G. Bologna et al. "On the Event Observed in the Mont Blanc Underground Neutrino Observatory during the Occurrence of Supernova 1987a". In: *Europhys. Lett.* 3 (1987), p. L1315. doi: [10.1209/0295-5075/3/12/011](https://doi.org/10.1209/0295-5075/3/12/011).
- [Agl89] M. Aglietta et al. In: *Nuovo Cimento C* 12 (1989), p. 467.
- [Agl99] M. Aglietta. "Measurement of the neutron flux produced by cosmic ray muons with LVD at Gran Sasso". In: *Proc. 26th Intern. Cosmic Ray Conf.* 2 (1999).
- [Ahm02] Q. R. Ahmad et al. "Direct Evidence for Neutrino Flavor Transformation from Neutral-Current Interactions in the Sudbury Neutrino Observatory". In: *Physical Review Letters* 81 (2002), p. 011301.
- [Ahn12] J. K. Ahn et al. "Observation of reactor electron antineutrinos disappearance in the RENO experiment". In: *Physical Review Letters* 108.19 (2012). doi: [10.1103/PhysRevLett.108.191802](https://doi.org/10.1103/PhysRevLett.108.191802). arXiv: [1204.0626](https://arxiv.org/abs/1204.0626).

- [Ale88] E. N. Alexeyev et al. "Detection of the neutrino signal from SN 1987A in the LMC using the INR Baksan underground scintillation telescope". In: *Physics Letters B* 205.2-3 (1988), p. 209. DOI: [10.1016/0370-2693\(88\)91651-6](https://doi.org/10.1016/0370-2693(88)91651-6).
- [Ali09] G. Alimonti et al. "The liquid handling systems for the Borexino solar neutrino detector". In: *Nuclear Instruments and Methods in Physics Research Section A: Accelerators, Spectrometers, Detectors and Associated Equipment* 609.1 (2009), pp. 58–78.
- [Alp] Alphalabs. *Ultrafast Photodetectors*. URL: http://www.alphalabs.com/images/stories/products/laser%7B%5C_%7Ddiagnostic%7B%5C_%7Dt ools/Ultrafast%7B%5C_%7DPhotodetectors%7B%5C_%7DUPD%7B%5C_%7DALPHALAS.pdf.
- [An12] F. P. An et al. "Observation of electron-antineutrino disappearance at Daya Bay". In: *Physical Review Letters* 108.17 (2012). arXiv: [1203.1669](https://arxiv.org/abs/1203.1669).
- [And16] S. Andringa et al. "Current Status and Future Prospects of the SNO+ Experiment". In: *Advances in High Energy Physics* 2016.9 (2016). arXiv: [1508.05759](https://arxiv.org/abs/1508.05759). URL: <http://arxiv.org/abs/1508.05759>.
- [Ant04] Pietro Antonioli et al. "SNEWS: The SuperNova Early Warning System". In: *New Journal of Physics* 6 (2004). DOI: [10.1088/1367-2630/6/1/114](https://doi.org/10.1088/1367-2630/6/1/114).
- [Ant97] P. Antonioli et al. "A three dimensional code for muon propagation through the rock: MUSIC". In: *Astroparticle Physics* 7.4 (1997), pp. 357–368. DOI: [10.1016/S0927-6505\(97\)00035-2](https://doi.org/10.1016/S0927-6505(97)00035-2). arXiv: [9705408 \[hep-ph\]](https://arxiv.org/abs/hep-ph/9705408).
- [Ara05a] T Araki et al. "Experimental investigation of geologically produced anti-neutrinos with KamLAND". In: *Nature* 436.7050 (2005), pp. 499–503. DOI: [10.1038/nature03980](https://doi.org/10.1038/nature03980).
- [Ara05b] H.M. Araújo et al. "Muon-induced neutron production and detection with GEANT4 and FLUKA". In: *Nuclear Instruments and Methods in Physics Research Section A: Accelerators, Spectrometers, Detectors and Associated Equipment* 545.1-2 (2005), pp. 398–411. ISSN: \. DOI: [10.1016/j.nima.2005.02.004](https://doi.org/10.1016/j.nima.2005.02.004).
- [Ara08] H. M. Araújo et al. "Measurements of neutrons produced by high-energy muons at the Boulby Underground Laboratory". In: *Astroparticle Physics* 29.6 (2008), pp. 471–481. DOI: [10.1016/j.astropartphys.2008.05.004](https://doi.org/10.1016/j.astropartphys.2008.05.004). arXiv: [0805.3110](https://arxiv.org/abs/0805.3110).
- [Arh09] B. Arhamim et al. "Measurement of the Cosmic Ray and Neutrino-Induced Muon Flux at the Sudbury Neutrino Observatory". In: *Physical Review D* 01 (2009), p. 17. DOI: [10.1103/PhysRevD.80.012001](https://doi.org/10.1103/PhysRevD.80.012001). arXiv: [0902.2776](https://arxiv.org/abs/0902.2776).
- [Arn11] R. Arnold et al. "Measurement of the $\beta\beta$ -Decay half-life of ^{130}Te with the NEMO-3 detector". In: *Physical Review Letters* 107.6 (2011). DOI: [10.1103/PhysRevLett.107.062504](https://doi.org/10.1103/PhysRevLett.107.062504). arXiv: [1104.3716](https://arxiv.org/abs/1104.3716).

- [Arp08] C. Arpesella et al. "Direct Measurement of the ^7Be Solar Neutrino Flux with 192 Days of Borexino Data". In: *Physical Review Letters* 101.9 (2008), p. 091302. DOI: [10.1103/PhysRevLett.101.091302](https://doi.org/10.1103/PhysRevLett.101.091302).
- [Bab95] K. S. Babu and R. N. Mohapatra. In: *Physical Review Letters* 75 (1995), p. 2276.
- [Bah05] John N. Bahcall, Aldo M. Serenelli and Sarbani Basu. "New Solar Opacities, Abundances, Helioseismology, and Neutrino Fluxes". In: *The Astrophysics Journal* 621 (2005), p. L85. DOI: [10.1086/428929](https://doi.org/10.1086/428929).
- [Bar13] J. Barea, J. Kotila and F. Iachello. "Nuclear matrix elements for double- β decay". In: *Physical Review C* 87.1 (2013), p. 014315.
- [Bel10] G. Bellini, J. Benziger, S. Bonetti et al. "Observation of geo-neutrinos". In: *Physics Letters B* 687.4-5 (2010), p. 299.
- [Bel11] G Bellini et al. "Muon and Cosmogenic Neutron Detection in Borexino". In: *Journal of Instrumentation* 6.5 (2011), p. 5005. DOI: [10.1088/1748-0221/6/05/P05005](https://doi.org/10.1088/1748-0221/6/05/P05005). arXiv: [1101.3101](https://arxiv.org/abs/1101.3101).
- [Bel13a] G Bellini et al. "Cosmogenic Backgrounds in Borexino at 3800 m water-equivalent depth". In: *J. Cosmol. Astropart. Phys.* 1308 (2013), p. 49. DOI: [10.1088/1475-7516/2013/08/049](https://doi.org/10.1088/1475-7516/2013/08/049). arXiv: [1304.7381](https://arxiv.org/abs/1304.7381).
- [Bel13b] G Bellini et al. "Measurement of geo - neutrinos from 1353 days of Borexino". In: *Physics Letters B* 722.4-5 (2013), p. 295. arXiv: [arXiv:1303.2571v1](https://arxiv.org/abs/1303.2571v1).
- [Bel14] G. Bellini et al. "Neutrinos from the primary proton-proton fusion process in the Sun". In: *Nature* 512 (2014), pp. 383–386. DOI: [10.1038/nature12702](https://doi.org/10.1038/nature12702).
- [Ber12] J. Beringer et al. "Review of Particle Physics (The Particle Data Group)". In: *Physical Review D* 86 (2012). DOI: [10.1016/j.physletb.2004.06.001](https://doi.org/10.1016/j.physletb.2004.06.001).
- [Bez73] L. B. Bezrukov et al. In: *Sov. J. Nucl. Phys.* 17 (1973), p. 51.
- [Bha03] G. Bhattacharyya et al. In: *Physical Review D* 67 (2003), p. 113001.
- [Bil12] S. M. Bilenky and C. Giunti. In: *Modern Physics Letters A* 27 (2012).
- [Bio87] R. M. Bionta et al. "Observation of a neutrino burst in coincidence with supernova 1987A in the large magellanic cloud". In: *Physical Review Letters* 58.14 (1987), pp. 1494–1496. DOI: [10.1103/PhysRevLett.58.1494](https://doi.org/10.1103/PhysRevLett.58.1494).
- [Bir51] J. B. Birks. "Scintillation from organic crystals: specific fluorescence and relative response to different radiations". In: *Proc. Phys. Soc. A* 64 (1951), p. 874.
- [Bir64] J. B. Birks. *The Theory and Practice of Scintillation Counting*. Pergamon Press Ltd., 1964.
- [Boe00] F. Boehm et al. "Neutron production by cosmic-ray muons at shallow depth". In: *Physical Review D* 62.9 (2000), p. 92005. DOI: [10.1103/PhysRevD.62.092005](https://doi.org/10.1103/PhysRevD.62.092005).

- [Boe92] F. Boehm and P. Vogel. *Physics of Massive Neutrinos*. Cambridge: Cambridge University Press, 1992.
- [Bow39] E. J. Bowen and A. Norton. "The quenching of fluorescence in solution". In: *Trans. Faraday Soc.* 35 (1939), pp. 44–48.
- [Bra62] E. Brannon and G. L. Olde. "The existence of a neutron". In: *Radiation Research* 16.1 (1962).
- [Bra70] E. D. Bransome et al. *The current status of liquid scintillation counting*. New York: Grune and Stratton, 1970.
- [Buo99] S Buontempo et al. "Influence of dissolved gas and temperature on the light yield of new liquid scintillators". In: *Nuclear Instruments and Methods in Physics Research Section A: Accelerators, Spectrometers, Detectors and Associated Equipment* 425 (1999), pp. 492–497.
- [C0B] Website of the C0BRA collaboration. URL: http://www.cobra-experiment.org/sites/site%7B%5C_%7Dcobra-experiment/content/e97947/e99330/Massparabola.JPG (visited on 12/03/2016).
- [Con68] J. C. Conte, J. B. Birks and G. Walker. "The fluorescence excitation spectra of aromatic liquids and solutions". In: *Journal of Physics B: Atomic and Molecular Physics* 1 (1968), p. 934.
- [Cun65] R. B. Cundall and P. A. Griffiths. "Energy Transfer Effects in the Irradiation of Benzene + Butene-2 Mixtures". In: *Trans. Faraday Soc.* 61 (1965), p. 1968. DOI: [10.1039/TF9656101968](https://doi.org/10.1039/TF9656101968).
- [Cun70] R. B. Cundall and W. Tippett. "Intersystem Crossing in Irradiated Benzene and Toluene". In: *Trans. Faraday Soc.* 66 (1970), pp. 350–362. DOI: [10.1039/TF9706600350](https://doi.org/10.1039/TF9706600350).
- [Dav68] R. Jr. Davis, D. S. Harmer and K. C. Hoffmann. "Search for neutrinos from the sun". In: *Physical Review Letters* 20.21 (1968), pp. 1205–1209.
- [Del16] S. Dell’Oro et al. "Neutrinoless double beta decay: 2015 review". In: (2016). arXiv: [1601.07512](https://arxiv.org/abs/1601.07512).
- [Dex53] D. L. Dexter. "A theory of sensitized luminescence in solids". In: *J. Chem. Phys.* 21.5 (1953), p. 836.
- [Doi83] M. Doi, T. Kotani and H. Nishiura. In: *Progress of Theoretical Physics* 69.602 (1983).
- [Eli97] F Elisei et al. "Measurements of liquid scintillator properties for the Borexino detector". In: *Nuclear Instruments and Methods in Physics Research, Section A: Accelerators, Spectrometers, Detectors and Associated Equipment* 400.1 (1997), pp. 53–68. DOI: [10.1016/S0168-9002\(97\)00933-9](https://doi.org/10.1016/S0168-9002(97)00933-9).
- [Ell87] S. R. Elliott, A. A. Hahn and M. K. Moe. "Direct Evidence for two-neutrino double-beta decay in ^{82}Se ". In: *Physical Review Letters* 59 (1987), pp. 2020–2023.
- [Eni87] R. I. Enikeev. In: *Sov. J. Nucl. Phys.* 46 (1987), p. 1492.

- [Fio12] G. Fiorentini et al. "Mantle geoneutrinos in KamLAND and Borexino". In: *Physical Review D - Particles, Fields, Gravitation and Cosmology* 86.3 (2012). DOI: [10.1103/PhysRevD.86.033004](https://doi.org/10.1103/PhysRevD.86.033004). arXiv: [1204.1923](https://arxiv.org/abs/1204.1923).
- [Fly02] So Flyckt and C Marmonier. *Photomultiplier tubes: Principles and applications*. 2002.
- [For03] A. Formicola, G. Imbriani, M. Junker et al. "The LUNA II 400 kV accelerator". In: *Nuclear Instruments and Methods in Physics Research Section A: Accelerators, Spectrometers, Detectors and Associated Equipment* 507 (2003), pp. 609–616.
- [For15] R. Ford. "A scintillator purification plant and fluid handling system for SNO+". In: *AIP Conference Proceedings* 1672 (2015), p. 080003.
- [För48] T. Förster. "Zwischenmolekulare Energiewanderung und Fluoreszenz". In: *Annalen der Physik* 437 (1948), pp. 55–75.
- [För51] T. Förster. *Fluoreszenz organischer Verbindungen*. Göttingen: Vandenhoeck und Ruprecht, 1951.
- [Fra05] D. Franco. "¹¹C measurement and CNO and pep fluxes at Borexino". In: *Nuclear Physics B - Proceedings Supplements* 145 (2005), pp. 29–32. DOI: [10.1016/j.nuclphysbps.2005.03.028](https://doi.org/10.1016/j.nuclphysbps.2005.03.028).
- [Fri04] Alexander Friedland, Cecilia Lunardini and C. Pena-Garay. "Solar neutrinos as probes of neutrino-matter interactions". In: *Physics Letters B* 594.3-4 (2004), pp. 347–354.
- [Fuk98] Y. Fukuda et al. "Evidence for Oscillation of Atmospheric Neutrinos". In: *Physical Review Letters* 81.8 (1998), pp. 1562–1567. DOI: [10.1103/PhysRevLett.81.1562](https://doi.org/10.1103/PhysRevLett.81.1562).
- [Fur39] W. H. Furry. "On Transition Probabilities in Double Beta-Disintegration". In: *Physical Review* 56 (1939), pp. 1184–1193.
- [G O] Website of G. Orebi Gann Group at UC Berkley. URL: http://underground.physics.berkeley.edu/img/experiments/snoplus/snoplus%7B%5C_%7Ddart.png (visited on 08/03/2016).
- [Gai90] T. Gaisser. *Cosmic rays and particle physics*. Cambridge, UK: Cambridge University Press, 1990.
- [Gal05] C Galbiati et al. "Cosmogenic ¹¹C production and sensitivity of organic scintillator detectors to pep and CNO neutrinos". In: *Physical Review C* (2005).
- [Gan11a] A. Gando et al. "Constraints on θ_{13} from a three-flavor oscillation analysis of reactor antineutrinos at KamLAND". In: *Physical Review D - Particles, Fields, Gravitation and Cosmology* 83.5 (2011). DOI: [10.1103/PhysRevD.83.052002](https://doi.org/10.1103/PhysRevD.83.052002). arXiv: [1009.4771](https://arxiv.org/abs/1009.4771).
- [Gan11b] A. Gando, Y. Gando, K. Ichimura et al. "Partial radiogenic heat model for Earth revealed by geoneutrino measurements". In: *Nature Geoscience* 4 (2011), p. 647.

- [Gea] Website for the Geant4 Physics Reference Manual. URL: <http://geant4.web.cern.ch/geant4/UserDocumentation/UsersGuides/PhysicsReferenceManual/fo/PhysicsReferenceManual.pdf> (visited on 03/12/2015).
- [Goe35] M. Goeppert-Mayer. "Double Beta-Disintegration". In: *Physical Review* 48 (1935), p. 512.
- [Gon14] M. C. Gonzalez-Garcia, Michele Maltoni and Thomas Schwetz. "Updated fit to three neutrino mixing: status of leptonic CP violation". In: *Journal of High Energy Physics* 11 (2014). DOI: [10.1007/JHEP11\(2014\)052](https://doi.org/10.1007/JHEP11(2014)052). arXiv: [1409.5439](https://arxiv.org/abs/1409.5439).
- [Gre88] N. N. Greenwood and A. Earnshaw. *Chemie der Elemente*. Weinheim, Germany: VCH, 1988.
- [Gri01] K.F. Grieder. *Cosmic Rays at Earth*. Elsevier B.V., 2001.
- [Gro57] G. W. Grodstein. "X-ray attenuation coefficients from 100 keV to 100 MeV". In: *National Bureau of Standards Circular* 583 (1957).
- [Hag00] T Hagner, R Von Hentig and B Heisinger. "Muon-induced production of radioactive isotopes in scintillation detectors". In: *Astroparticle Physics* 14 (2000), pp. 33–47.
- [Ham07] Hamamatsu Photonics K.K. *Photomultiplier tubes*. 2007.
- [Ham10] Hamamatsu Photonics K.K. *Photomultiplier Tubes R1828-01, R2059*. 2010. URL: http://www.hamamatsu.com/resources/pdf/etd/R1828-01%7B%5C_%7DR2059%7B%5C_%7DTPMH1259E.pdf.
- [Ham99] W. Hampel, J. Handt and G. Heusser. "GALLEX solar neutrino observations: results for GALLEX IV". In: *Physics Letters B* 447.1-2 (1999), pp. 127–133.
- [Han10] S. Hannestad. "Neutrino physics from precision cosmology". In: *Prog. Part. Nucl. Phys.* 65 (2010).
- [Her95] R Hertenberger, M Chen and B. L. Dougherty. "Muon-induced neutron and pion production in an organic liquid scintillator at a shallow depth". In: *Physical Review C* 52.6 (1995), pp. 3449–3459. DOI: [10.1103/PhysRevC.52.3449](https://doi.org/10.1103/PhysRevC.52.3449).
- [Hol11] P. C. de Holanda and A. Yu Smirnov. "Solar neutrino spectrum, sterile neutrinos, and additional radiation in the Universe". In: *Physical Review D - Particles, Fields, Gravitation and Cosmology* 83.11 (2011), pp. 1–13. DOI: [10.1103/PhysRevD.83.113011](https://doi.org/10.1103/PhysRevD.83.113011). arXiv: [1012.5627](https://arxiv.org/abs/1012.5627).
- [Hom85a] Y Homma, Y Murase and M Ishii. "Some effects of temperature on fluorescence for pure toluene and liquid scintillator". In: *J. Radioanal. Nucl. Chem. Letters* 5.95 (1985), pp. 281–290.
- [Hom85b] Y. Homma, Y. Murase and M Ishii. "Temperature dependence of pulse-height distribution in liquid scintillator". In: *J. Radioanal. Nucl. Chem. Letters* 5.93 (1985), pp. 263–270.

- [Hom87] Y. Homma, Y. Murase and K. Sonehara. "The Effect of Temperature on Fluorescence for Liquid Scintillators and Their Solvents". In: *Appl. Radiat. Isot.* 38 (1987), pp. 91–96.
- [Hun27] F. Hund. "Deutung der Molekülspektren, I und II". In: *Zeitschrift für Physik* 40 (1927), pp. 742–764.
- [Iva03] V.N. Ivanchenko. "Geant4 toolkit for simulation of HEP experiments". In: *Nuclear Instruments and Methods in Physics Research Section A: Accelerators, Spectrometers, Detectors and Associated Equipment* 502.2-3 (2003), pp. 666–668.
- [Kim93] C. W. Kim and A. Pevsner. *Neutrinos in Physics and Astrophysics*. Harwood Academic Publishers, 1993.
- [Kle29] O. Klein and T. Nishina. "Über die Streuung von Strahlung durch freie Elektronen nach der neuen relativistischen Quantentheorie von Dirac". In: *Zeitschrift für Physik A* 52 (1929), pp. 852–868.
- [Kög11] Diplomarbeit T. Kögler. *Pulseformdiskrimination und Lichtausbeutemessungen von LAB-basierten Flüssigszintillatoren*. TU Dresden, 2011.
- [Kos09] Karsten Kossert et al. "High-precision measurement of the half-life of ^{147}Sm ". In: *Applied radiation and isotopes : including data, instrumentation and methods for use in agriculture, industry and medicine* 67.9 (2009), pp. 1702–6. DOI: [10.1016/j.apradiso.2009.03.013](https://doi.org/10.1016/j.apradiso.2009.03.013).
- [Kri04] I. V. Krivosheina. "SN 1987A - Historical view about registration of the neutrino signal with Baksan, Kamiokande II and IMB detectors". In: *International Journal of Modern Physics D* 13.20 (2004), p. 2085. DOI: [10.1142/S0218271804006607](https://doi.org/10.1142/S0218271804006607).
- [Kro13] B. Krosigk et al. "Measurement of the proton light response of various LAB based scintillators and its implication for supernova neutrino detection via neutrino-proton scattering". In: *The European Physical Journal C* 73.4 (Apr. 2013), p. 2390. DOI: [10.1140/epjc/s10052-013-2390-1](https://doi.org/10.1140/epjc/s10052-013-2390-1).
- [Kro15] B Von Krosigk. "Measurement of proton and alpha-particle quenching in LAB based scintillators and determination of spectral sensitivities to supernova neutrinos in the SNO+ detector". PhD thesis. TU Dresden, 2015.
- [Kro16] B Von Krosigk, S Hans, A R Junghans et al. "Measurement of alpha - particle quenching in LAB based scintillator in independent small - scale experiments". In: *European Physical Journal C* 1 (2016), pp. 1–13.
- [Kud03] V. A. Kudryavtsev, N. J. C. Spooner and J. E. McMillan. "Simulations of muon-induced neutron flux at large depths underground". In: *Nuclear Instruments and Methods in Physics Research Section A: Accelerators, Spectrometers, Detectors and Associated Equipment* 505 (2003), pp. 688–698. DOI: [10.1016/S0168-9002\(03\)00983-5](https://doi.org/10.1016/S0168-9002(03)00983-5).

- [Lau58] G. Laustriat and A. Coche. “Influence de la température sur les photomultiplicateurs et les scintillateurs liquides”. In: *Journal de physique et le radium* 19 (1958), pp. 927–929.
- [Lau60] G. Laustriat and A. Coche. “Influence de la température sur les scintillateurs liquides”. In: *Journal de physique et le radium* 21 (1960), pp. 487–489. DOI: [10.1051/jphysrad:01960002105048700](https://doi.org/10.1051/jphysrad:01960002105048700).
- [Li15] Mohan Li et al. “Separation of Scintillation and Cherenkov Lights in Linear Alkyl Benzene”. In: (2015), pp. 1–6. arXiv: [1511.09339](https://arxiv.org/abs/1511.09339).
- [Lin09] A. Lindote et al. “Simulation of neutrons produced by high-energy muons underground”. In: *Astroparticle Physics* 31.5 (June 2009), pp. 366–375. DOI: [10.1016/j.astropartphys.2009.03.008](https://doi.org/10.1016/j.astropartphys.2009.03.008).
- [Mac14] C. Macolino et al. “Results on neutrinoless double beta decay from GERDA Phase I”. In: *Modern Physics Letters A* 29 (2014).
- [Mak62] Z. Maki, M. Nakagawa and S. Sakata. “Remarks on the Unified Model of Elementary Particles”. In: *Progress of Theoretical Physics* 28.5 (1962), p. 870.
- [Mar07] M.G. Marino et al. “Validation of spallation neutron production and propagation within Geant4”. In: *Nuclear Instruments and Methods in Physics Research Section A: Accelerators, Spectrometers, Detectors and Associated Equipment* 582.2 (Nov. 2007), pp. 611–620. DOI: [10.1016/j.nima.2007.08.170](https://doi.org/10.1016/j.nima.2007.08.170).
- [Mas07] C. Master Thesis. Lan. *SNO+ and Geoneutrino Physics*. Kingston, ON, Canada, 2007.
- [Mat85] R.D. Mathad and N. Umakantha. “On the mechanism of electronic excitation energy migration in organic liquids”. In: *Physics Letters A* 108.3 (1985), pp. 167–169.
- [Mau05] S. Maurizio and C. Santi. *Evolution of stars and stellar populations*. John Wiley and Sons, 2005, pp. 119–121.
- [Mei06] D.-M. Mei and A. Hime. “Muon-induced background study for underground laboratories”. In: *Physical Review D* (2006).
- [Men11] G. Mention et al. “Reactor antineutrino anomaly”. In: *Physical Review D - Particles, Fields, Gravitation and Cosmology* 83.7 (2011). DOI: [10.1103/PhysRevD.83.073006](https://doi.org/10.1103/PhysRevD.83.073006). arXiv: [1101.2755](https://arxiv.org/abs/1101.2755).
- [Mik86] S. P. Mikheev and A. Y. Smirnov. “Resonant amplification of neutrino oscillations in matter and solar neutrino spectroscopy”. In: *Nuovo Cimento C* 17 (1986).
- [Moh04] R. N. Mohapatra and B. P. Pal. *Massive Neutrinos in Physics and Astrophysics*. World Scientific Publishing Co. Pte. Ltd., 2004.
- [Mot03] M. Motoki et al. “Precise measurements of atmospheric muon fluxes with the BESS spectrometer”. In: *Astroparticle Physics* 19 (2003), p. 113.
- [OKe09] Helen M. (Queens University Kingston) O’Keeffe. *Temperature dependent measurement of the density of LAB*. Tech. rep. Queen’s University, 2009.

- [Oke11] HM O’Keeffe, E O’Sullivan and MC Chen. “Scintillation decay time and pulse shape discrimination in oxygenated and deoxygenated solutions of linear alkylbenzene for the SNO+ experiment”. In: *Nuclear Instruments and Methods in Physics Research Section A: Accelerators, Spectrometers, Detectors and Associated Equipment* (2011). arXiv: [arXiv:1102.0797v1](https://arxiv.org/abs/1102.0797v1).
- [Par63] C. A. Parker and C. G. Hatchard. “Delayed fluorescence of pyrene in ethanol”. In: *Trans. Faraday Soc.* 59 (1963), pp. 284–295.
- [Pas93] M. D. de Pascale et al. “Absolute Spectrum and Charge Ratio of Cosmic Ray Muons in the Energy Region from 0.2 GeV to 100 GeV at 600 m above Sea Level”. In: *Journal of Geophysical Research* 98.A3 (1993), pp. 3501–3507.
- [Pau30] W. Pauli. *Brief an die Gruppe der Radioaktiven*. Tuebingen, 1930.
- [Pet09] Petresa Canada. *Linear Alkylbenzene, Petrelab 550-Q (P 550-Q)*. 2009.
- [Pla49] J. Platt. “The perimeter free-electron model”. In: *Journal of Chemical Physics* 17 (1949), p. 484.
- [Pon57] B. Pontecorvo. “Mesonium and Anti-Mesonium”. In: *Soviet Physics JETP* 6 (1957), p. 429.
- [Pri53] R. W. Pringle et al. “A new quenching effect in liquid scintillators”. In: *Physical Review* 92 (1953), pp. 1582–1583.
- [Red09] Matthew Redshaw et al. “Masses of ^{130}Te and ^{130}Xe and Double- β -Decay Q-Value of ^{130}Te ”. In: *Physical Review Letters* 102.21 (2009), p. 212502. DOI: [10.1103/PhysRevLett.102.212502](https://doi.org/10.1103/PhysRevLett.102.212502).
- [Rei13] L Reichhart et al. “Measurement and simulation of the muon-induced neutron yield in lead”. In: *Astroparticle Physics* 47 (2013), pp. 67–76. arXiv: [arXiv:1302.4275v1](https://arxiv.org/abs/1302.4275v1).
- [Rei56] F. Reines and C. L. Cowan. “The Neutrino”. In: *Nature* 178 (1956), p. 446.
- [Sai14] Saint-Gobain Crystals. *Reflector Paint for Liquid Scintillator Tanks*. 2014. URL: <http://www.crystals.saint-gobain.com/uploadedFiles/SG-Crystals/Documents/SGC%20BC622A%20Data%20Sheet.pdf>.
- [Sch97] N. Schmitz. *Neutrino Physik*. Stuttgart: Teubner, 1997.
- [Sel56] H. H. Seliger and C. A. Ziegler. “Liquid-scintillator temperature effects”. In: *Neocleonics*. Vol. 14. 4. 1956, p. 49.
- [Ser09] Aldo M. Serenelli et al. “New Solar Composition: the Problem With Solar Models Revisited”. In: *The Astrophysical Journal* 705.2 (2009), pp. L123–L127. DOI: [10.1088/0004-637X/705/2/L123](https://doi.org/10.1088/0004-637X/705/2/L123).
- [Ser11] A. M. Serenelli, W. C. Haxton and C. Pena-Garay. “Solar models with accretion. I. Application to the solar abundance problem”. In: *Astrophys. Journal* 743.24 (2011). arXiv: [arXiv:1104.1639v1](https://arxiv.org/abs/1104.1639v1).
- [She15] MSDS - Material Data Safety Sheet. *3,5,5-Trimethylhexanoic acid*. 2015.
- [Shi03] J. Shirai. In: *Nuclear Physics B - Proceedings Supplements* 118.15 (2003).

- [Tab99] Website for the Table of Radioactive Isotopes. 1999. URL: <http://ie.lbl.gov/toi/> (visited on 05/08/2015).
- [Tot87] Y. Totsuka et al. "Observation of a neutrino burst from the supernova SN1987a". In: *Physical Review Letters* 58.14 (1987), p. 1490. DOI: [10.1016/0375-9474\(88\)90844-5](https://doi.org/10.1016/0375-9474(88)90844-5).
- [Tre10] V.I. Tretyak. "Semi-empirical calculation of quenching factors for ions in scintillators". In: *Astroparticle Physics* 33.1 (Feb. 2010), pp. 40–53. DOI: [10.1016/j.astropartphys.2009.11.002](https://doi.org/10.1016/j.astropartphys.2009.11.002).
- [Wan01] YF Wang et al. "Predicting neutron production from cosmic-ray muons". In: *Physical Review D* 64 (2001), pp. 1–6. DOI: [10.1103/PhysRevD.64.013012](https://doi.org/10.1103/PhysRevD.64.013012).
- [Web] Website. XCOM: Photon Cross Section Database. URL: <http://www.nist.gov/pml/data/xcom/> (visited on 04/01/2016).
- [Wik16] Website for the chemical Wiki of the UC Davis. 2016. URL: http://chemwiki.ucdavis.edu/Theoretical%7B%5C_%7DChemistry/Chemical%7B%5C_%7DBonding/Valence%7B%5C_%7DBond%7B%5C_%7DTheory/Resonance/Delocalization%7B%5C_%7Dof%7B%5C_%7DElectrons (visited on 11/01/2016).
- [Wol78] L. Wolfenstein. "Neutrino oscillations in matter". In: *Physical Review D* 17.9 (1978), p. 2369. DOI: [10.1103/RevModPhys.61.937](https://doi.org/10.1103/RevModPhys.61.937).
- [Xia10] H. L. Xiao, J. S. Deng and N. Y. Wang. "Oxygen quenching in LAB based liquid scintillator and a nitrogen bubbling model". In: *Chinese Physics C* 34 (2010), pp. 571–575.
- [Xia14] Dong-Mei Xia, Bo-Xiang Yu, Xiao-Bo Li et al. "Temperature dependence of the light yield of the LAB-based and mesitylene-based liquid scintillators". In: *Chinese Physics C* 38.11 (2014), pp. 1–5. DOI: [10.1088/1674-1137/38/11/116001](https://doi.org/10.1088/1674-1137/38/11/116001). arXiv: [arXiv:1402.6871v1](https://arxiv.org/abs/1402.6871v1).
- [Ye15] Xing-Chen Ye et al. "Preliminary study of light yield dependence on LAB liquid scintillator composition". In: *Chinese Physics C* 39.9 (2015), p. 096003. DOI: [10.1088/1674-1137/39/9/096003](https://doi.org/10.1088/1674-1137/39/9/096003).
- [Yeh07] Minfang Yeh, A. Garnov and R.L. Hahn. "Gadolinium-loaded liquid scintillator for high precision measurements of antineutrino oscillations and the mixing angle θ_{13} ". In: *Nuclear Instruments and Methods in Physics Research Section A: Accelerators, Spectrometers, Detectors and Associated Equipment* 578 (2007), pp. 329–339.
- [Zbi10] Karim Zbiri. "Remark on the studies of the muon-induced neutron background in the liquid scintillator detectors". In: *Nuclear Instruments and Methods in Physics Research Section A: Accelerators, Spectrometers, Detectors and Associated Equipment* 615 (2010), pp. 220–222. arXiv: [arXiv:0910.3714v3](https://arxiv.org/abs/0910.3714v3).

Acknowledgement

First and foremost I like to thank Kai Zuber who enabled this work, supported me at all times and is always a source of inspiration.

Also I would like to express my gratitude to the Nuclear Physics division at the Institute of Radiation Physics at the HZDR, which provided the hardware and its great infrastructure for the scintillator measurements. Especially Toni Kögler, the pioneer of liquid scintillator detectors in this group, and Andreas Hartmann with his 'magic hands' played a significant role in the success of this work. But also Arnd Junghans and Andreas Wagner helped me a lot with their ideas and recommendations.

Until today some of the scripts that Nuno Barros wrote still leave me startling. His untiring support and help will not be forgotten.

Valentina Lozza and Belina von Krosigk are colleagues of a special kind, hard working and always busy, have they never let me down when their help was needed.

Finally I want to thank Christiane Howe and Lotta Franek for their unconditional support during good and bad times.

Eidesstattliche Erklärung

Hiermit versichere ich, dass ich die vorliegende Arbeit ohne unzulässige Hilfe Dritter und ohne Benutzung anderer als der angegebenen Hilfsmittel angefertigt habe. Die aus fremden Quellen direkt oder indirekt übernommenen Gedanken sind als solche kenntlich gemacht. Die Arbeit wurde bisher weder im Inland noch im Ausland in gleicher oder ähnlicher Form einer anderen Prüfungsbehörde vorgelegt.

Die vorliegende Dissertation wurde unter der wissenschaftlichen Betreuung von Herrn Prof. Dr. K. Zuber am Institut für Kern- und Teilchenphysik in Dresden angefertigt.

Bis zum jetzigen Zeitpunkt habe ich keinerlei erfolglose Promotionsverfahren absolviert.

Ich erkenne die Promotionsordnung der Fakultät für Mathematik und Naturwissenschaften der Technischen Universität Dresden an.

Dresden, 21. März 2016

Arnd Sörensen